FAILURE ANALYSIS OF A 30KHZ ULTRASONIC WELDING TRANSDUCER

BY

CHRISTOPHER PAUL HAMPTON

THESIS

Submitted in partial fulfillment of the requirements
for the degree of Master of Science in Mechanical Engineering
in the Graduate College of the
University of Illinois at Urbana-Champaign, 2010

Urbana, Illinois

Adviser:

Professor K. Jimmy Hsia

ABSTRACT

Ultrasonic welding is used across variety of industries to join together thermoplastic materials. During ultrasonic welding, high frequency mechanical vibrations and compressive pressure are applied to the plastic materials. This creates intermolecular friction within the plastic which raises the temperature high enough to reach the melting point. During high volume production in manufacturing environments, the ultrasonic welding system component which fails most often is the transducer, which is responsible for creating the vibration. The transducer converts electrical energy into mechanical energy by means of a polarized piezoelectric PZT (lead zirconate titanate) polycrystalline ceramic material using high frequency voltage. The transducer is composed of round PZT disks attached to a titanium machined body by means of a central bolt. The bolt creates compressive pre-stress which prevents any tensile stresses within the brittle crystals during vibration and ensures perfect coupling between all components. The piezoelectric PZT crystals behave according to linear coupled electrical and mechanical equations. The transducer assembly is vibrated near the parallel resonant frequency to maximize efficiency and amplitude output.

The purpose of this thesis was to analyze 30 kHz multilayer PZT transducer failures caused by excessive amplitude (stress) and recommend ways to increase the lifespan. The 30 kHz transducer design being studied is produced by Herrmann Ultraschalltechnic GmbH and is currently used in production facilities around the world. Based upon warranty and field data, this size transducer fails twice as often as the 20 kHz and 35 kHz transducers. The analysis was based upon studying overall converter design practices and creating a Finite Element model to understand the stress magnitude and distribution to predict the point of failure. Laboratory experiments were then performed under high amplitude conditions to increase the stress levels until failure occurred.

The Finite Element model predicted the current design should be capable of withstanding up to 208% of nominal production level amplitudes (stress) before failure due to uncoupling between the ceramic crystals and the adjacent conducting plates. During the laboratory experiments the failures occurred between 179%-244%, however the failure mode did not correlate with the

failure predicted by the Finite Element model. All of the failures during the experiment resulted from electrical arcing at the inner diameter of the bottom ceramic disks. Furthermore, these laboratory failure modes were not consistent with those normally observed in production environments where fracture and shifting of crystals are the dominant modes. We can conclude that the electrical load used in the experiments did not accurately represent production welding conditions, which means it could not be used as a comparison against the Finite Element model.

In order to increase the lifespan of the transducer additional testing must be performed. First and foremost would be new tests which accurately reproduce production welding conditions. Then these results could be tested against the Finite Element model. Once this was completed, if the models accuracy was verified, improvements could be made and tested with the Finite Element model to try and increase the lifespan.

ACKNOWLEDGMENTS

I would like to first and foremost acknowledge Professor K. Jimmy Hsia. Not only did he guide me through the thesis process but through his classes I gained many insights into failure modes and how to analyze failures. It was not easy to coordinate a thesis via e-mail and telephone, however he was very accommodating. I would also like to thank an industry expert and ultrasonic consultant James Sheehan of JFS Engineering Incorporated for many thought provoking conversations and countless hours of help with ANSYS, a program I had never worked with before. Ulrich Vogler, an R&D manager at Herrmann Ultraschalltechnic GmbH played an integral role in designing and executing the transducer experiments necessary to complete this thesis. Most importantly, I would like to thank my wife for her patience, understanding and editing skills; I know these past 28 months were not easy…

TABLE OF CONTENTS

LIST OF TABLES

LIST OF FIGURES

CHAPTER 1: Introduction

1.1 What is ultrasonic welding

Ultrasonic welding is one of the most popular technologies used for joining thermoplastic materials to create an assembly or finished product. It can be applied to amorphous or semi-crystalline polymers, but not to thermo-sets. Its main advantages include:

- Short weld cycles (can be less than 100miliseconds)
- Localized welding
- Precise melting of only a small area
- No consumable solvents or glues
- Low energy consumption
- Hermetic sealing through contaminated surfaces or interfaces

Ultrasonic welding uses high frequency mechanical vibrations between 20 kHz to 35 kHz combined with a compressive force to create intermolecular friction within polymers at an interface. Localized melting occurs at this interface once enough heat has been generated to reach the melting or glass transition temperature. The polymers melt and diffuse due to breakage in the secondary molecular bonds, thus allowing previously immobile and separate molecular chains to intermix and flow together. This process is aided by application of an external force [1]. Upon removing the ultrasonic vibrations, the temperature rapidly decreases and new secondary bonds form between molecules containing the previously separate layers of thermoplastic. The strength of this new bond can almost reach that of the un-bonded material [1]. The term “ultrasonic” refers to the frequencies used during welding, which are beyond the range of human hearing but within the ultrasound wave range. Ultrasonic welding is used across a wide variety of industries including automotive, hygiene, feminine care, food packaging, electronics and medical devices. Figure 1.1 shows parts commonly welded using ultrasonics.

1.2 Components in an ultrasonic welder

An ultrasonic welding system can be broken into three main areas:

1. The vibrating sub-assembly
2. The fixture

3. The force build-up mechanism

The vibrating sub-assembly consists of a generator, high frequency cable and vibrating transducer/booster/sonotrode. Low voltage and low frequency electricity (typically 230 VAC at 60 Hz) is introduced into the generator where it is transformed through digital circuits into a high voltage/frequency signal (typically 800-1000VAC at 20,000-35,000 Hz). This high voltage/frequency electricity is transmitted through the high frequency cable into the transducer where the electrical energy is transformed into mechanical energy. The transducer vibrates in a pure axial mode due to its design and the way the electrical signal is controlled. The amplitude of this longitudinal wave created at the anti-node of the transducer is too low to weld most materials, thus it must be amplified by a booster. The booster increases the amplitude based upon the mass ratio between the top and bottom halves along with the efficiency of the metal. The amplitude can be further increased by the sonotrode, which is also the component used to contact the part being welded. Figure 1.2 shows the vibrating components and how the parts interconnect.

The fixture is a rigid stationary structure used to hold the polymer component(s) being welded. The fixture is typically metal with enough mass and rigidity to dampen the vibrations created by the sonotrode. This is done to ensure most of the vibrational energy is consumed by the plastic component and can be used for initiating melt flow. The geometry of this part is also chosen so that its resonant frequency is far from the vibrating frequency of the sonotrode, thus ensuring it does not oscillate at high amplitudes during welding. An ideal fixture will dampen all vibrations. A diagram of a typical stack and welding fixture or anvil for welding two thin plastic films is shown in figure 1.3.

The force build-up mechanism is used to control the amount of force being applied to the thermoplastic component(s) during welding. This is typically accomplished with an air cylinder or stepper motor, which applies a force directly against the vibrating stack. The vibrating stack is usually mounted on a precision sliding surface to ensure smooth movement. The force must be high enough to ensure transmission of the energy into the plastics and draw enough power from the transducer to quickly reach the melting point while forcing the melted surfaces together.

Force is one of the most important variables in determining the quality of a weld. Therefore, it must be carefully controlled to create a consistent weld. Figure 1.4 shows a picture of a typical force build-up system attached to a vibrating stack.

These components are combined into one assembly or "machine" which can then be used to weld plastic components.

1.3 Construction and electrical control of a 30kHz transducer

Almost all converters used in plastic ultrasonic welding have the same basic construction. The differences are minor geometric changes and some material variations. Transducers are constructed based upon a Langevin type design which is an assembly with polarized piezoelectric PZT ceramic material sandwiched between two metal cylinders with a bolt in the middle to hold them together. The most common design variation is a cylindrical ½ wavelength assembly composed of a metal body with multiple disk shaped PZT crystals and a central bolt to keep the components in compression at all times. The metal body usually has a mounting surface at the nodal point where there is zero net vibration or amplitude. The PZT disks are polarized and oriented so that common polarities face each other, i.e. positive faces positive and negative faces negative. In between each PZT disk is a copper-beryllium conducting plate where the electricity is applied via wires. Figures 1.5 and 1.6 shows a cross section and picture of the 30 kHz converter being examined in this paper. The converter studied is designed and manufactured by Herrmann Ultraschalltechnic GmbH based in Karlsbad Germany (HUG).

The amount of amplitude and power created by the vibrating transducer is controlled electronically with a power supply or ultrasonic generator. The generator is designed so that the vibrating assembly maintains the same amplitude at the welding surfaces at all times, regardless of how much force is being applied to the welded part. The challenge is that the generator has no direct feedback of the physical displacement inside the PZT ceramics; it can only monitor and control the voltage, current and frequency. Because amplitude is a function of velocity and frequency (see equation 1.1 below), the amplitude is kept constant by maintaining the same frequency and velocity [2].

$$v = 2\pi * f * \lambda \tag{1.1}$$

The frequency can be directly controlled by the generator, but the velocity can only be controlled and maintained by varying the current or power according to equation 1.2 shown below.

$$P = F * v \tag{1.2}$$

In this equation P, is power which is based upon amperage or current and F is the external force being applied to the vibrating surface. To summarize, the generator maintains the same amplitude under various welding forces by increasing or decreasing the current/power to maintain the velocity while simultaneously keeping the frequency constant (or changing it only fractions of a percent) to satisfy equation 1.1.

1.4 Failure modes and lifetime of 30kHz transducer

There are seven main failure modes for an ultrasonic transducer. These failure modes are based upon the author's direct experience for the past 5 years in the field of ultrasonic welding.

1. Fracture of ceramic crystals

   Fracture occurs when the crack grows large enough to cause the crystals to separate into multiple pieces. Even if the separated pieces do not move apart from eachother the fracture surfaces are no longer perfectly coupled, which allows relative motion leading to friction and rapid overheating [3]. Poor coupling at the interface causes the resonant frequency to change, creates unequal electrical properties and allows a short circuit path for high voltage arcing. Cracks initiate at either pre-existing cracks/voids or they are formed by tensile loads, impact stresses or shear stresses [4]. Figure 1.7 is a picture of a converter failure due to cracked PZT crystals.

2. Shifted ceramic crystals

   Crystals can be displaced along the plane perpendicular to the axis of symmetry when compressive pre-stress at two mating surfaces temporarily becomes zero. Once crystals shift, mechanical forces and moments are no longer symmetric about the central axis, which creates a bending moment rather than perfectly longitudinal motion. At this point amplitude distribution is no longer even, power draw increases

and internal stresses increase in the crystals. In many cases, shifted ceramic crystals also lead to fracture. Figure 1.8 shows converter failure due to shifted crystals.

3. Arcing due to short circuit

   If the voltage applied to the ceramic crystals is high enough and/or two conducting surfaces of opposite polarity are close enough, then arcing can occur. This arcing can cause local depolarization due to very high temperatures and thus possibly initiate crystal fracture.

4. Fracture of pre-stress bolt

   Fracture of the pre-stress bolt occurs when the dynamic tensile stress exceeds the endurance limit. When this happens the fracture propagates through bolt causing complete failure, breaking the bolt into 2 pieces. After bolt failure, pre-stress becomes zero, all transducer components become uncoupled and the transducer will not operate.

5. Fracture of Beryllium conducting plate at wire connector

   A small portion of the Beryllium plate is not compressed between PZT crystals and protrudes for attachment to the conducting electrical wire. The electrical conducting wire is connected to the top housing of the transducer body, however the beryllium plate where it connects is vibrating at the same frequency and magnitude as the PZT crystals. This protruding section can fatigue due to high frequency flexure and fracture, causing a loss of electrical power to one set of PZT crystals. This completely changes the electrical properties of the transducer. The remaining crystals are forced to carry all remaining power which overloads them and leads to overheating or fracture. The loose wire created during this failure can also touch other parts of the transducer and create a short circuit.

6. Fracture in the Titanium body

   Fracture in the Titanium body occurs due to crack growth caused by dynamic stresses which exceed the fatigue limit. As the crack grows, the resonant frequency of the transducer changes until it is outside permissible operating limits. Alternately, the cracked surface temperature can overheat the entire transducer.

7. Overheating of PZT crystals

Overheating the PZT crystals occurs when the temperature rises close to the Curie point and de-polarization begins. During depolarization the crystals lose their piezoelectric properties leading to excessive dynamic stress and fracture (failure #1).

Based upon data collected between 2006-2008, over 80% of recorded transducer failures resulted from cracked and shifted crystals [5]. These two failure modes will be the focus of this thesis.

The lifespan of a transducer varies widely depending upon the welding application and proper operation. Based upon the author's 5 years of field experience visiting customers and repairing equipment, several generalities can be made:

1. Transducers in low force and/or low power applications last longer than those in high force and/or high power applications.
2. More welding cycles shorten the lifespan.
3. Properly operated and maintained transducers can vary from as little as 3 months and as long as 10 years producing tens of millions of welded parts. The average life expectancy is between 1-3 years. Customers expect a transducer to last at least one year.

Between 2006-2008, the failure rate of 30 kHz transducers varied between 5-15%. This failure rate is based upon the number of transducers returned for examination compared to the total number manufactured that same year. Data for the other two sizes produced by HUG (20 kHz and 35 kHz) show much better life-spans, with failure rates between 4-8% [5].

1.5 Importance of transducer lifespan

The acceptable lifespan and failure rate of an ultrasonic transducer due to defects, is based upon the expectations of the end users and the nature of ultrasonic applications. Fortunately, transducer failure does not pose a health risk to an individual. There is no single recordable case of serious injury due to transducer failure. However, excessive failure rates tarnish a company's image and can cause a loss of future business. In addition, there are hard costs associated with replacing the failed components including the resources wasted to build the original failed part, the resources to create a new part, the labor to replace the component and process the paperwork for each of these steps. The customer incurs additional costs in poorly welded products, possible

customer liability, loss of production plus labor to troubleshoot and replace the failed component. It is very difficult to quantify what an ideal lifespan and failure rate should be. From a customer perspective they should last forever, but in reality the resources needed to create the "perfect" transducer are limited. As with virtually all engineered products there must be a balance between the resources available to design and optimize a part counterbalanced by market demands allowing the product to be competitive and generate revenue. The goal of this paper is to increase the lifespan and reduce the annual failure of the 30 kHz transducer. This will be accomplished by investigating the current design through FEA analysis, verifying the accuracy of the FEA model through laboratory testing and then refining the model to allow for higher stress levels before failure occurs.

1.6 Tables and Figures

Figure 1.1 – Parts welded with ultrasonics

Figure 1.2 – Schematic of vibrating assembly

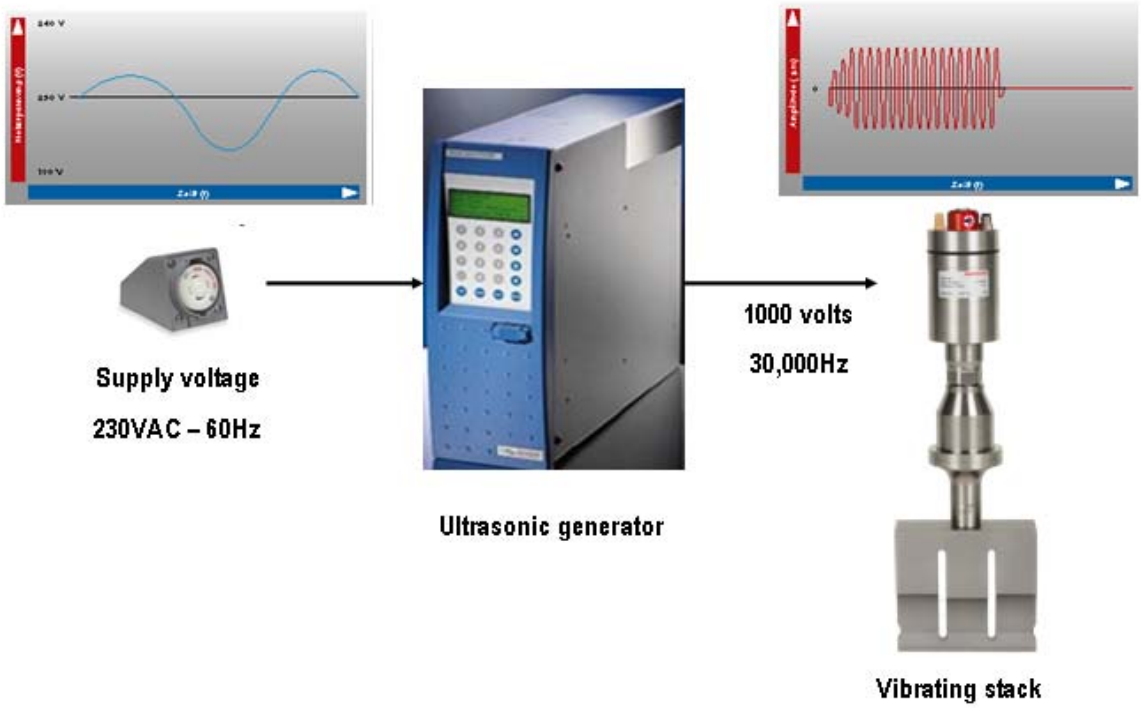

Figure 1.3 – Diagram of welding fixture and vibrating stack

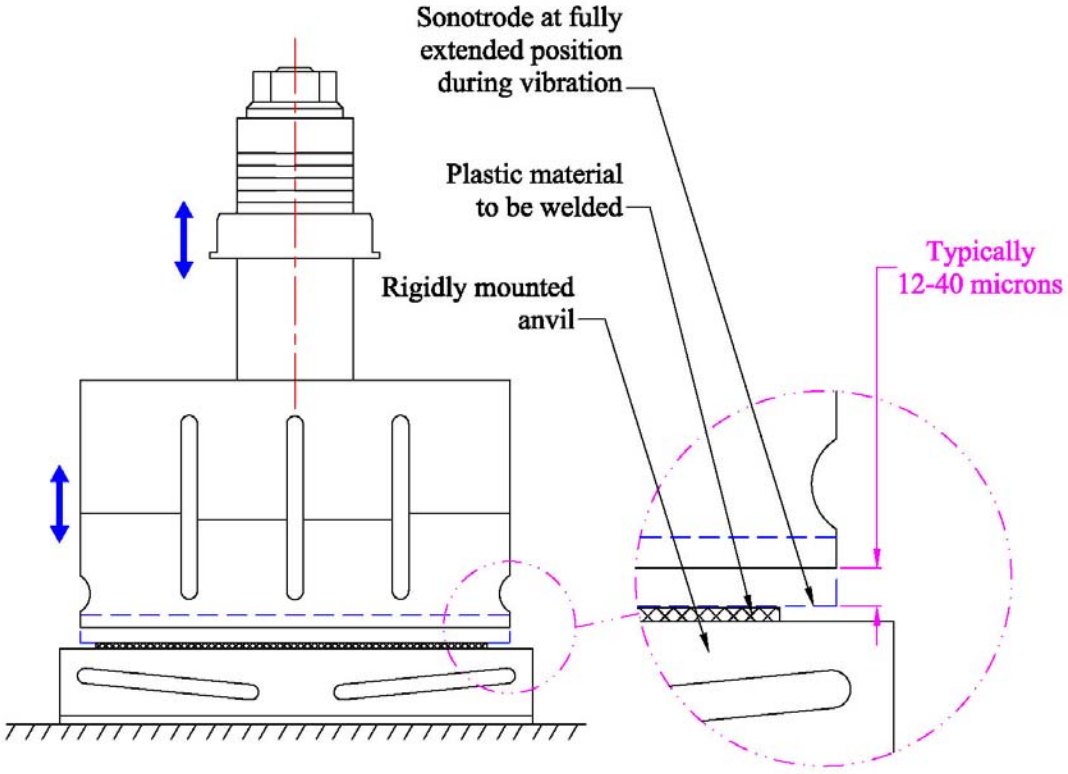

Figure 1.4 – Force build-up mechanism attached to a vibrating stack

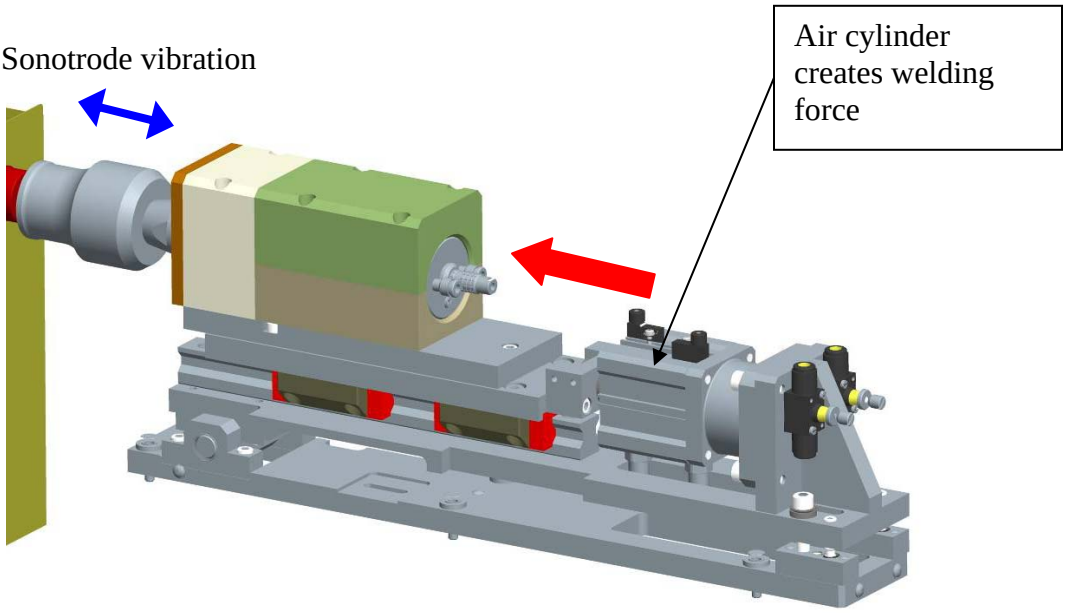

Figure 1.5 – Cross section of 30 kHz transducer

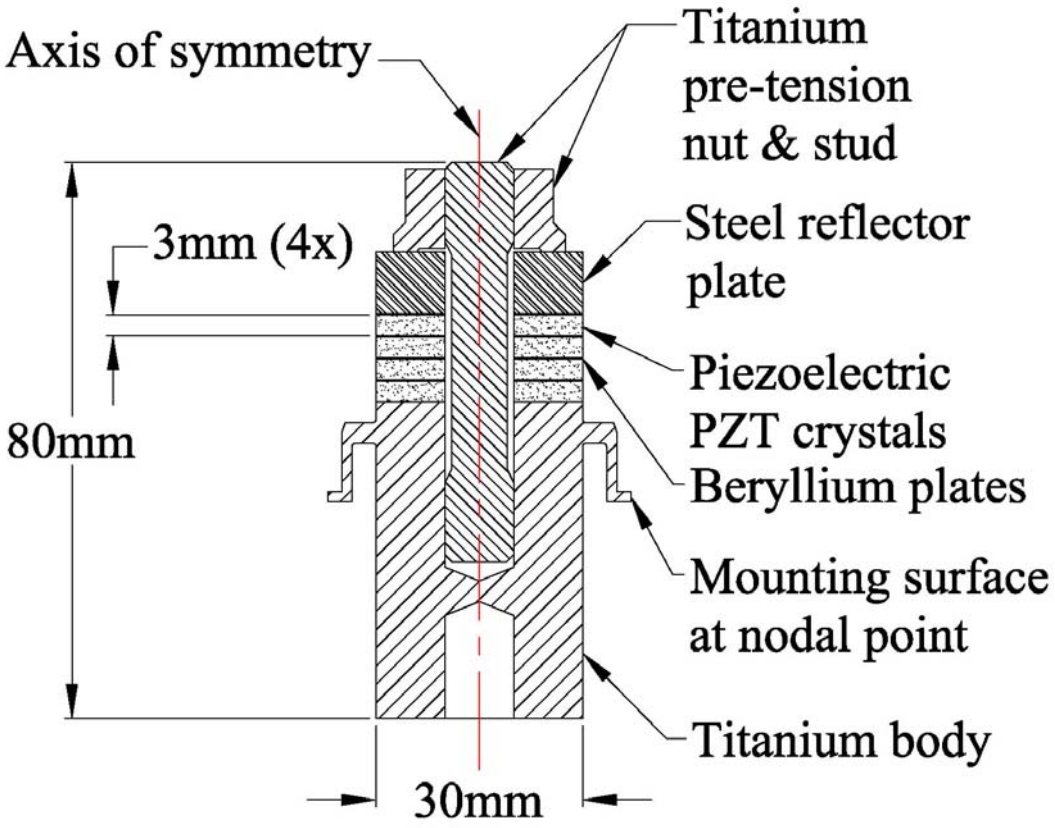

Figure 1.6 – Picture of 30 kHz transducer

Figure 1.7 – Transducer failure due to cracked crystals

Figure 1.8 – Transducer failure due to shifting crystals

CHAPTER 2: Literature review

2.1 Fundamentals of PZT piezoelectric crystals

Piezoelectricity was first discovered in 1880 by Jacques and Pierre Curie. They discovered that in certain materials an electric charge could be generated by applying a stress. The most well known material exhibiting this property is quartz. In Greek, the word "piezo" means "to press". Therefore, piezoelectricity literally means generating electricity from pressure [6]. The Curies later confirmed the reverse effect whereby mechanical strain can be generated by applying an electric charge. In the 1950s more efficient and powerful piezoelectric materials were discovered, including those in the form of lead zirconate and lead titanate (PZT). These materials can have a permanent dipole moment and a much higher dielectric constant. They can be easily manufactured as polycrystalline ceramics, doped with a variety of elements and polarized [6]. Lead zirconate titanate ($PbZr_{1-x}\ Ti_x\ O_3$) is the material used in the ultrasonic transducers studied in this paper.

The piezoelectric properties of PZT ceramics are a result of their molecular structure. The most useful piezoelectric properties are observed when the mole fraction of Ti and Zr are close to 0.5. $PbZr_{.47}\ Ti_{.53}\ O_3$ is a common configuration used in industry. Examining the phase diagram in figure 2.1, it is apparent that multiple crystalline structures can exist near this mole fraction. This transitional area is called the morphotropic phase boundary (MPB) [7]. Above the Curie temperature (Tc), the structure is cubic. At this point there is no net dipole due to cubic symmetry. However once the temperature drops below the Curie point, the structure becomes tetragonal or rhombohedral. It is this distorted structure that creates an electric dipole moment. These non-cubic structures have over 14 stable domain configurations at the MPB giving them great flexibility during polarization [7]. Figure 2.2 shows the structure above and below the Curie temperature.

Unit cells in PZT crystals combine to form domains. Because they are polycrystalline materials, there are grain boundaries and voids formed during manufacturing, which separate these domains. Figure 2.3 shows an SEM image of a typical PZT under high magnification [8]. The

individual grains, grain boundaries and voids are clearly visible. The material properties are dependent on grain size, grain boundary thickness as well as the size and number of voids. These properties are all controlled during the manufacturing process and must be consistent in order to maintain consistent physical properties.

The polycrystalline nature of PZT yields many grains with random crystallographic orientations. Even though each grain has its own dipole moment, when the temperature is below Tc, the overall structure on a macroscopic level has zero net polarization and is considered un-poled. In this state, the material does not exhibit any piezoelectric properties. In order to create a net dipole moment, the material needs to be polarized. This is done by applying a strong external electric field above the coercive strength of the material. This causes the tetragonal or rhombohedral molecular structure to deform into an alternate stable geometry where the direction of polarization is parallel to the externally applied electric field. This is illustrated in figure 2.4 which shows the un-poled and polarized state of a PZT. If the temperature goes above the Curie point or if a strong enough external electric field is applied, the polarization will be reversed or become polarized in a new direction.

The piezoelectric properties exist because of the net polarization in the material. The piezoelectric effect works due to distortion of the molecules. This effect is illustrated in figure 2.5 which shows a piezoelectric material with no externally applied electrical charge. Once an electrical charge is applied, the electrons and electron holes either attract or repel the polarized material, causing it to expand or contract thus straining the material.

The constitutive equations which describe the behavior of piezoelectric materials can be derived from thermodynamic principles. The final electromechanical equations describing the coupled linear behavior of a piezoelectric material are shown in equation (2.1) [9, 10].

$$\begin{aligned} T_i &= c_{ij} S_j - e_{mi} E_m \\ D_i &= d_{mj} T_j + \varepsilon_{mn} E_n \end{aligned} \tag{2.1}$$

T, S, D, E, c, e, ε and *d* are the stress, strain, electric flux, electric field, stiffness matrix, piezoelectric stress matrix, dielectric permittivity and piezoelectric constant respectively. Examining these equations reveals the fundamental behavior of piezoelectric materials under the influence of electric fields and mechanical strain. The top equation illustrates how the mechanical stress generated in the crystal is due to the material stiffness times the strain. At the same time however an electric field is generated, which opposes the direction of strain and stiffens the material. The bottom equation illustrates how the electric charge or current is generated by mechanical stress and the capacitance of the ceramic material. These equations fail under high applied voltage and stress due to hysteresis effects which cause *c, d* and *e* to vary with the applied electric field or stress, causing non-linear behavior [11]. These equations also illustrate how the mechanical strain produced by a piezoelectric crystal installed in a device can be controlled with electrical signals even though there is no mechanical feedback.

Even though piezoelectric PZT materials were first intensively studied when sonar was first developed in World War I, the behavior of piezoelectric PZT crystals allows them to be used in a wide variety of other novel and interesting applications. They are used extensively in medical applications and considerable research is underway for use in the design of MEMS. PZT crystals can be used in precision position devices with accuracy down to a picometer [12]. In fact, piezoelectric materials are limited by the ability to control the applied voltage as opposed to the material properties.

2.2 Langevin type piezoelectric PZT transducer design and operation

Langevin style transducers were first developed in 1917 for use in sonar during World War I. In the 1960s, this design was used to create transducers for ultrasonic thermoplastic welding. As previously mentioned, a Langevin type transducer is composed of piezoelectric crystals compressed between two metal pieces, as shown in figure 1.5. Even though hundreds of thousands of transducer s have been designed and manufactured in the past 50 years, there are no universal standards or design specifications beyond general rules of thumb and guidelines. Each manufacturer has its own design philosophy and construction regime, which includes a considerable amount of proprietary knowledge. In addition, there are also only a handful of specialists who fully understand the intricacies of designing and controlling a piezoelectric

transducer. This is mainly a result of the relatively small market size for ultrasonic welding equipment, which is no more than a few hundred million dollars per year. This market does not attract funding for research at a fundamental level. Because the transducer is only one component of a welding machine, it makes up a small fraction of a company's R&D and engineering budget. In my research, I have found most companies rely on trial and error and take a very reactive approach to transducer design. As long as the current design provides consistent welding results, little additional progress is made. This paper is the result of such thinking. The current 30 kHz design from HUG is not as robust as the company would like. It fails too frequently and does not last as long as the other size transducers. Every company has limited resources and must decide how to maximize the return on those resources, keep its employees working and keep its shareholders/owners happy. If a particular device is operating correctly, large amounts of resources will not be invested in refining the design. Thus many practical engineering problems and products on the market today are not being optimized to the fullest extent possible.

I consulted and studied with several veteran engineers (Ulrich Vogler - HUG, James Sheehan - JFS Engineering,) in industry who have spent over 20 and 10 years respectively designing ultrasonic transducers for plastic welding and other applications using piezoelectric crystals. Their respective design approaches and methodologies are used throughout this section and subsequent sections relating to the FEA analysis along with the failure experiment.

Even though PZT transducers for plastic welding are not extensively studied, there are entire books devoted to the design and use of piezoelectric crystals [13,14]. These books only provide very general guidelines, however and they are geared more towards the most current applications, such as micro-positioning devices, sensing devices and sonar or circuitry for an ultrasonic generator. They also have disclaimers where they acknowledge that each design and application requires empirical testing, especially an application such as ultrasonics welding which involves high stress levels and high power requirements.

Examined as a whole, a piezoelectric PZT transducer is a very complicated device involving a diverse group of fields such as electronics, statics, dynamics, strength of materials, acoustics,

wave propagation, thermodynamics, electrostatics, crystallography and circuit theory [13]. This is due to all the interactions which are occurring during operation. Even though this device is very complex, we can still break it into smaller manageable pieces to study the basic operating principles and gain a general understanding with a few simple models [15].

In its simplest form, the transducer can be modeled as a simple mass-spring-mass system which is operated near its mechanical resonant frequency. This is illustrated in figure 2.6, where the spring constant k is based upon the stiffness or modulus of the material and m represents the mass of each side. Equation 2.2 describes the approximate frequency of this system with simplified assumptions such as no mechanical losses of any kind, i.e. entropy generation equals zero.

$$f = \sqrt{\frac{k(m1+m2)}{m1m2}} \qquad (2.2)$$

Since the transducer must be designed to operate at a specific frequency, this equation makes it clear that aside from all other considerations, the material properties play a large role in proper operation.

If we take a deeper look into the mechanical aspect of the transducer, we can see how the dynamic stress/strain distribution and the overall displacement which is shown in figure 2.7. The area of highest strain/stress is in the middle at the nodal point, however the highest displacement and velocity is at each end. This figure also confirms that these are ½ wavelength transducers with one nodal point where the transducer is mounted.

From a purely electrical stand-point, the vibrating system can also be modeled as various lumped equivalent circuits depending on the operating frequency. This model was first developed in the 1960s by Mason and has been used extensively since then [16]. Figure 2.8 shows the equivalent circuit model for a transducer vibrating in series and parallel resonance [17]. In these simplified models, Cs/Cp represents the stiffness (i.e. spring constant), Ls/Lp represents the mass, Rs/Rp represents the mechanical losses during vibration and Cos/Cop represents the capacitance of the PZT crystals.

During series resonance, Ls and Cs effectively cancel out as current flows back and forth between these two components. This creates a short circuit condition, as Rs is the only portion left in the circuit to resist the flow of current. This leads to high current and low voltage or low impedance. Since the capacitor and inductor being discussed represent a mechanical system, they can also be described as follows. During series resonance, the energy is shifting back and forth between potential energy (mass) and kinetic energy (spring). At full transducer extension, whether the transducer is in tension or compression, the velocity is momentarily zero and all the energy is stored as potential energy. At the time of highest velocity, half way through a full cycle, the kinetic energy is maximized and the potential energy is zero. During series resonance, Cos has no effect on the system performance, as the impedance across it is very high and very little current flows through it [15].

During parallel resonance, Lp and Cp resonate with Cop to cancel out, as the current flowing through each segment of the circuit is equal in value but 90 degrees out of phase. This allows almost zero current to flow through the circuit, thus creating a high voltage and low current situation similar to an open circuit with a high impedance value. [15]

It is important to note that the parallel resonance does not exist when only considering the mechanical behavior of the transducer, as it does not capture the capacitance of Cop. This is more clearly seen in the FEA section when the amplitude is plotted versus frequency. The amplitude reaches a localized maximum at the series resonant point, but not at the parallel resonant point. When the frequency is somewhere between these two resonant values, a hybrid electric model needs to be considered.

The equivalent circuits help us interpret and understand the impedance plot, which is one of the primary tools used to design transducers aside from FEA [18]. The impedance plot is created by applying a voltage to the transducer and varying the frequency while simultaneously reading the impedance or the ratio of alternating voltage to current along with the phase angle. A plot of the results clearly shows the series and parallel frequency values, the distance between them, the shape of the curve in between and the magnitude of the impedance at these points. Figure 2.9

shows a typical impedance plot from an actual 30 kHz transducer used in the experimental portion of this paper. In this plot the series resonant frequency is 29,565Hz and impedance is at a minimum. The parallel frequency is 31,710 Hz where the impedance is at a maximum value. Based upon the way HUG controls the voltage going to the transducer, this impedance plot will allow the system to operate close to 31,500Hz during operation. By using a very wide frequency range, the impedance plot will also locate any other resonant frequencies which represent alternate modes of vibration.

While these simple mechanical models and electrical circuits help understand how the transducer operates, practical design of a working transducer requires more detailed information. When designing an ultrasonic transducer, the following basic parameters must be considered [15]:

1. What frequency will it operate at?
2. How much peak and continuous power will the transducer be able to output and what is the duty cycle?
3. How much mechanical displacement or amplitude needs to be produced at the coupling surface?
4. How will the transducer be electronically controlled? Will it run at the series resonant frequency (f_s), the parallel resonant frequency (f_p), or somewhere in between?
5. What will be the maximum voltage experienced by the crystals?
6. How many cycles is the transducer expected to last before failure?

The transducer studied in this paper vibrates at 30,000 Hertz, draws a maximum peak power of 1700 watts and reaches an amplitude of 7.5 microns. The control will be in between f_s and f_p and the real voltage will not exceed 1000Vrms. The lifespan should be more than 10^{12} cycles, which represents 24/7 operation for 356 days.

Once these specifications are known, the overall geometric configuration can be designed and materials can be selected. Many of these steps rely on approximations and rules of thumb based upon past experience or simply iterations of current designs. For example, the diameter of the transducer should be less than ¼ the wavelength of the operating frequency to minimize transverse vibration and excessive transverse stresses in the radial direction [19]. This also helps

maintain purely longitudinal vibration along the center axis, since this is the vibration performing the work during the welding process. Vibration in any other direction is wasted. Another example deals with the material selection. The transducer studied is made out of titanium, copper-beryllium, PZT-8 and cold worked tool steel. Copper-beryllium is used because it has high thermal and electrical conductivity. It is also strong and has high dimensional stability under thermal loading. Titanium is an expensive material but very efficient at transmitting vibration, while PZT-8 provides very high power density and good piezoelectric properties. The steel is only used on the reflector plate to increase the mass, which reduces the length of the transducer and helps create an even stress distribution on the crystals from the pre-stress bolt. Lastly, the amount of pre-compressive force on the ceramics is a balance between the following factors [20]:

1. De-polarizing the crystals - Too much force will cause depolarization and adversely affect the piezoelectric properties.
2. Maintaining compression on the ceramics at all times - Shifting or cracking can occur if excessive amplitude spikes cause a loss of compression at any time.
3. Remaining below the fatigue limit of the bolt - Bolts will fail if an adequate safety factor is not used.
4. Keeping the total static bolt elongation 10 times greater than the total change in length during vibration - This insures the crystals are in compression and coupled together at all times

After the geometry and material have been selected, the transducer should be modeled with an FEA package to make sure it vibrates with the proper mode and to ensure the static pre-compression is more than the dynamic stresses with some additional safety factor. The FEA model is also used to verify that the stress levels will not cause failure in any other materials. If the FEA model results are positive, the transducer is manufactured and then tested to see if the operating frequency, impedance plot, displacement and power draw are sufficient. At this point, the duty cycle can be tested and cooling requirements can be found.

2.3 Modeling transducers with FEA

The mentor I worked extensively with on the FEA analysis portion of this thesis, Jay Sheehan, provided me a simple analogy about modeling transducers. To paraphrase, "if welding transducers were used by NASA on the space shuttle, we would have millions of dollars of research funding and a supercomputer at our disposal to create a tremendously sophisticated model that accounted for all the interactions taking place during vibration and actual welding of thermoplastic materials". In reality there are not enough resources to create a comprehensive model which means the engineer must rely on experience, assumptions and approximations to the best of his/her abilities. The two other facts I learned very quickly were "garbage in = garbage out" and that you can twist numbers or material properties to distort reality. In the first case, incorrect material properties, dimensions, boundary conditions or program parameter selections can lead to meaningless results. In the second case, it is dangerous when you know what number you should end up with. This makes it very easy to manipulate numbers to match the desired result. These comments are being made to illustrate the imperfect nature of FEA and to highlight the fact that FEA cannot be performed in a vacuum. You must also verify your findings with experiments. This is why both steps are being done in this thesis. An FEA model is created and empirical tests are performed to verify the FEA results before they are manipulated to try and improve the design.

There were no technical documents or studies discovered during my research which reported a single comprehensive model that simultaneously accounted for pre-stress, dynamic stress, load conditions from welding and temperature fluctuations. Most studies looked at one piece of the transducer or broke it into several pieces for easier analysis.

The analysis process used in this paper is based upon this same principle. It is broken up into pieces and analyzed individually. The final results are found by summing each part then drawing conclusions about stresses, lifespan and safety factor. This piecemeal approach has been proven to work in the past. Due to computational limitations of the ANSYS educational software, only a 2-dimensional axisymmetric model was created and studied. Based upon prior experience, this produces very accurate results with one flaw. Because a 3-D model is not created, the analysis cannot detect any bending modes of vibration, which can be a problem in transducer design.

This is especially true once the transducer is connected to the sonotrode and booster and used in production. Most other studies using FEA to analyze a transducer created a 3-D model to test this behavior [21].

Following is a generic process for using FEA to analyze a transducer [15]:

1. Enter the material properties and geometry - values must be very accurate and handbook values should not be relied upon.
2. Modal analysis – Calculate the various modes of vibration along with the corresponding frequencies and examine the modal shapes. The goal is to have pure axial vibration at the desired operating frequency and to make sure the next closest mode is far enough away so that it is not excited during operation. Ideally, the alternate frequencies should be several thousand hertz away.
3. Static pre-load stress analysis – Choose the contact surface conditions between the separate pieces and apply the desired force to the bolt to simulate tightening the center bolt. Examine the magnitude and distribution of the stress in the transducer, paying extra attention to the piezoelectric crystals and the interfaces between pieces.
4. Impedance plot - Create an impedance plot by performing a harmonic analysis across a range of frequencies that fall before and after the series and parallel resonant frequencies. Use the impedance plot to determine the frequency producing the desired amplitude at the coupling surface of the transducer and the corresponding power draw.
5. Harmonic stress analysis – Perform a harmonic analysis at the frequency producing the desired amplitude. Examine the stress distribution and compare with pre-load values.
6. Thermal analysis – Simulate heat generation and forced convective cooling to determine temperature rise inside crystals. As a rule of thumb, the temperature should never reach more than 65 degrees Celsius.

The stress data generated in step #3 and #5 can be added together to determine the total dynamic stress during operation. These combined results allow us to measure how much stress or amplitude it will take to overcome the pre-tension and allow the ceramics to shift or experience tensile loading.

Numerous research papers have analyzed the relationship between modes of vibration and geometry of the transducer in an effort to better understand the general shapes which give the best performance [22, 23].

The FEA process described can yield results very close to reality, however in making some of the simplifications, certain practical phenomena are overlooked. The FEA analysis is performed while vibrating in free air. Experiments with actual transducers show that they can operate almost indefinitely in free air without failure. In actual production environments when plastic welding takes place, the welded material plus the fixture it is welded against have an impact on the vibrating transducer assembly. Under ideal conditions, the plastic material perfectly couples with the vibrating sonotrode and acts as a pure spring/mass damper system. However, when perfect coupling does not occur or if the material is very thin or rigid, the supporting tooling can also react due to the forced vibration from the sonotrode. The supporting tooling and plastic can reflect back a wave that is out of phase and/or at alternate frequencies. This rogue reactionary force wave can then induce alternate vibration in the transducer. This can either interfere or enhance the primary mode of vibration, which in turn affects the dynamic stress distribution and magnitude. In addition, if these external vibrations cause a change in the pure uniaxial vibration of the converter, an electric charge in the PZT crystals can be induced which must be compensated for by the electronic generator. These interactions can cause incorrect amplitude or amplitude spikes which can then lead to converter failure. At this point, the numeric models are no longer accurate. To compound this challenge there isn't a reliable, easy or accurate method to directly measure what is actually happening inside the transducer while it is welding. Indirect measurements of the voltage and current can be made, but the true stress/strain at a given point in the converter is not easily available. Because of this, much of the development or fine tuning for reliability has been based upon trial and error which is expensive, cumbersome and time consuming. The solution has been to design a transducer with the highest possible safety factor, but this is always limited by the need to maximize power and amplitude output while minimizing heat build up, costs and size.

2.4 Tables and figures

Figure 2.1 – Phase diagram of PbZrTi

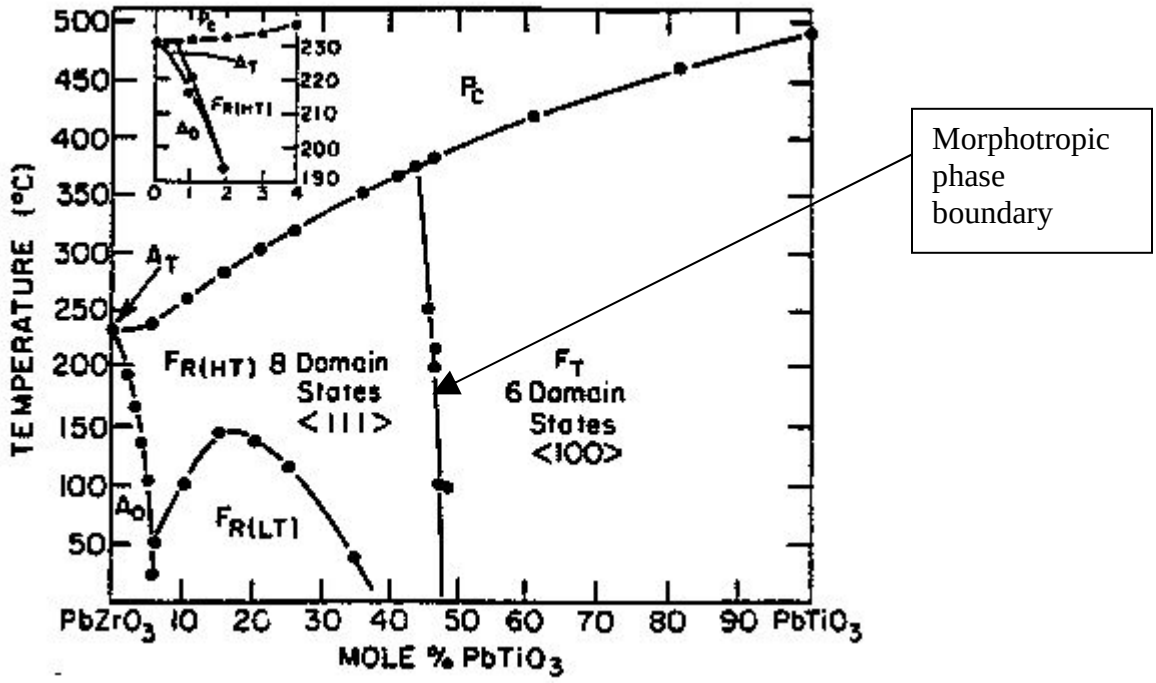

Figure 2.2 – Molecular structure of PZT above and below Curie temperature

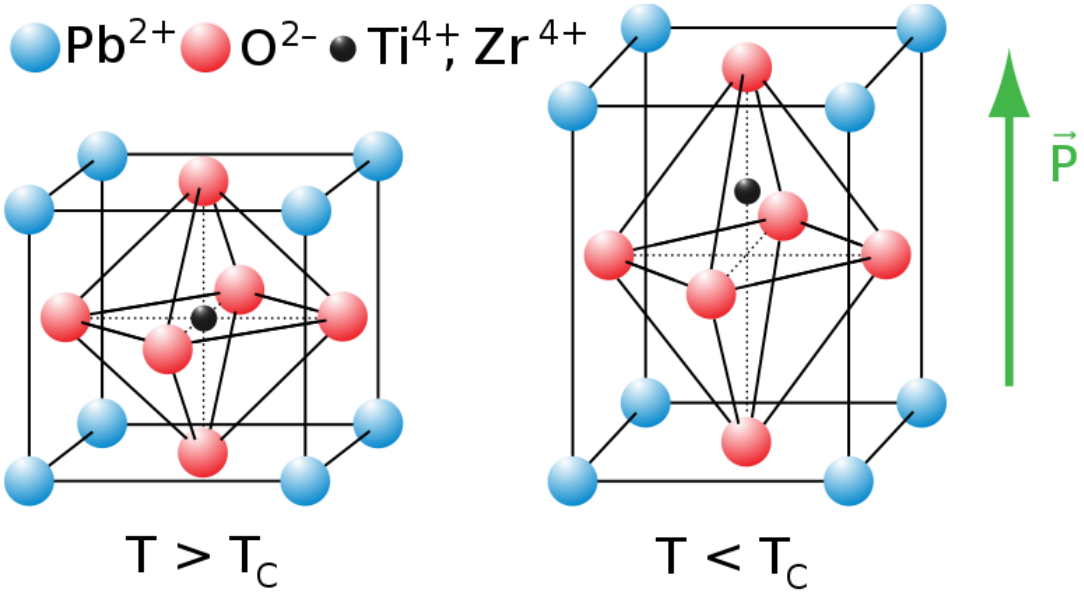

Figure 2.3 – SEM of PZT showing grains, grain boundaries and voids

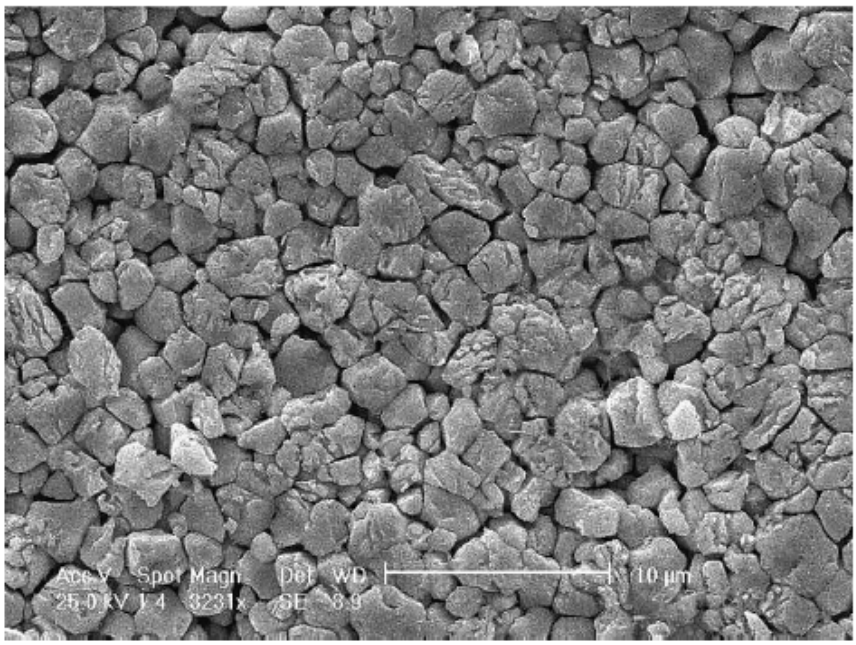

Figure 2.4 – Un-poled and polarized PZT

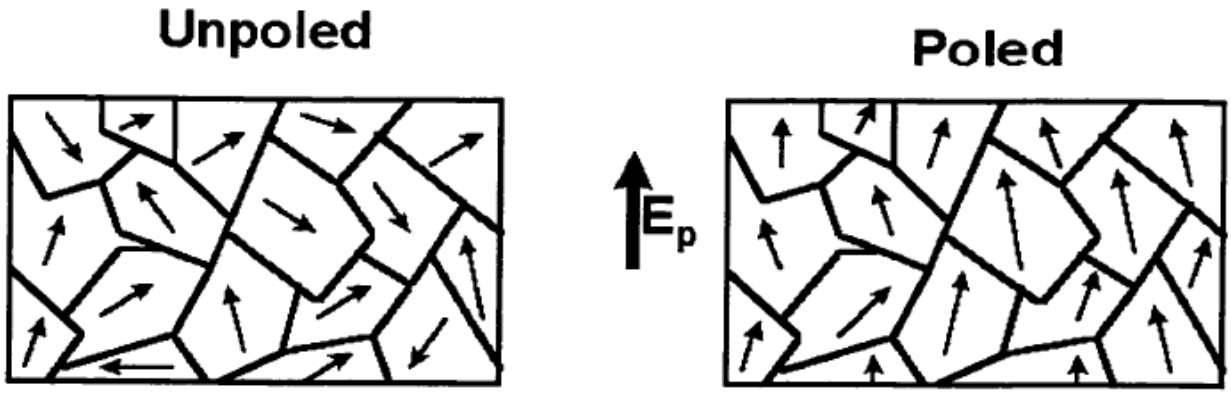

Figure 2.5 – Polarized material with various electric charge states

[http://www.americanpiezo.com/piezo_theory/index.html]

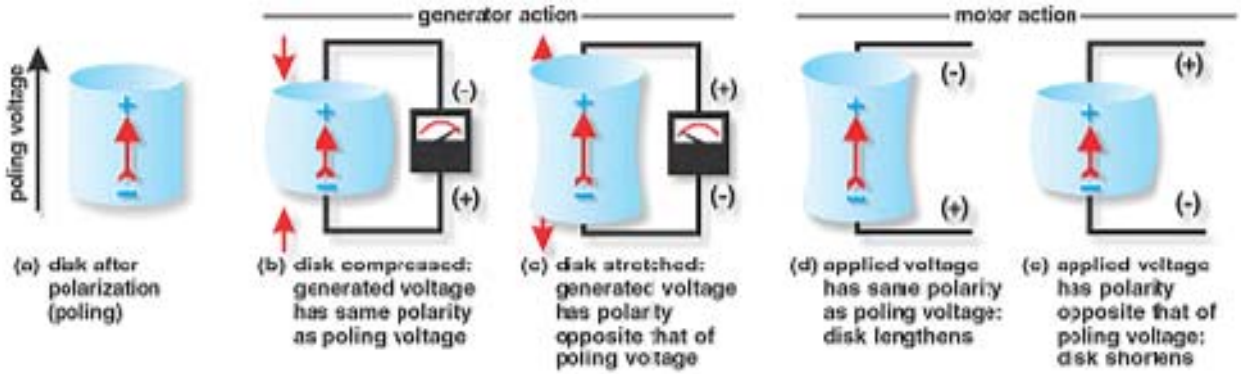

Figure 2.6 – mass-spring-mass transducer model

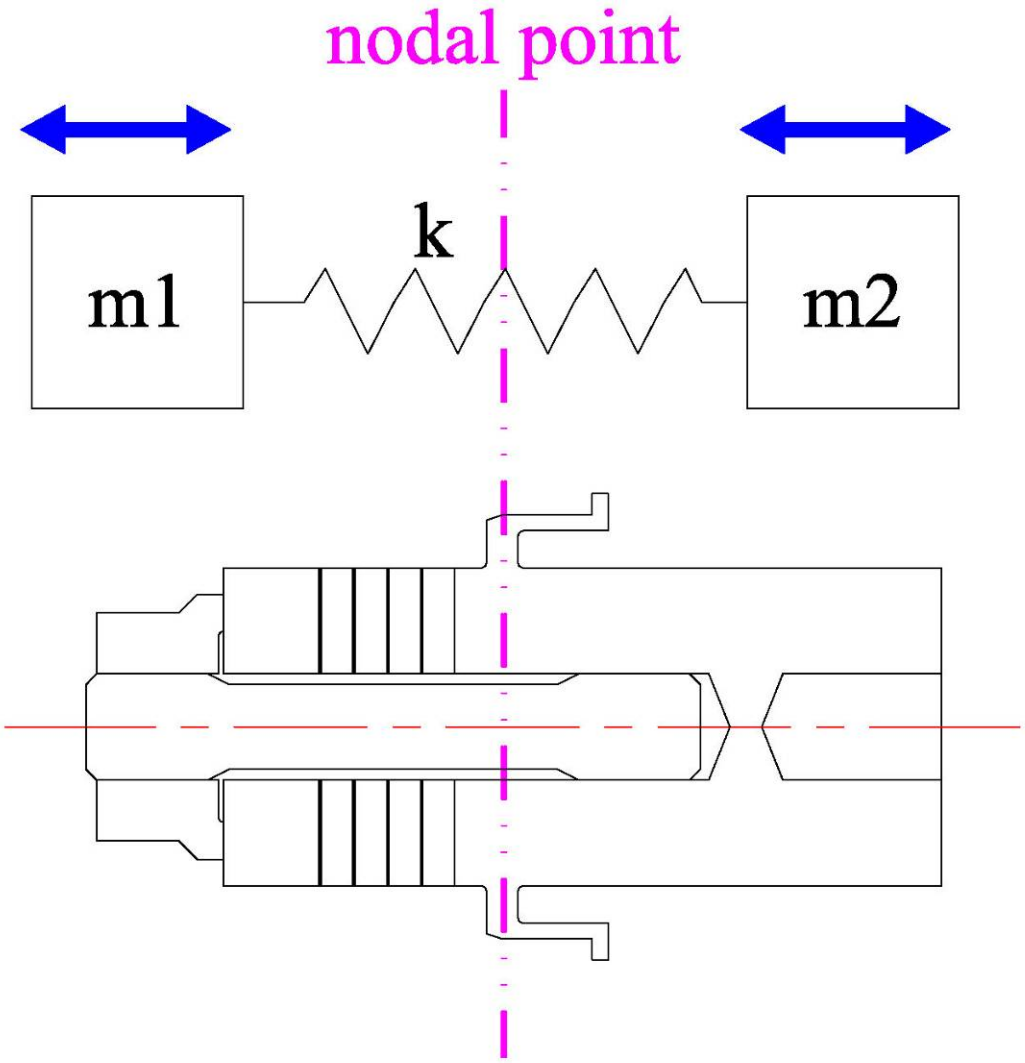

Figure 2.7 – stress/strain and displacement along transducer during vibration

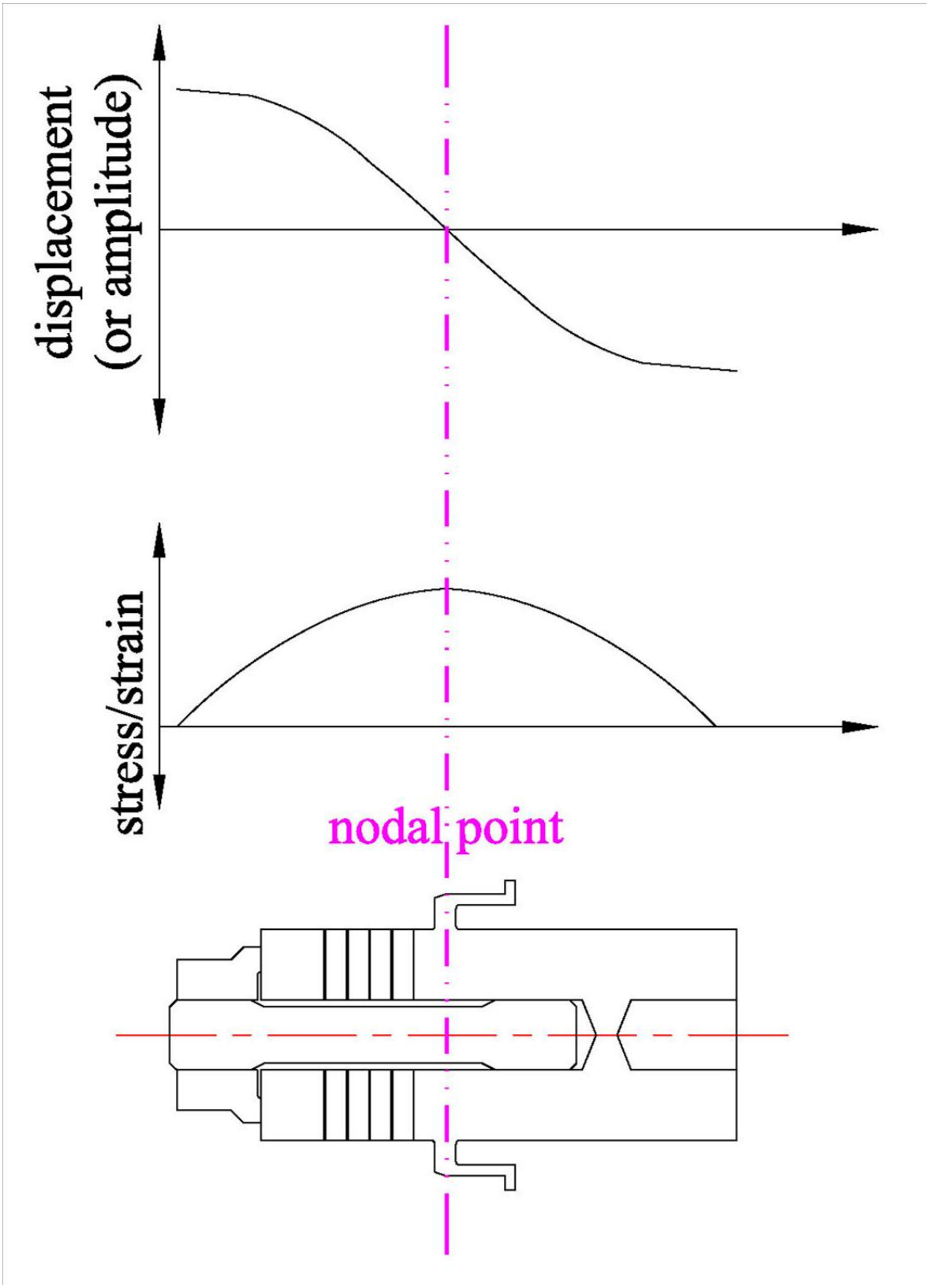

Figure 2.8 – Equivalent series and parallel resonance circuits

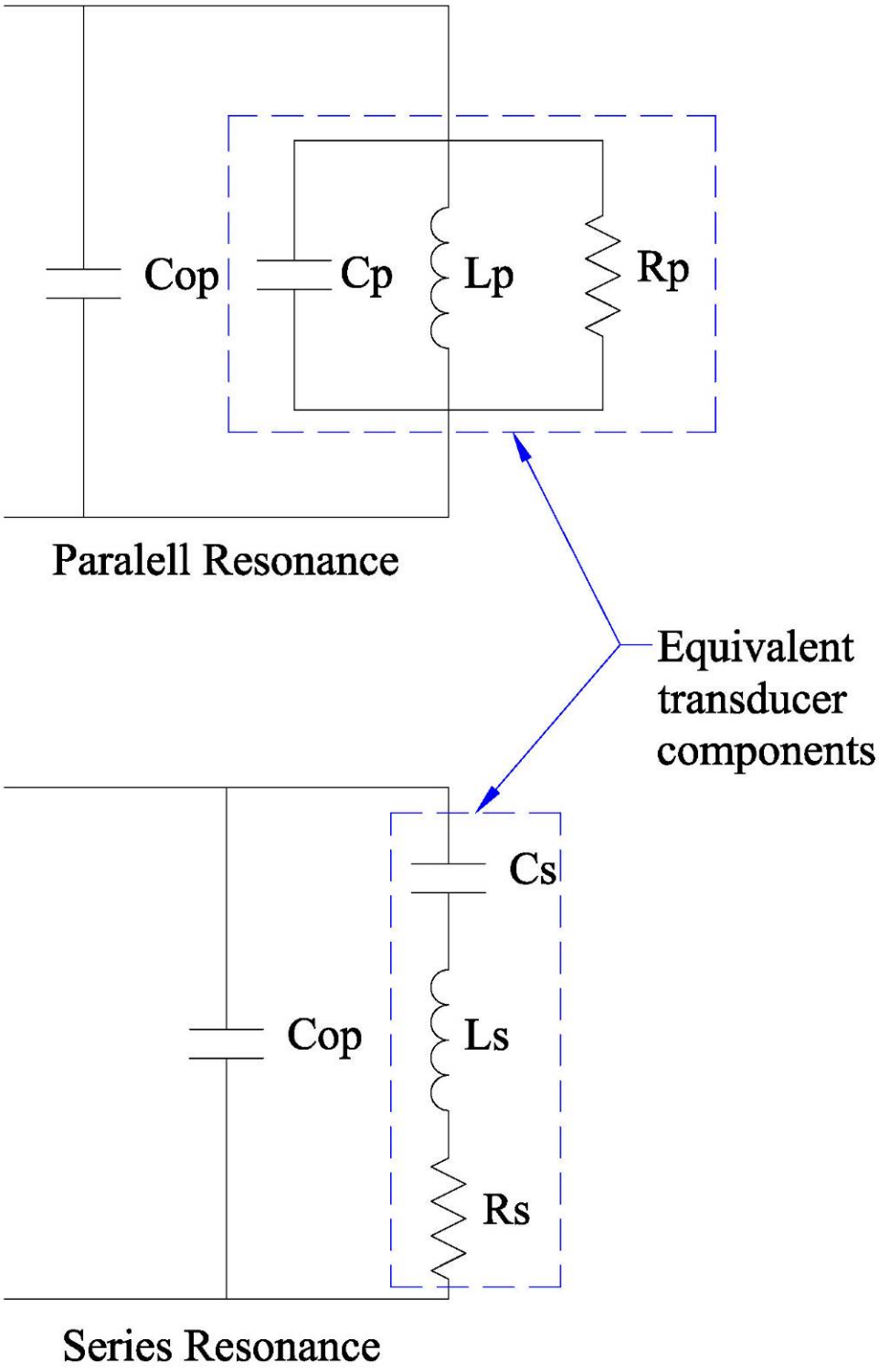

Figure 2.9 – Example impedance plot of transducer

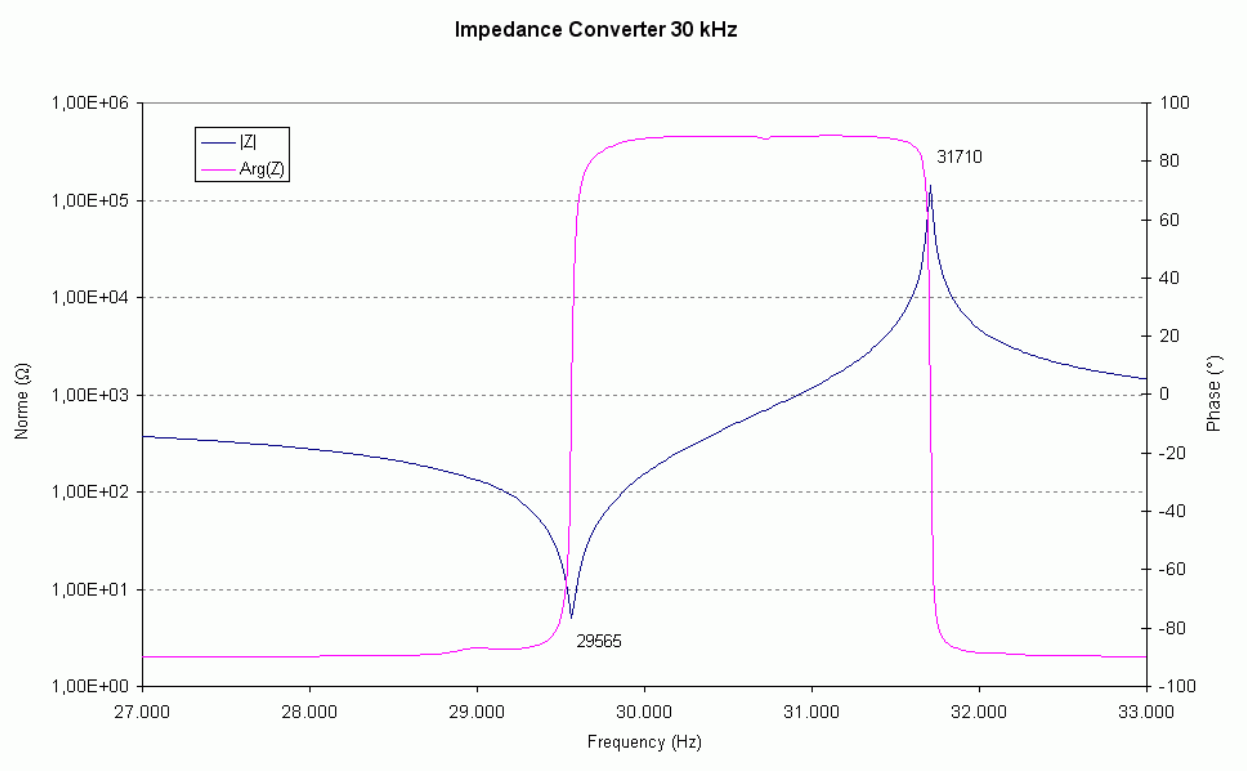

CHAPTER 3: FEA model of current 30 kHz transducer

3.1 Overview

The FEA analysis on the 30 kHz transducer being studied was performed using the academic version of ANSYS 12.1 APDL. Due to restrictions on the number of elements, only a 2-D axisymmetric model was produced. In ANSYS, the Y-axis (axis 2) is the axis of rotational symmetry, the X-axis (axis 1) represents the radial direction and the Z-axis is perpendicular to the plane produced by the Y-X axis. This must be carefully considered when entering material properties. A number of other scientific journal studies have been done using ANSYS on high powered transducers yielding very accurate results [24]. This was also verified by the consultant from JFS engineering [25]. Without a 3-D model, bending modes could not be detected, even if they fell within the operating frequency range of the transducer. This is another point considered when examining results. The titanium, beryllium and steel materials were modeled with PLANE42 elements, which are 2-D structural solid elements with 4 nodes and two degrees of freedom at each node – UX and UY. The piezoelectric PZT crystals were modeled as SOLID13 elements which are 2-D coupled field solids with 4 nodes and four degrees of freedom at each node - UX,UY,UZ and VOLT.

The 2-D geometry used throughout the modeling process is shown in figure 3.1. It was created with engineering drawings from HUG. The condition of the contact surfaces were defined based upon the analysis type. For the modal and dynamic analyses, the surfaces were considered perfectly coupled with no relative displacement. For the static pre-load analysis, the contact surfaces between the center nut and the steel reflector plate were considered. Also considered were the contact surfaces between the beryllium plates and piezoelectric PZT crystals. The polarization in the ceramics was configured as shown in figure 3.2.

The material properties were based upon both manufacturer specifications and data used in previous analyses by the engineering group at HUG and JFS engineering for similar calculations. They acquired these properties from the manufacture's specification sheets and from independent testing. All material properties have shown good correlation with laboratory test results. It is important to note that these properties will vary from lot to lot due to normal

manufacturing variations accounting for some slight variation in production transducers. Figure 3.3 shows the data sheet from Morgan Ceramics, who was the manufacturer of the PZT801 material. The piezoelectric charge constant in the direction of polarization (YY) and permittivity (PERY) shown in table 3.1 needed to be modified due to the compressive pre-load. The pre-load increased the value of both properties [25]. Before entering the data into ANSYS, it needed to be manipulated based upon ANSYS material data input requirements. The derivation can be found in Appendix A. The material properties entered into ANSYS for each material are shown in table 3.1.

For all analyses, the model was meshed with free quad shaped elements with a 0.7mm sized mesh. Mesh distribution was very even, as seen in figure 3.4.

3.2 Modal analysis results

The modal analysis was performed using the block Lanczos method under two separate boundary conditions to detect the series and parallel resonance frequencies. One boundary condition applied 0 volts to the top of each piezoelectric disk (open circuit or parallel conditions) and the second condition applied 0 volts to both the top and bottom of each disk (closed circuit or series conditions). The exact boundary condition locations are shown in figure 3.5, which points to the top and bottom of each conducting disk or plate. The modal analysis range was 0-60,000 Hertz to capture any modes close to the primary axial mode. Table 3.2 shows the resulting frequencies from the modal analysis under both boundary conditions. In this model, the series resonant frequency was at 29,787Hz and the parallel resonant frequency was at 31,937Hz. Figures 3.6 and 3.7 show deformed plots for Y-displacement at full extension and compression for series and parallel modes of vibration respectively. Images of alternate modes of vibration can be found in Appendix B. The next closest mode was almost 24,000 Hz away under both boundary conditions and do not need to be considered.

3.3 Harmonic analysis results

Based upon the resonant frequencies calculated in the modal analysis, a harmonic analysis was done from 29,000 Hertz to 33,000 Hertz in 20 hertz increments to capture both resonant points and at an applied voltage of 850 volts peak or 650 volts rms. This is the voltage output by the

current HUG designed generator under no load conditions, i.e. when it is only vibrating the transducer. The high voltage was applied to the top of each piezoelectric crystal while 0 volts were applied to the bottom of each crystal. The results were used to create an impedance plot and a plot of the amplitude or y-displacement at the coupling surface over this frequency range. The Herrmann welding system is designed based upon 7.5 microns of amplitude at the coupling surface or face of the transducer, therefore the dynamic stresses were evaluated at this point. Both the impedance plot and the amplitude plots will be checked and compared to actual components in the analysis section.

The harmonic analysis was performed with a frontal solver using a full solution method with stepped boundary conditions. The resulting impedance plot is shown in figure 3.8. The impedance is calculated from the voltage boundary condition and a calculation for the current based upon the charge. The plot of the amplitude or y-displacement at the coupling surface is shown in figure 3.9. Figure 3.10 is another amplitude plot from 30,650 to 30,750 hertz with 1 hertz increments to find the exact frequency producing 7.5 microns. This plot clearly shows that 30,700 hertz is the correct point. Figure 3.11 shows the Von mises stress distribution with maximum displacement at 30,700 Hertz. Figure 3.12 shows the same distribution only within the piezoelectric transducer crystals to more clearly illustrate this critical area.

3.4 Static pre-stress analysis results

The pre-stress analysis was performed using the pre-tension element feature in ANSYS to apply a tensile force of 44 kN within the central bolt/stud by using a master node located underneath the coupling surface. The voltage at the top of each piezoelectric ceramic was set to 0 volts and the bottom of each ceramic was left unconstrained, which created an open circuit boundary condition. The contact surface behavior was set-up to include initial penetration using an augmented Lagrange contact algorithm with standard contact surface behavior and the contact stiffness updated with each iteration. The analysis converged on a solution within 10 iterations. The overall Von mises stress distribution is shown in figure 3.13. Figure 3.14 shows the same stress distribution only in the piezoelectric ceramic disks. To more clearly see the pressure distribution effect, figure 3.15 shows the contact pressure distribution in the tensioning nut and

ceramic interfaces. Figure 3.16 shows the contact pressure at the bottom of each ceramic disk and figure 3.17 shows the contact pressure at disk #1 and disk #4.

3.5 Calculated stress limit and safety factor in the piezoelectric crystals

As mentioned previously, there are two primary modes of failure seen under production conditions in a welding transducer - cracking and/or shifting piezoelectric ceramic disks. The theoretical failure point will occur when the contact stress at one point becomes zero and the two surfaces at that point become uncoupled. This causes rapid heating and mechanical damage which leads to cracking. The other theoretical failure point will occur when the contact pressure over an entire surface is zero or no longer compressive, which would allow the crystal to shift its position due to lack of a restraining force. Two theoretical failure points that will not be examined in this thesis include exceeding the tensile stress at some localized region inside the crystal and exceeding the shear stress limit due to bending or twisting.

These failure points and corresponding safety factors can be calculated from the results of the static and harmonic analyses. Even though both dynamic and static stresses were calculated separately, they can be summed to produce a good approximation of the total stress during actual vibration, which can be visualized in figure 3.18. Using the calculated nodal stress values in the y-direction from both the static analysis at 44 kN and the harmonic analyses at 30,700 hertz, the stress at the ceramic interfaces can be calculated. These results determine how much the stress would have to increase in order to reach an uncompressed state at one point or across an entire surface. Because of the linear relationship between the ceramic stress and strain, this summation provides a safety factor which can be directly correlated to an amplitude limit not to be exceeded before failure occurs. For example, a safety factor of 200% indicates the amplitude or strain would have to double, which would in turn double the stress. The raw nodal calculation data can be found in appendix C. The graphs in figure 3.19 show the y-direction contact stresses at each interface along with the safety factor in percent and dotted lines indicating the localized failure point and the shifting failure point. The crystals are labeled as #1 for the disk closest to the top pre-tension nut and then in descending order, where disk #4 is the disk against the titanium body as shown in figure 3.2.

3.6 Tables and figures

Table 3.1 – Material properties used in FEA analysis - (a) Basic mechanical properties of PZT801, (b) Elasticity matrix for PZT801, (c) Piezoelectric stress matrix for PZT801, (d) Permittivity matrix for PZT801, (e) Material properties for beryllium, titanium and steel

(a)

Material:	Model type:	Density (kg/m^3):	Damping constant:
17 - PZT801 piezoelectric ceramic	Linear anisotropic	7700	5.00E-10

(b)

PZT - Elasticity matrix (Pa):					
1.469E+11	8.105E10	8.109E10	0	0	0
-	1.317E11	8.105E10	0	0	0
-	-	1.469E11	0	0	0
-	-	-	3.135E10	0	0
-	-	-	-	3.135E10	0
-	-	-	-	-	3.067E10

(c)

PZT - Piezoelectric stress matrix (C/N):			
	X	*Y*	*Z*
X	0.00	-1.04	0.00
Y	0.00	18.52	0.00
Z	0.00	-1.04	0.00
XY	9.40	0.00	0.00
YZ	0.00	0.00	9.40
XZ	0.00	0.00	0.00

Table 3.1 (cont'd)

(d)

PZT - Permittivity (F/m):	
PERX	790
PERY	704
PERZ	790

(e)

Material:	Model type:	Density (kg/m^3):	Damping constant:	Poisson's ratio:	Elasticity (Pa):
18 - Beryllium-Copper	Linear isotropic	8250	1.00E-09	0.3	1.30E+11
19 - Titanium, TiAl6V4	Linear isotropic	4400	1.00E-09	0.334	1.154E+11
20 - Steel, 90MnCrV8	Linear isotropic	7800	1.00E-06	0.3	2.10E+11

Table 3.2 – modal frequencies under open and closed circuit boundary conditions (yellow highlighted row is primary mode) – (a) Series modal frequencies, (b) Parallel modal frequencies

(a) Series modal frequencies				
SET	TIME/FREQ	LOAD	STEP	SUBSTEP
1	3.68E-03	1	1	1
2	29787	1	2	2
3	54424	1	3	3
4	57659	1	4	4

(b) Parallel modal frequencies				
SET	TIME/FREQ	LOAD	STEP	SUBSTEP
1	3.44E-03	1	1	1
2	31937	1	2	2
3	55321	1	3	3

Figure 3.1 – 2-D axisymmetric geometry of 30 kHz transducer

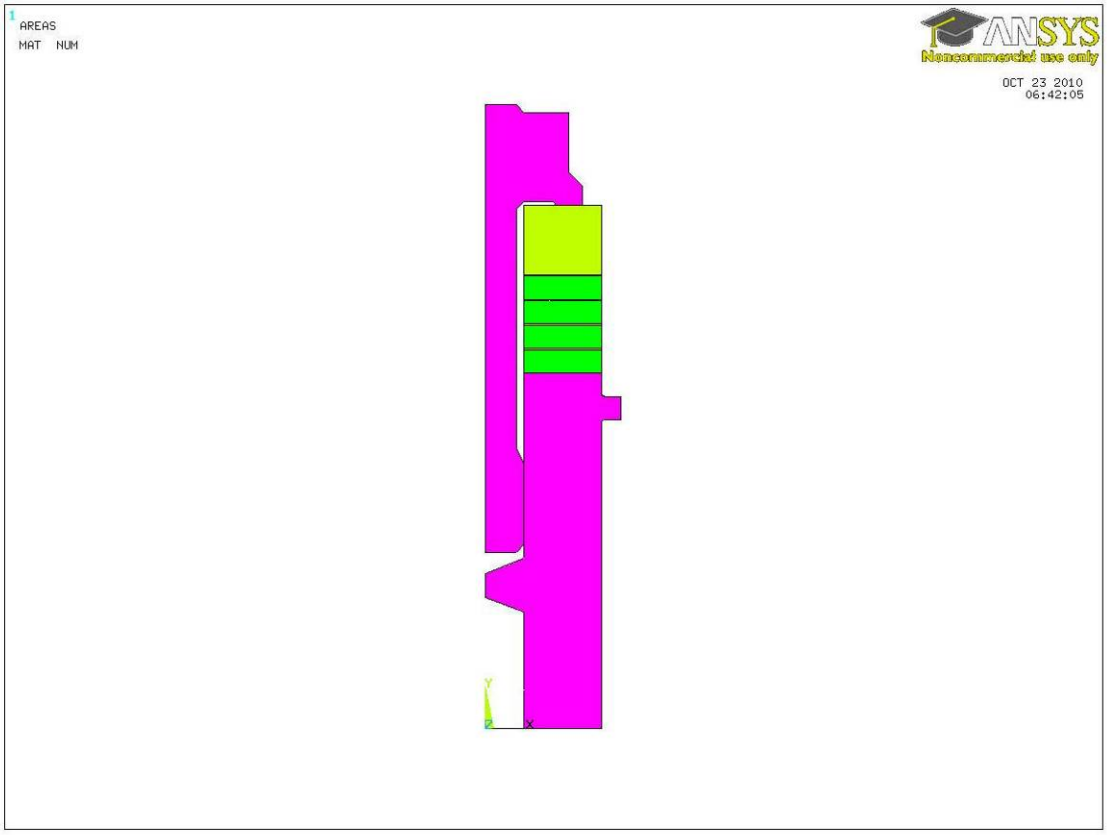

Figure 3.2 – Configuration of polarized PZT crystals for FEA analysis

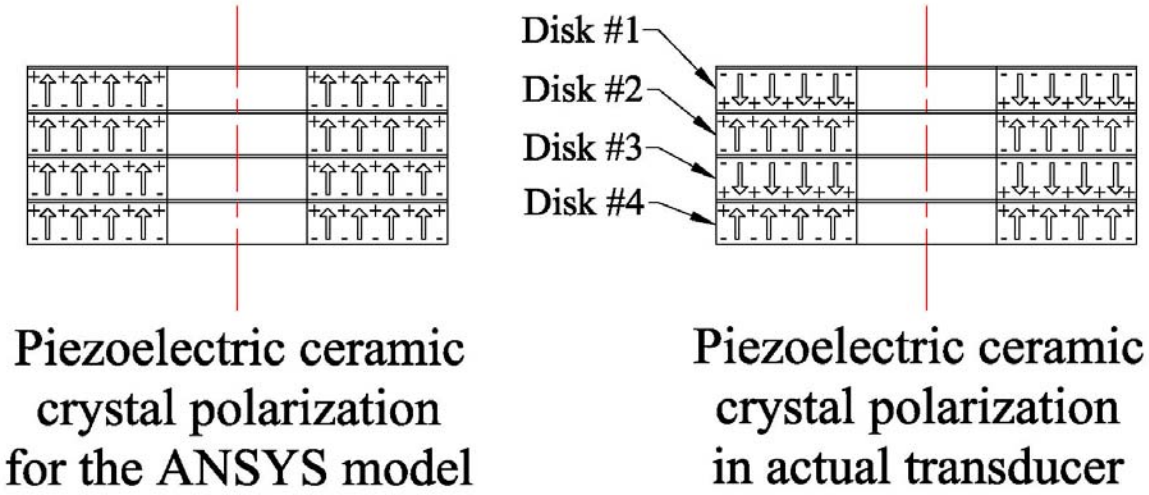

Figure 3.3 – Morgan Ceramics PZT801 data sheet

Property	Symbol	Unit	PZT801
No of days after poling			**1**
Electrical - Low Field			
Relative Permittivity	$\varepsilon_r^T{}_{33}$		1000
Relative Permittivity	$\varepsilon_r^T{}_{11}$		
Dielectric Loss	Tan δ		0.004
Resistivity (at 25°)	ρ el	Ωm	10^{10} (at 25°C)
Resistivity (at 100°)	ρ el	Ωm	
Resistivity (at 200°)	ρ el	Ωm	
Electrical - High Field			
Increase in $\varepsilon_r^T{}_{33}$ @ 2KV/cm		%	
Dielectric Loss @ 2KV/cm	Tan δ		
Increase in $\varepsilon_r^T{}_{33}$ @ 4KV/cm		%	
Dielectric Loss @ 4KV/cm	Tan δ		0.009
Electro-Mechanical			
Coupling Factors	k_p		0.51
	k_{15}		0.55
	k_{31}		0.30
	k_{33}		0.64
	k_t		
Charge Constants	d_{33}	x 10^{-12} C/N	225
or Strain Constants	d_{31}	x 10^{-12} C/N or m/V	-97
	d_h	x 10^{-12} C/N	31
	d_{15}	x 10^{-12} C/N or m/V	330
Voltage Constants	g_{33}	x 10^{-3} Vm/N	25.4
or Stress Constants	g_{31}	x 10^{-3} Vm/N	-10.9
	g_h	x 10^{-3} Vm/N	3.6
	g_{15}	x 10^{-3} Vm/N	28.9
	$d_h g_h$	x 10^{-15}	112
Frequency Constants	N_p	Hz.m	2340
	N_1	Hz.m	1700
	N_3	Hz.m	
	N_a	Hz.m	2000
	N_{3t} or N_{33}	Hz.m	2070
	N_s	Hz.m	
	Hoop or N_c	Hz.m	1070
	N_t	Hz.m	
Compressive Strength		10^6 Pa	
Tensile Strength		10^6 Pa	
Quality Factor	Q_m		1000
Mechanical			
Compliances	$S^E{}_{33}$	x 10^{-12} m^2/N	13.5
	$S^E{}_{11}$	x 10^{-12} m^2/N	11.5
	$S^E{}_{12}$	x 10^{-12} m^2/N	
	$S^E{}_{13}$	x 10^{-12} m^2/N	
	S^{E55}	x 10^{-12} m^2/N	
	S^{E66}	x 10^{-12} m^2/N	
	$S^D{}_{33}$	x 10^{-12} m^2/N	8.5
	$S^D{}_{11}$	x 10^{-12} m^2/N	10.1
	$S^D{}_{12}$	x 10^{-12} m^2/N	
	S_{66}	x 10^{-12} m^2/N	
	$Y^E{}_{33}$	x 10^{10} N/m^2	7.4
	$Y^E{}_{11}$	x 10^{10} N/m^2	8.7
	$Y^D{}_{33}$	x 10^{10} N/m^2	11.8
	$Y^D{}_{11}$	x 10^{10} N/m^2	9.9
Poisson's Ratio σ			
Density	ρ	kg/m^3	7600

Figure 3.4 – Meshed geometry

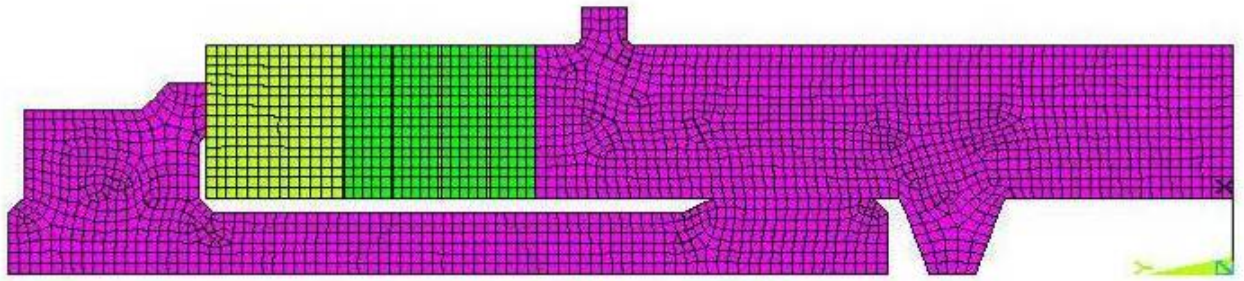

Figure 3.5 – Boundary conditions during modal analysis

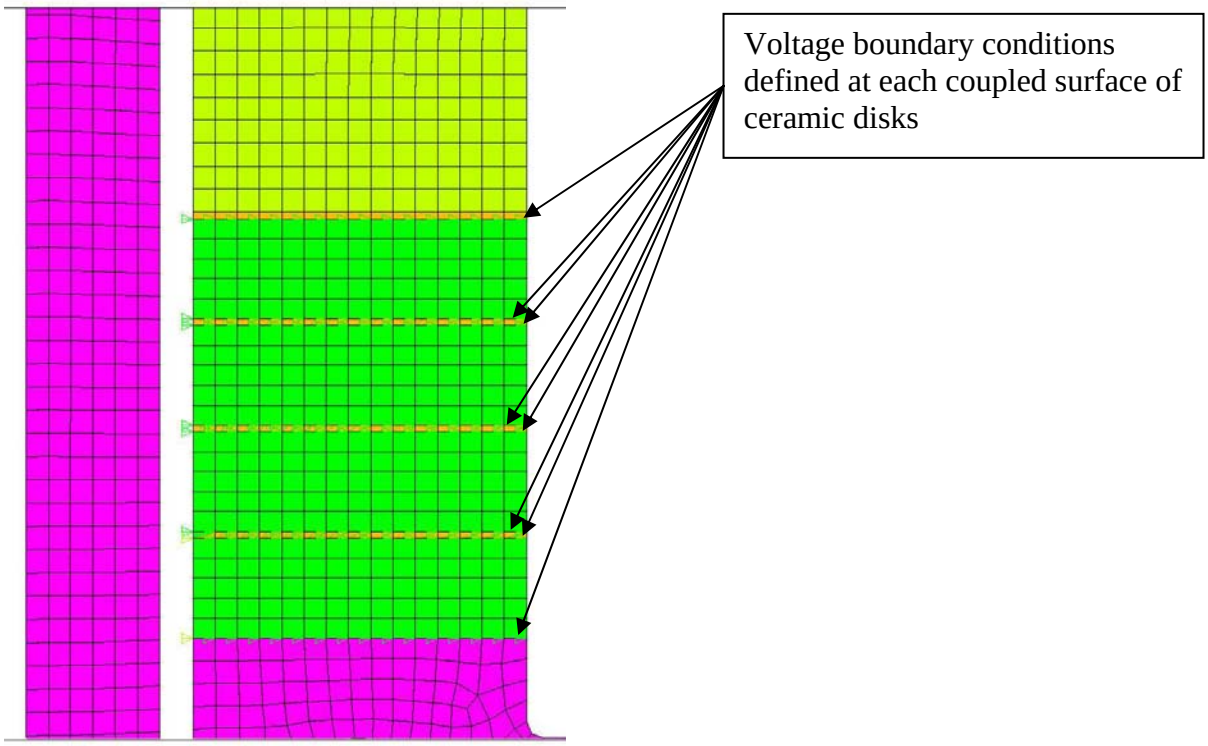

Figure 3.6 – Series modal vibration plots – (a) fully extended modal shape at series resonance, (b) fully compressed modal shape at series resonance

(a)

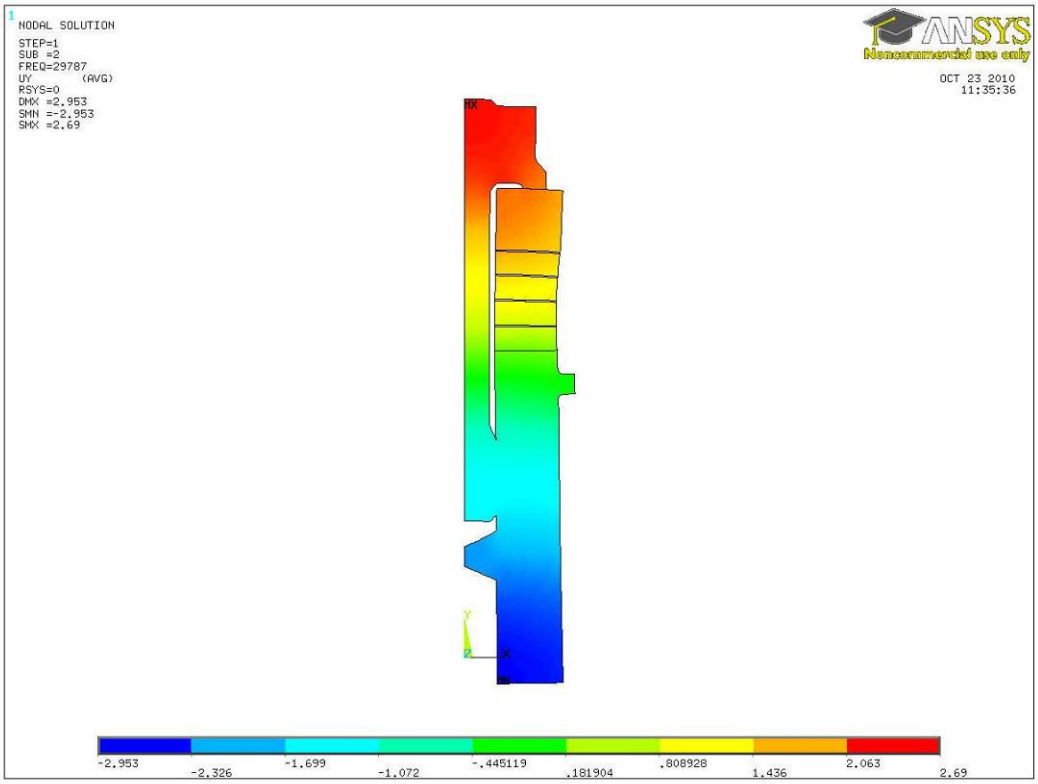

(b)

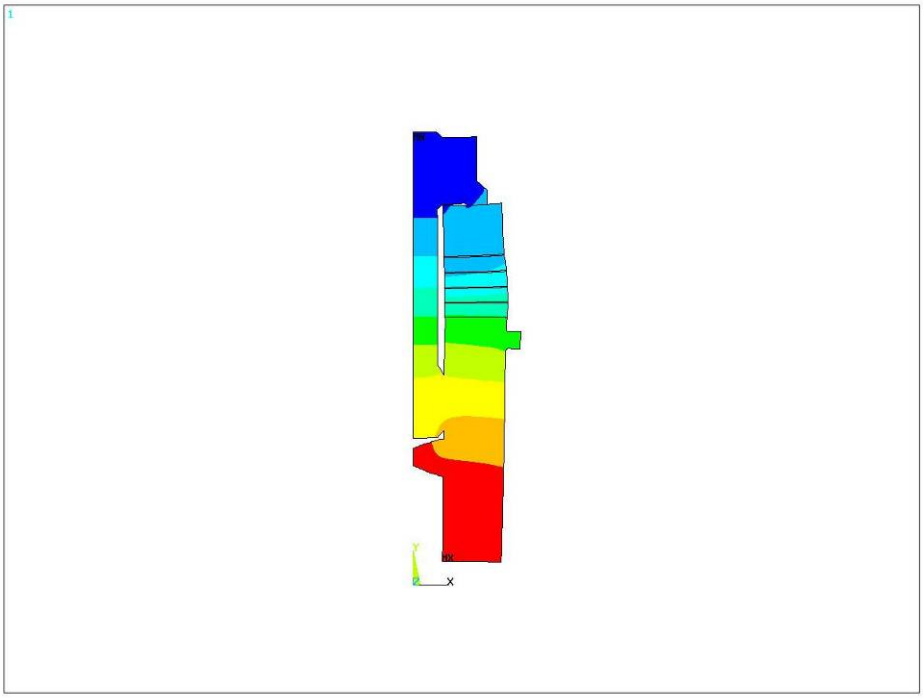

Figure 3.7 – Parallel modal vibration plots – (a) Fully extended modal shape at parallel resonance, (b) fully compressed modal shape at series resonance

(a)

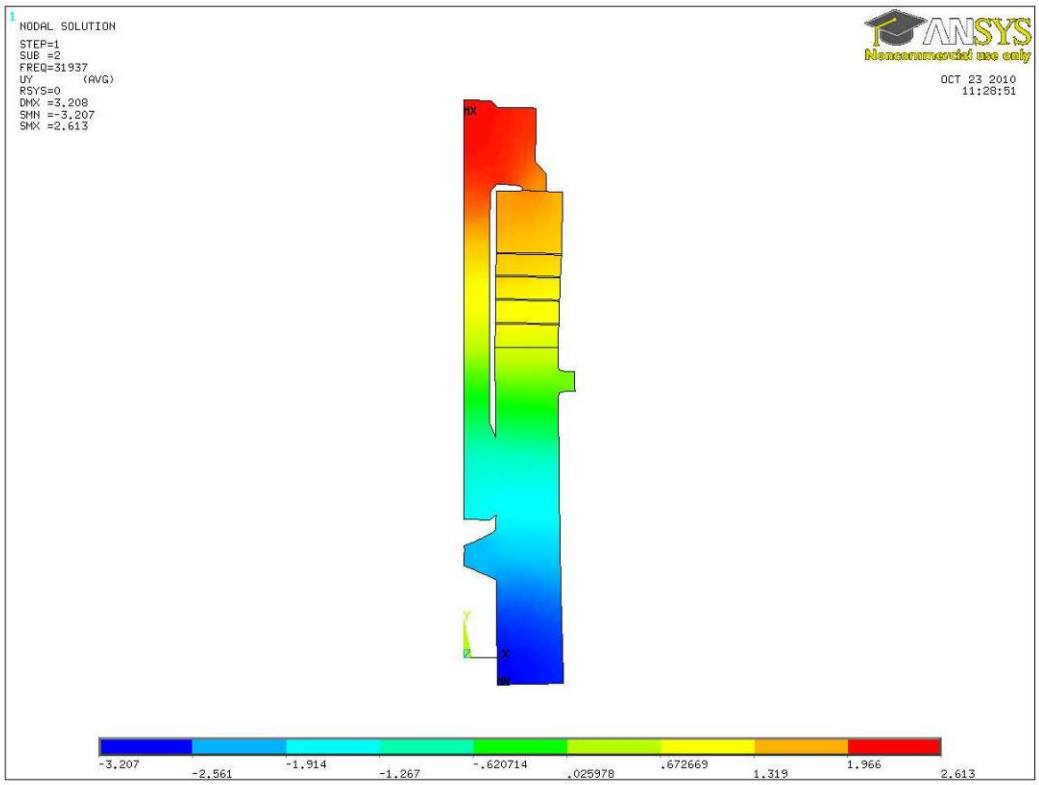

(b)

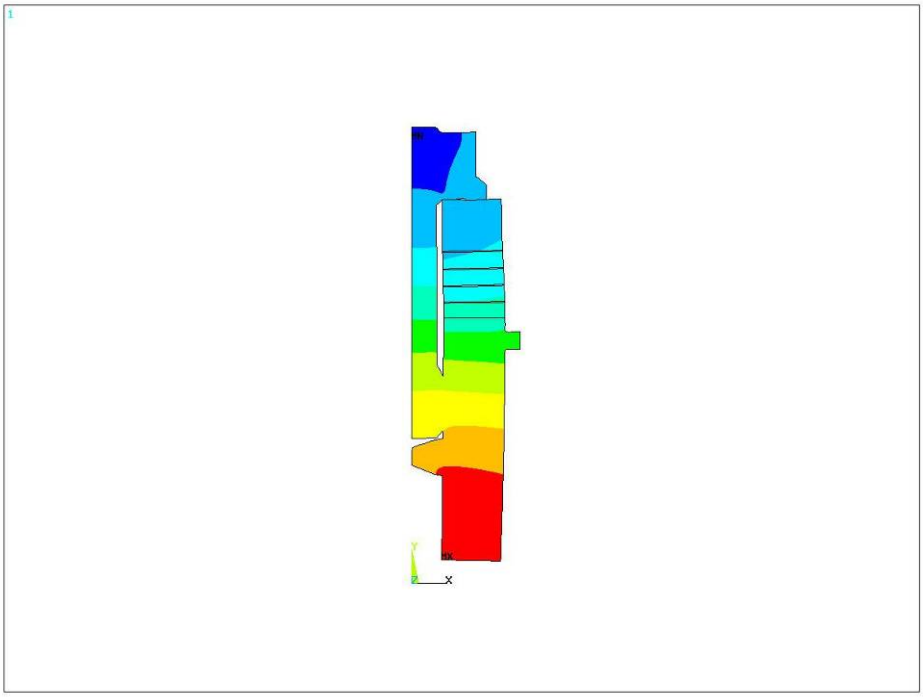

Figure 3.8 – Impedance versus frequency plot from 29,000-33,000 Hz

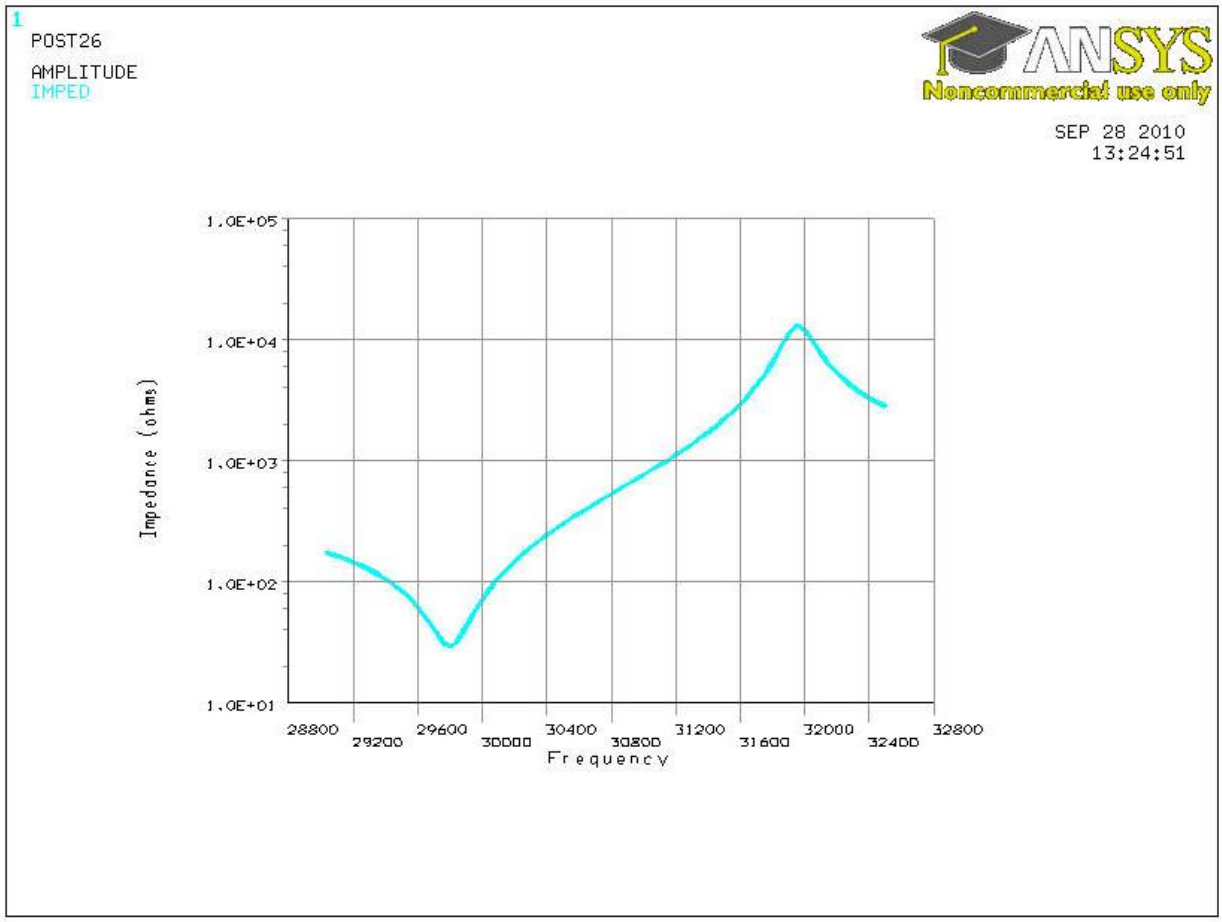

Figure 3.9 – Amplitude versus frequency plot from 29,000-33,000 hertz

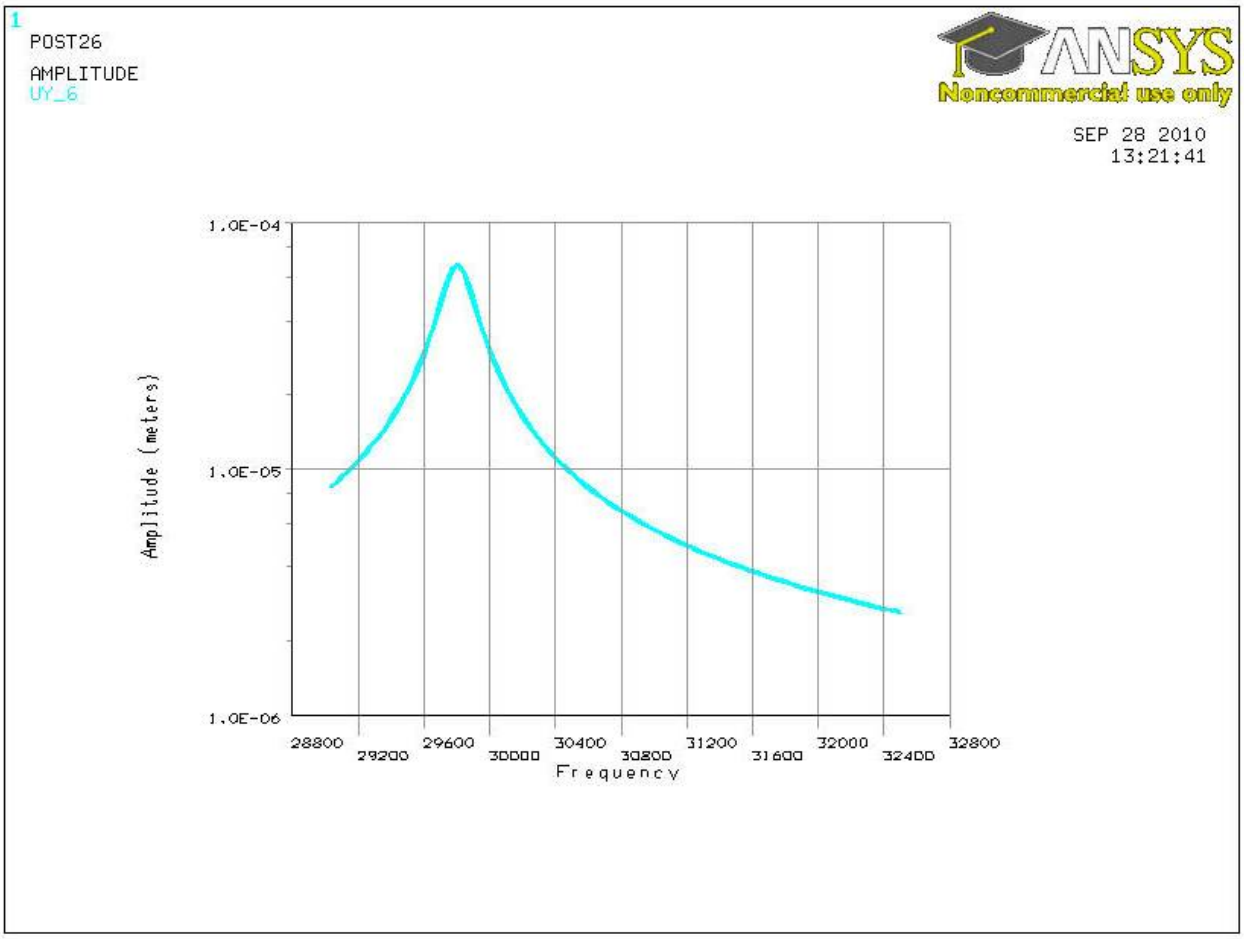

Figure 3.10 – Amplitude versus frequency from 30,650-30,750 hertz

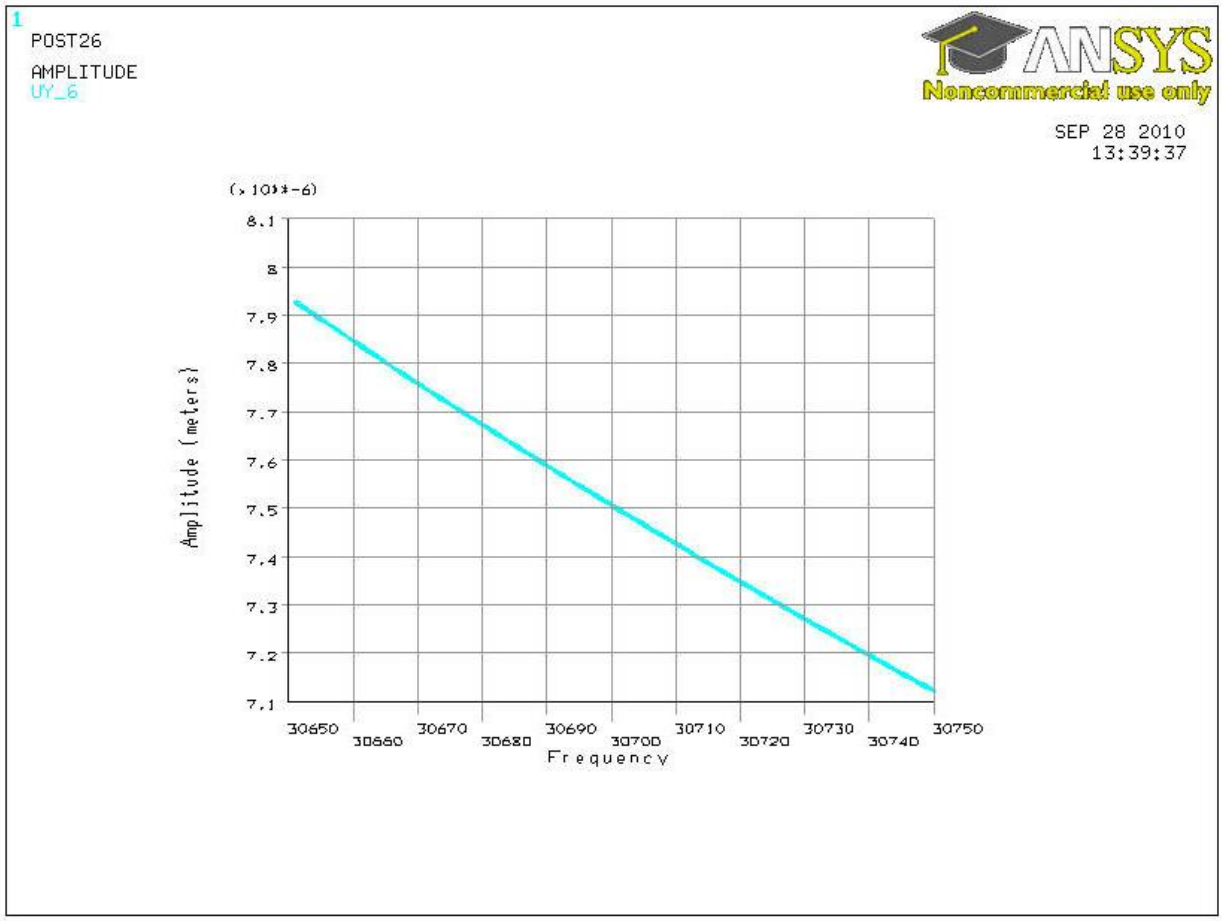

Figure 3.11 – Von Mises stress distribution at 30,700 hertz

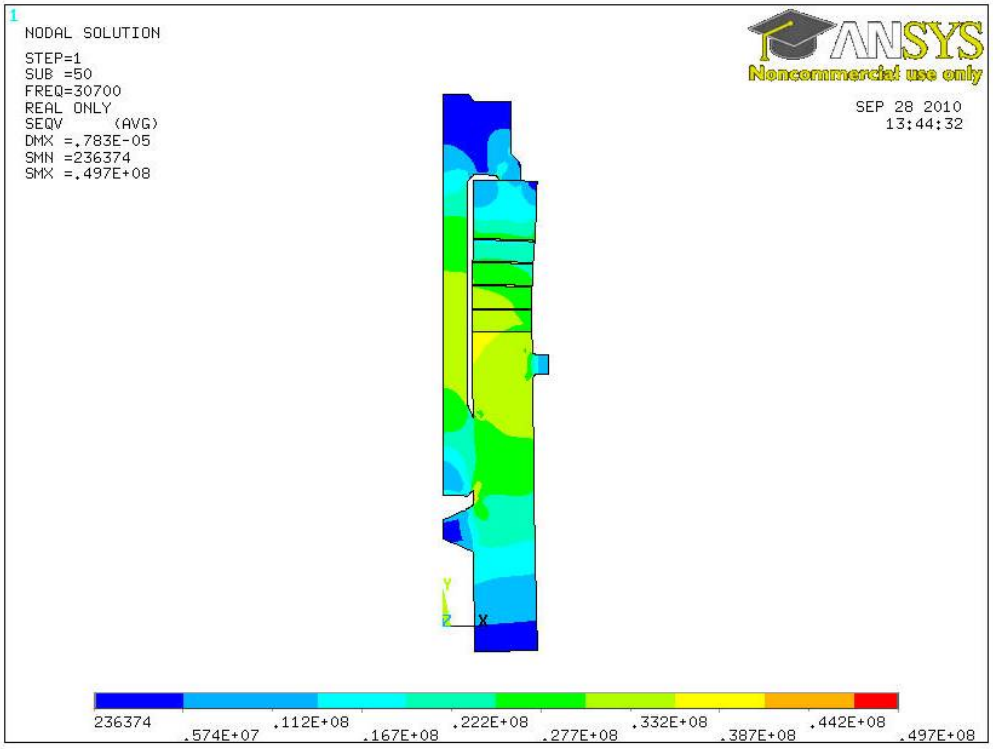

Figure 3.12 – Von Mises stress distribution at 30,700 hertz, only showing piezoelectric crystals

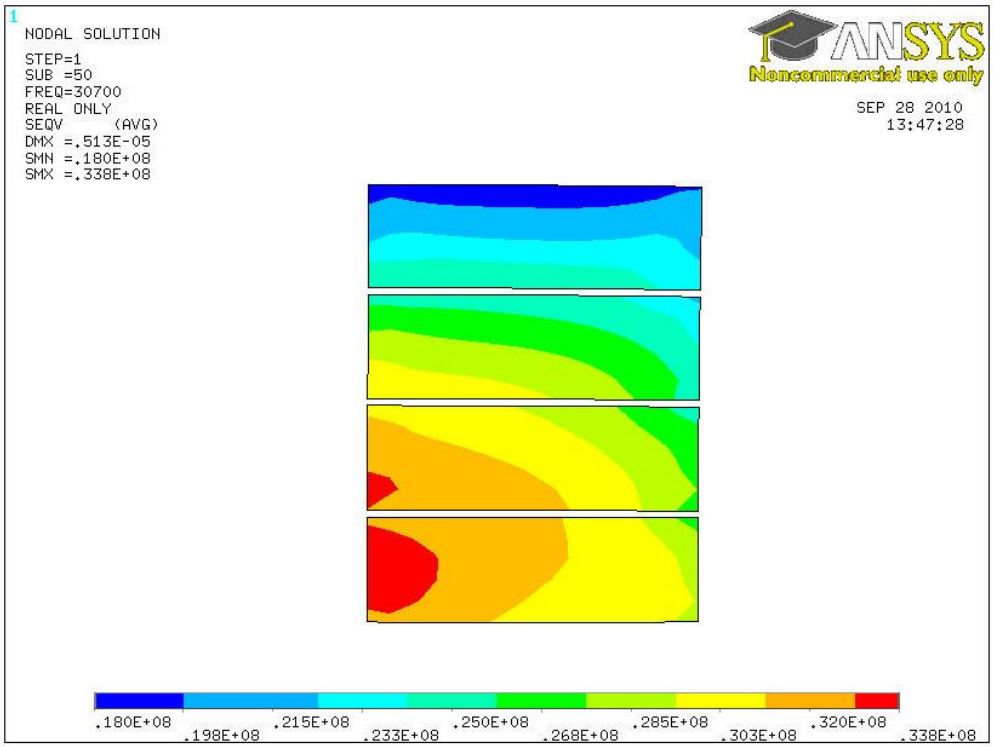

Figure 3.13 – Von Mises stress distribution under static load over entire model

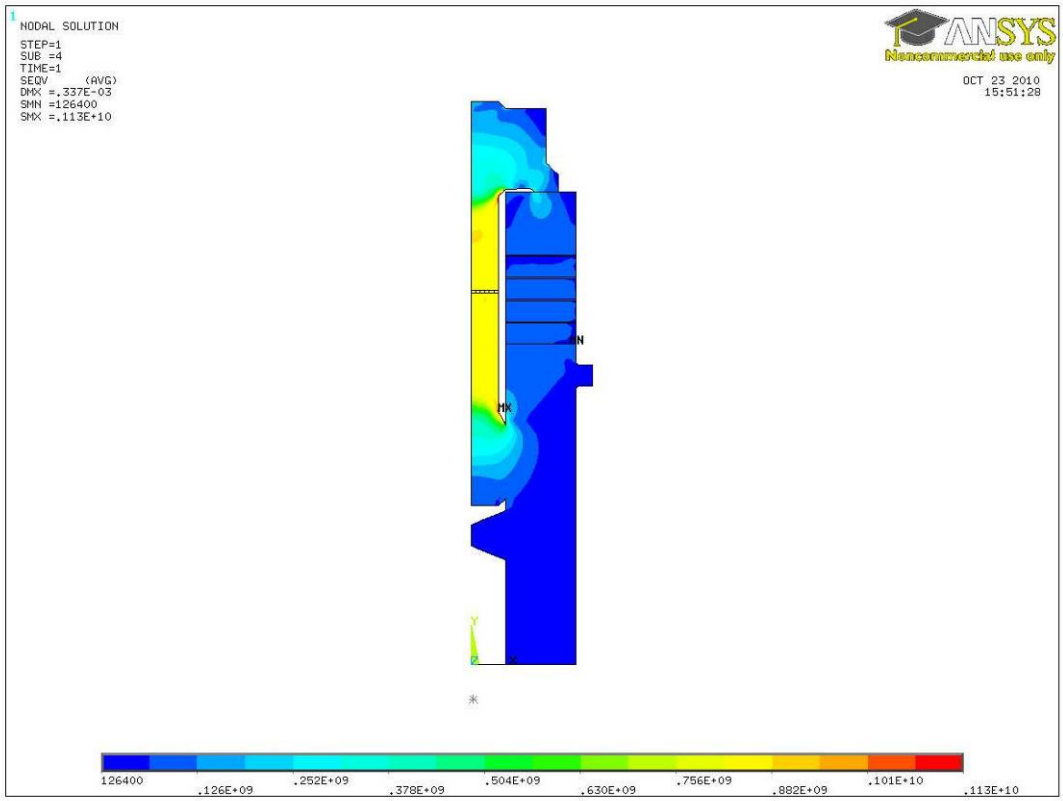

Figure 3.14 – Von Mises stress distribution under static load at ceramic crystals

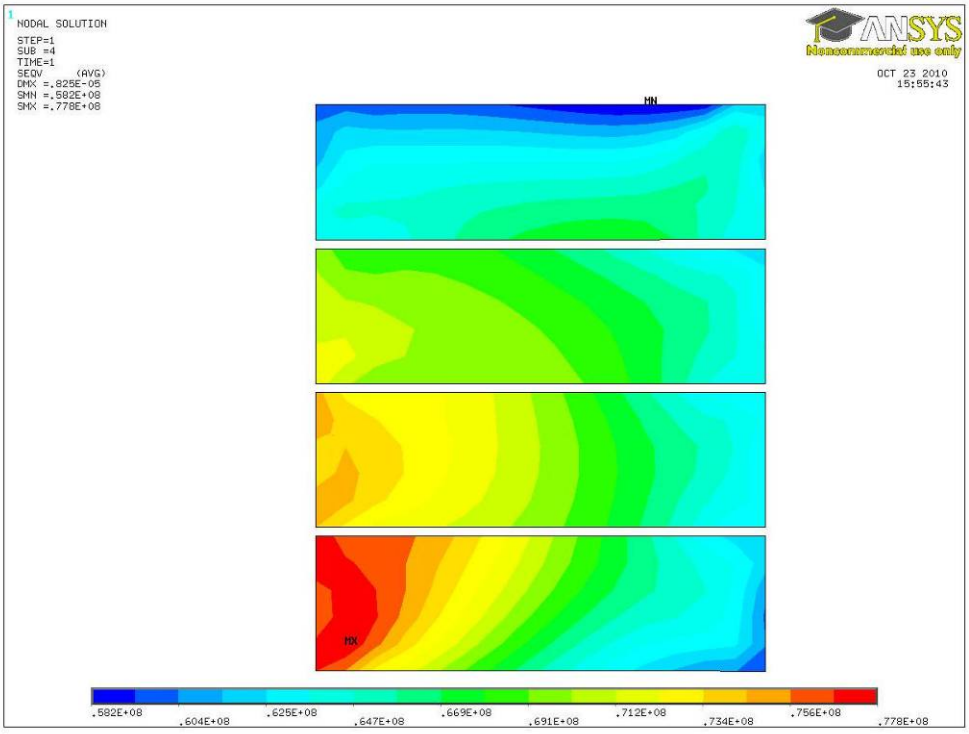

Figure 3.15 – Contact pressure over entire model under static load

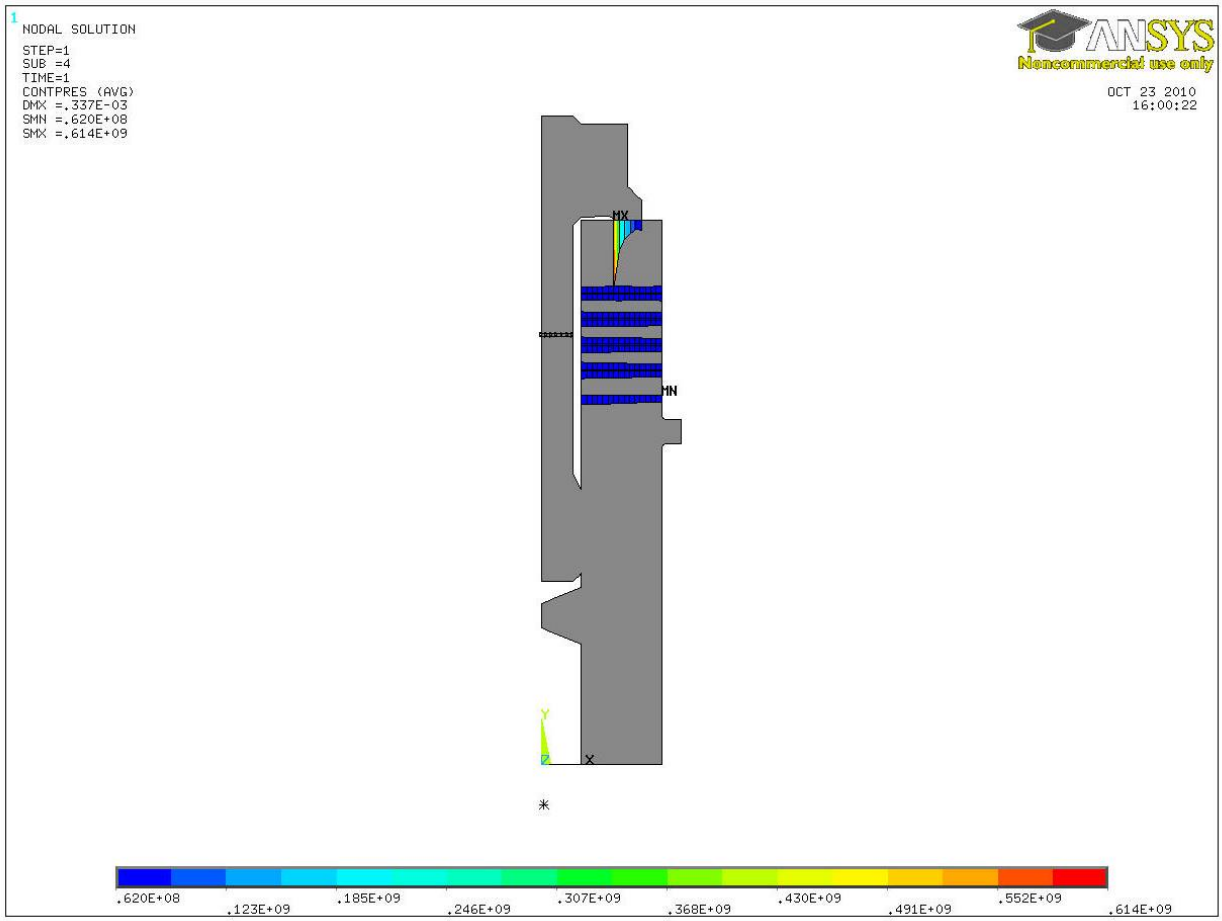

Figure 3.16 – Contact pressure at bottom of each crystal under static load

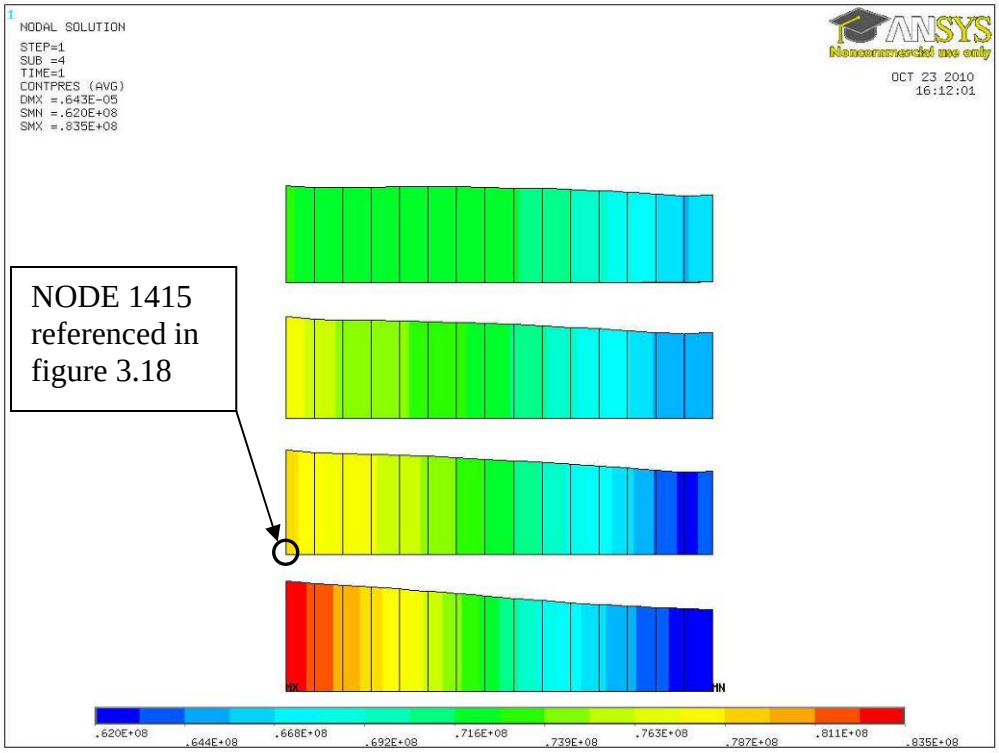

Figure 3.17 – Contact pressure at disk #1 and disk #4

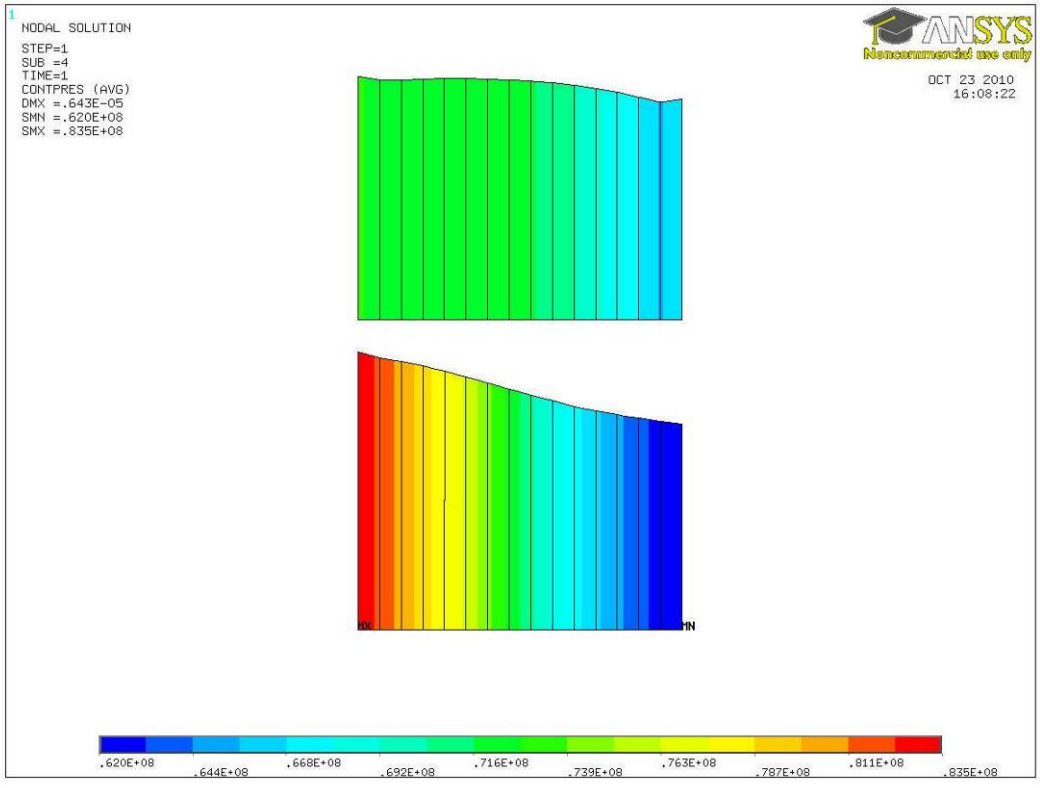

Figure 3.18 – Graphs illustrating summing of static and dynamic stresses to calculate total stress – (a) Static and dynamic loads separated, (b) Static and dynamic loads combined

(a)

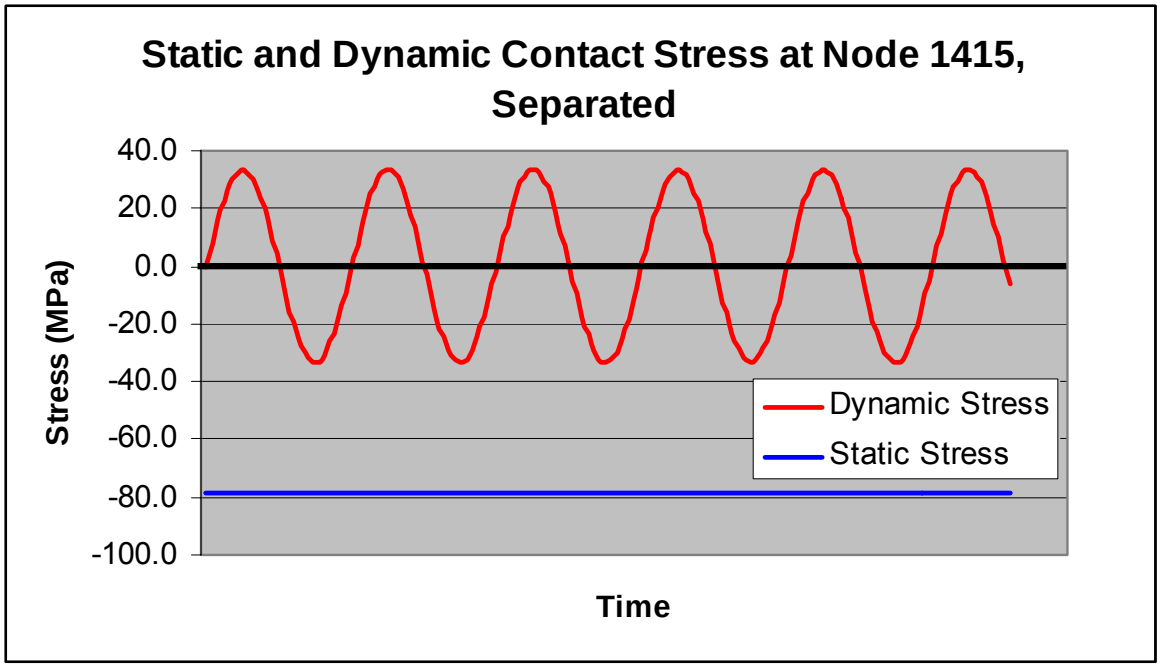

(b)

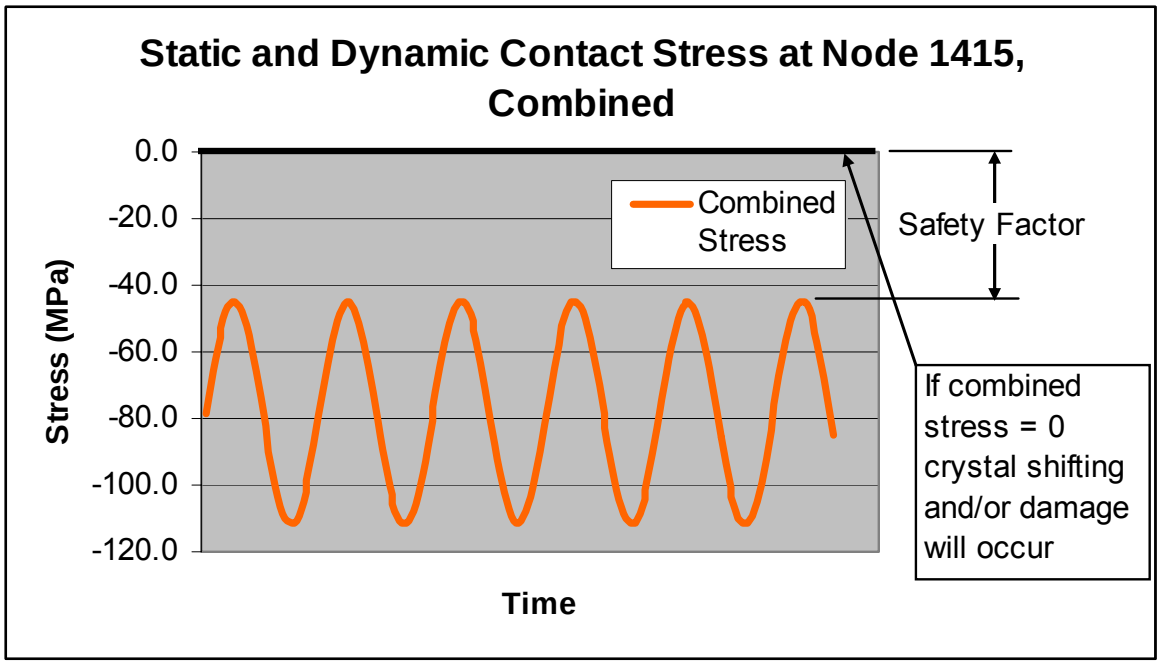

Figure 3.19 – Static and dynamic contact pressure between ceramics including safety factor – (a) Top of disk #1, (b) Bottom of disk #1, (c) Top of disk #2, (d) Bottom of disk #2, (e) Top of disk #3, (f) Bottom of disk #3, (g) Top of disk #4, (h) Bottom of disk #4

(a)

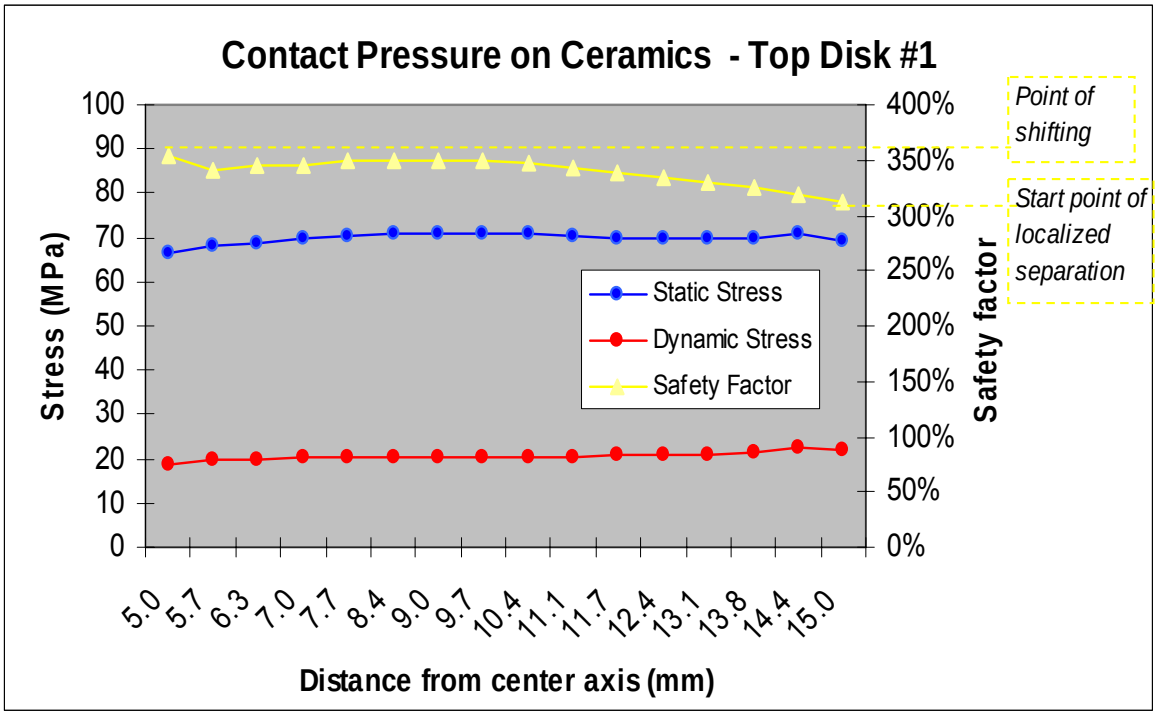

(b)

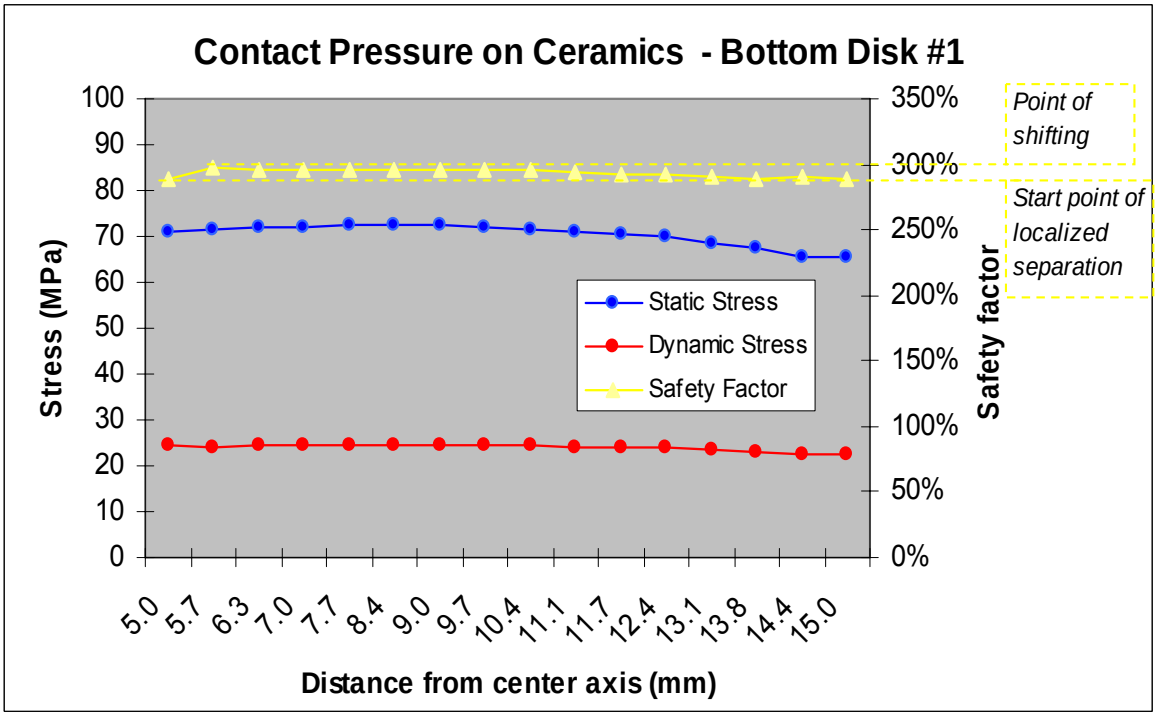

Figure 3.19 (cont'd)

(c)

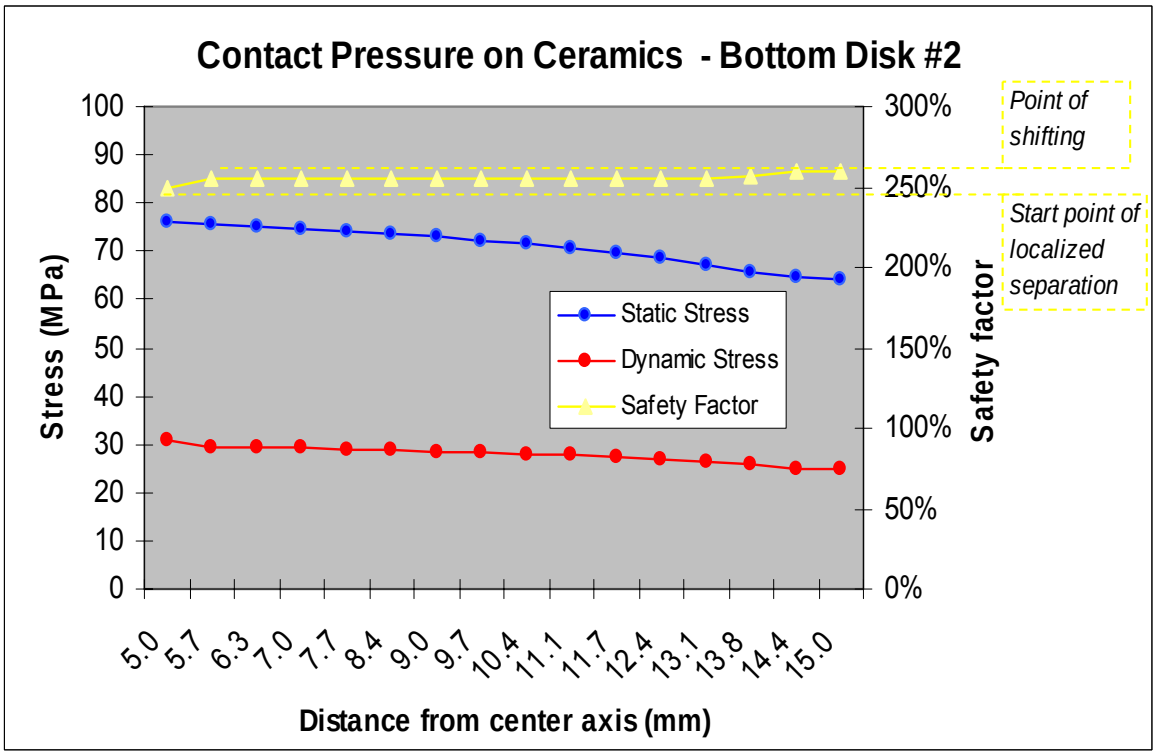

(d)

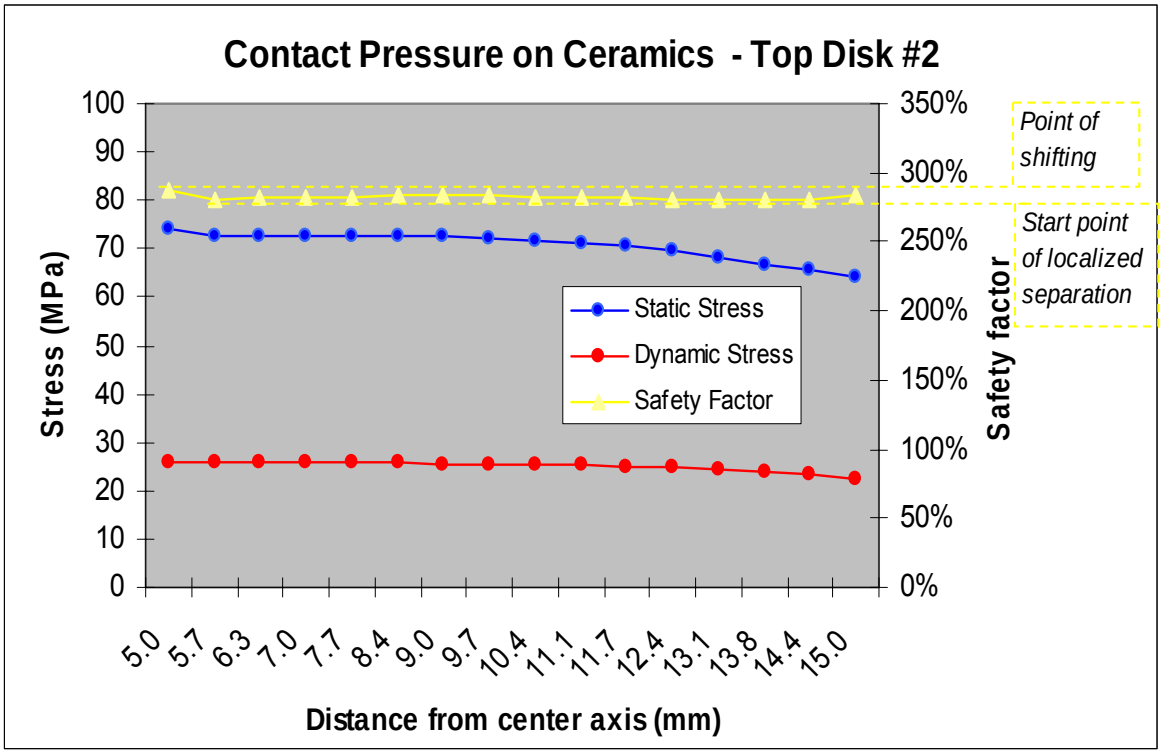

Figure 3.19 (cont'd)

(e)

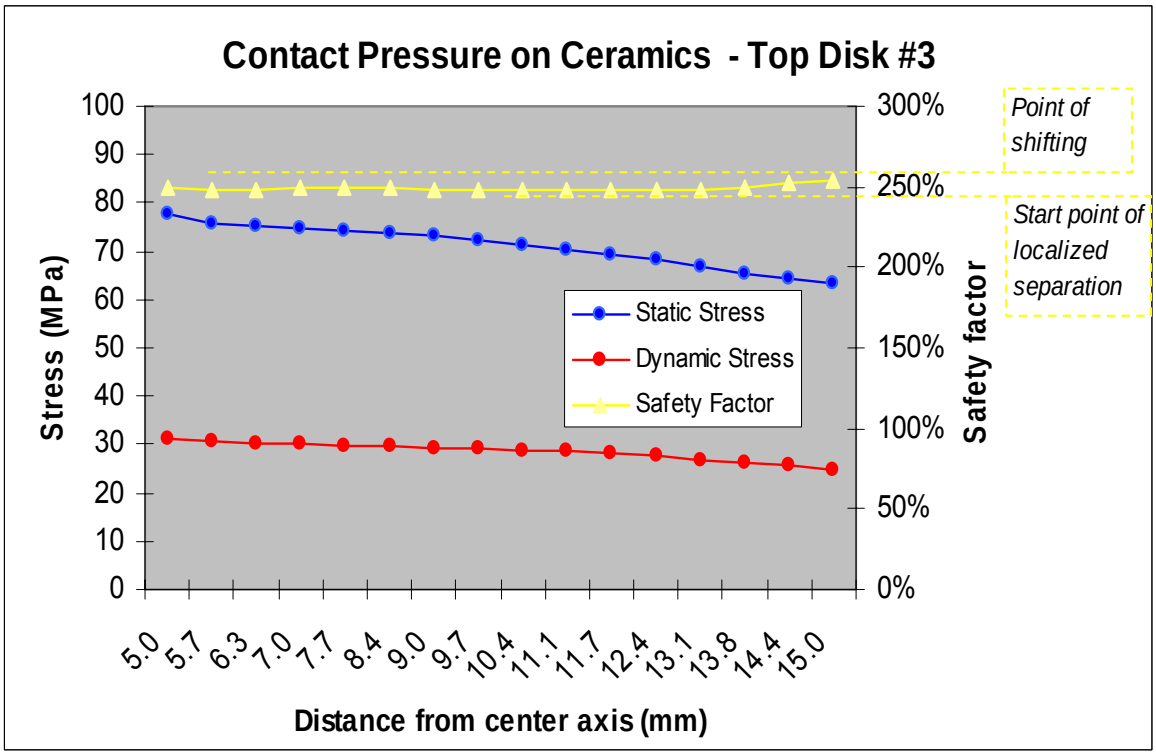

(f)

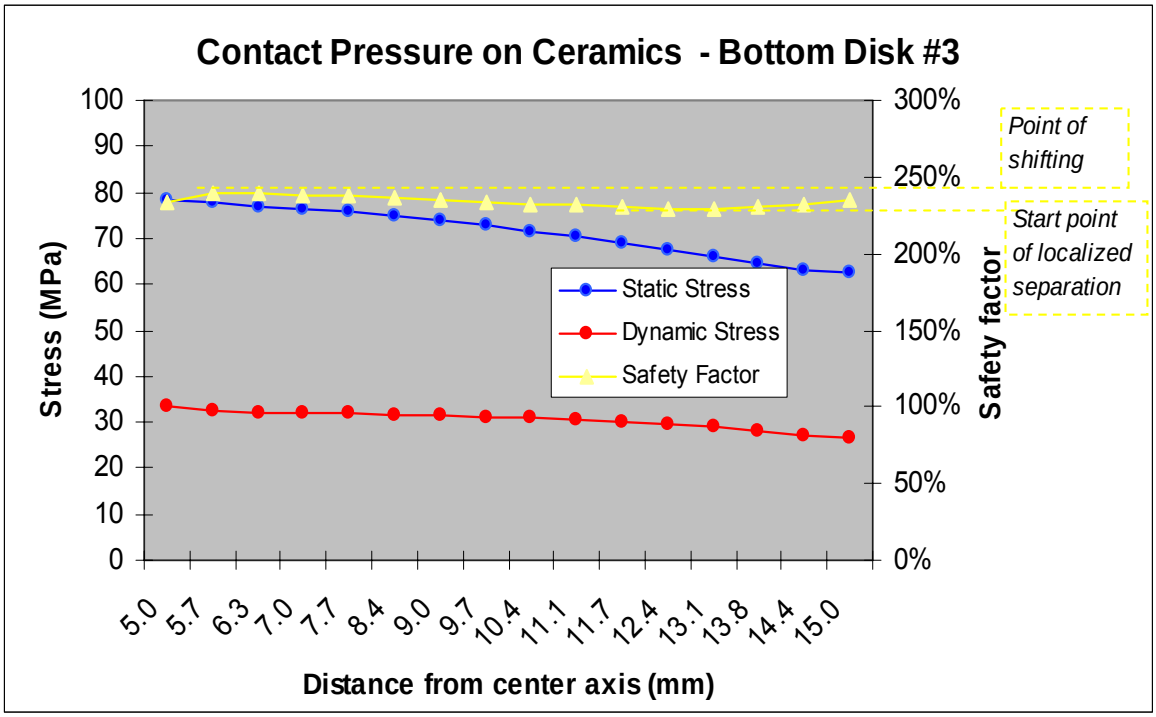

Figure 3.19 (cont'd)

(g)

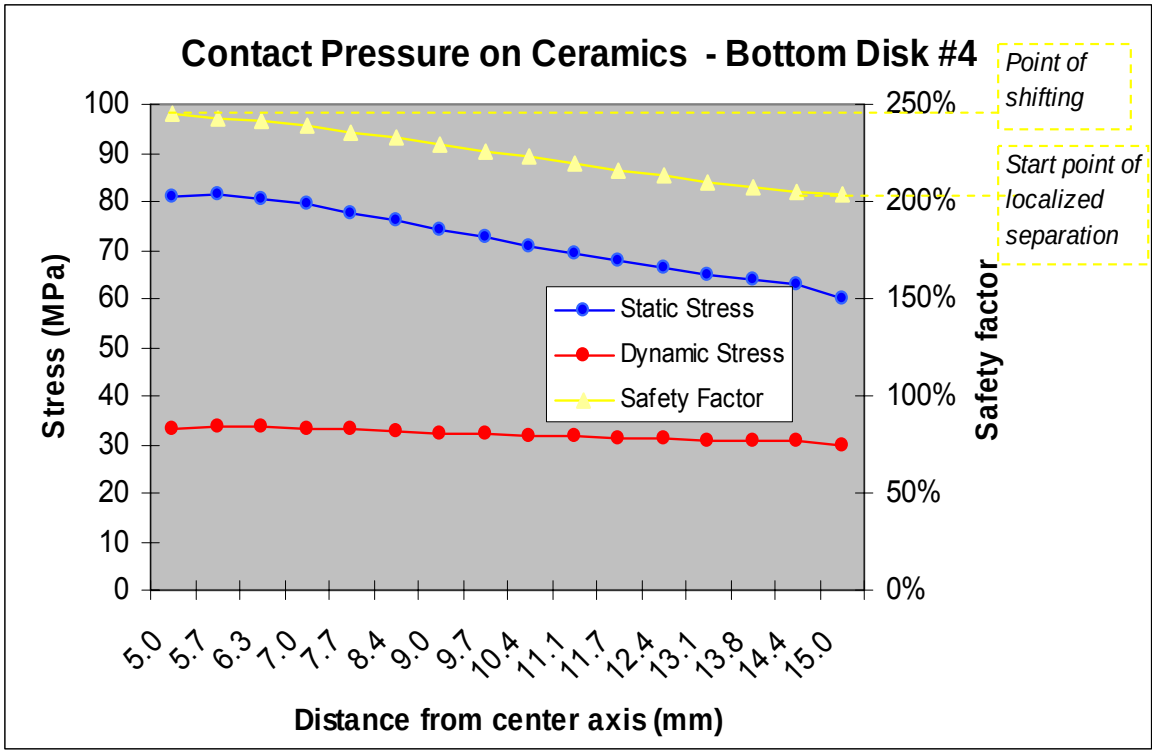

(h)

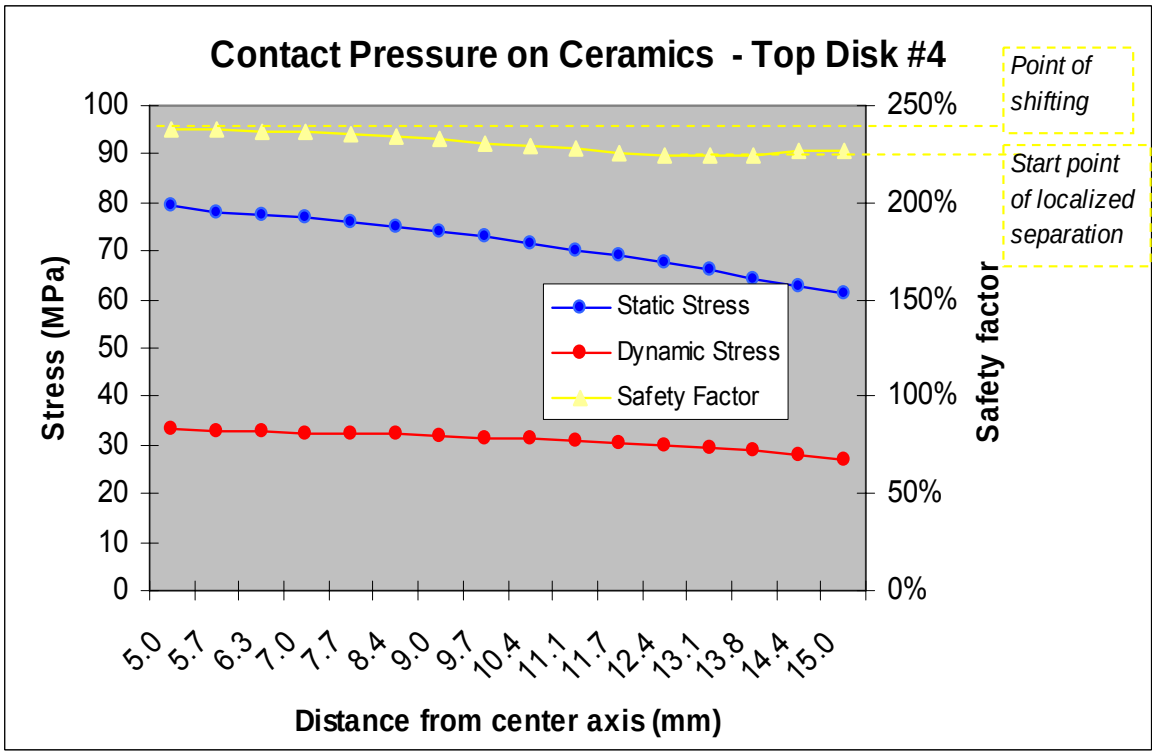

CHAPTER 4: Experiment, transducer failure due to excessive amplitude

4.1 Experimental set-up

In order to induce failure in the piezoelectric transducer under high amplitude conditions to study the failure mode, a vibrating stack consisting of a drive+slave transducer combination was used. This same set-up has been used in past experiments and is currently used as a way to perform endurance tests on ultrasonic generators under electronically loaded conditions. This is done because there is no practical way to mechanically load a vibrating stack with the same conditions encountered in production. In this drive+slave configuration the drive transducer is subject to electrical loads typically encountered during welding. With this arrangement, the slave transducer can be overstressed in a controlled manner based upon the booster size, generator setting and the manner in which the piezoelectric crystal is electrically connected. Figure 4.1 shows the basic set-up of this vibrating stack as well as several examples showing how to create normal and overstressed conditions within the slave transducer. The slave transducer is considered overstressed when the input amplitude at the coupling surface is greater than 7.5 microns, which is normally the maximum or nominal operating limit of the system. In figure 4.1d the generator is set to 75% resulting in a drive transducer output of 5.7 microns, which is 75% of 7.5 microns. The booster will amplify this value and double it based upon its gain ratio, generating 150% of the nominal stress level or ~11.3 microns in the slave transducer. Figure 4.2 shows a picture of the vibrating test stack. Figure 4.3 shows a schematic of the overall set-up of the experiment. Figure 4.4 shows pictures of the actual laboratory set-up used during the experiment.

The vibrating stack under study was mounted on a rigid booster tooling mount and then clamped to a rigid test stand to ensure no movement during testing and dampen any vibrations. Magnetic devices were used for easy positioning of the slave transducer cooling air lines and the infrared temperature sensor. The cooling air pressure was controlled by a simple pressure regulator. The temperature was measured with a USB connected infrared temperature sensor. This device displayed a real-time read-out of the temperature and it was pointed directly at the piezoelectric crystals as shown in figure 4.4e. The laser vibrometer laser module was positioned on a rigid tripod and aimed directly at the reflector plate of the slave transducer. It was positioned to be

perpendicular to this plane to ensure accurate readings in the axial direction. The laser module was connected to the laser vibrometer processing module, which was run with a Windows based user interface program. In order to have redundancy in the amplitude readings and to monitor the short vibrating pulses used in the experiment, an oscilloscope was connected to the laser vibrometer control module to monitor an analog output which was proportional to the velocity. The laser vibrometer software could also calculate the amplitude, however it required a stable signal lasting more than 2-3 seconds. Most testing was performed with much shorter cycle times, hence the need for an alternate method to capture the measurement data. The drive transducer on the vibrating stack was controlled with an ultrasonic generator, which was in turn connected to a PC running HUG's DIASIM software. This software can be used to run the generator in a pulsed operation mode and includes an easy to read graphical display with recording features. The slave transducer electrical leads were connected to an electronic load that functioned in the exact opposite way as the generator. It dissipated the electrical energy being created by the vibrations in the slave transducer. All testing was performed in a temperature controlled and sound isolated room.

4.2 Equipment

Table 4.1 lists the major pieces of equipment used to perform this experiment. The list includes the manufacturer, part number, serial number and any other data available.

4.3 Test Procedure

The goal of these tests was to establish the failure point and failure mechanism of the slave transducer due to excessive stress by increasing the amplitude above normal operating levels. This needed to be performed in a controlled and stepwise manner to ensure accurate and repeatable results. First, the PZT disk temperature reached during the tests should never exceed 35 degrees Celsius, ensures the temperature is not a variable and prevents inaccuracies due to property changes at higher temperatures. Second, the tests should simulate typical welding conditions as much as possible, including weld time, duty cycle and power draw. The first series of tests were performed for benchmarking purposes. These established a baseline for the amplitude readings under normal conditions at 100% nominal amplitude at the slave transducer. Once the baseline was established and all appropriate parameters recorded, the amplitude could

be slowly increased until failure occurred in the transducer. During each phase of testing, critical parameters were recorded for analysis. Some of the parameters recorded throughout the testing included temperature, generator amplitude settings, generator output power/frequency, reflector plate amplitude measurements, number of cycles, series/parallel impedance and frequency along with capacitance. Following is the general procedure used during each test:

1. Prior to beginning tests on a new slave transducer, perform an impedance and capacitance sweep between 28-32 kHz with the impedance analyzer. Note any deviations in the shape of the curve. Record values for the series/parallel frequency and series/parallel impedance. Perform a capacitance sweep between 1-2 kHz and record the value.
2. Verify all electrical connections, generator settings, DIASIM settings, temperature values and torque values.
3. Setup the laser vibrometer software by establishing the reference plane with three points, choosing the measuring point, and performing an autofocus scan.
4. Activate the ultrasonics at several known safe amplitude levels to verify the laser vibrometer readings, generator readings and audible sounds are correct. If possible, compare these values with previous results under the same conditions. If values do not match within a few percent, redo the laser vibrometer setup and try again.
5. Record starting parameters on the Excel test data sheet and then begin the test. Most tests involve running multiple 2 second cycles with 250 milliseconds of vibration and 1,750 seconds without vibration.
6. Observe the amplitude output, generator power and temperature for the first few cycles and record these values as the starting values in the Excel test data sheet. Note any unstable parameters.
7. If the test is only a few minutes long, monitor the output values every 30-60 seconds to make sure they are stable. At the end of the test, deactivate the ultrasonics and record the end results. If the test lasts several hours, record readings every 30-60 minutes as well as at the end of the test.
8. After the test is finished, allow the transducer to cool back to room temperature. Then either adjust the amplitude to the next higher interval (usually 10% higher) and proceed

to step #4 or remove the slave transducer and measure values with the impedance analyzer.

9. If the transducer fails at any point during the test, note the failure values, which include generator power draw, appearance of amplitude graph, amplitude values, temperature and any unusual noises. Records results from the impedance analyzer and then carefully disassemble, while taking detailed pictures and notes of the appearance.

Using these guidelines, two main types of tests were performed. Burst tests were conducted to quickly discover the ultimate failure point and endurance tests were performed to find the endurance limit. In the burst tests, the transducer was vibrated at the same amplitude for 100 cycles in a row then the amplitude was increased and the process repeated. In each cycle, the system was vibrating for 250 milliseconds and then turned off for 1,750 milliseconds. In the endurance tests, the same cycle time of 250/1,750 milliseconds was used, however up to 40,000 cycles could be reached while running at the same amplitude level. This allowed the vibrating cycles to reach as high as 10E8.

4.4 Results

Over the course of the testing, while monitoring all relevant parameters, seven transducers were operated to the point of failure. The raw test data can be found in appendix D. Two of the failures (transducer #1 and #2) were not under controlled conditions and are not included in some of the analysis. Transducer #4 appeared to fail, but upon inspection showed no physical signs of damage and still operated correctly at lower amplitude levels. A baseline amplitude value was established by using the laser vibrometer to measure the reflector plate of the drive and slave transducer. The generator was set to 100% using a 1:1 amplitude coupler. This established the reflector plate displacement or amplitude at 100% of the nominal operating amplitude level. Because this value varied slightly depending on the load conditions, an average value was used, which can be found in table 4.2. All amplitude readings were then based off this average value where an oscilloscope value of 1.72 volts = 100% of the stress level. Figure 4.5 shows a typical oscilloscope reading under normal operating conditions. The voltage value is based upon the peak to peak reading, which is 2.78 in this figure.

Figure 4.6 plots the number of vibrating cycles and corresponding amount of amplitude for each slave transducer tested while highlighting the failures. The failure values ranged from 179% to 244% of the nominal stress level. Transducer #4 did not fail. It was making an unusual noise that was misinterpreted as failure. Upon disassembly, it was shown to be in perfectly good condition. Table 4.3 lists the impedance plot values before and after failure for each transducer. There was virtually no change in the shape of the impedance curve even after complete failure and only a small decrease in the series and parallel frequencies from -20 to -290 Hz. Leading up to the point of failure, all values remained constant, even after 10E8 cycles. A typical impedance plot is shown in figure 4.7.

Table 4.4 summarizes the mode and amplitude level at failure for each transducer. Figure 4.8 shows pictures from each transducer failure.

All of the failure modes appeared to be from electrical arcing at the inner diameter of the lower ceramics (disk #3 and #4). This caused damage to the piezoelectric crystals due to localized overheating, transgranular cracking, and possible depolarization. Above a certain amplitude threshold (approximately 170% of the nominal amplitude), an alternate frequency was excited. This caused a noticeable change in the sound, an increase in amplitude and an erratic amplitude read-out on the oscilloscope and DIASIM software. The graphs in figure 4.8d show the amplitude before and after entering this zone. This alternate frequency did not cause failure and the system appeared to run indefinitely at these levels (see test 176). Figure 4.9 shows DIASIM graphs before and after operating above this threshold value. In all cases, ultimate failure caused a significant change in the system behavior. There was an immediate change in the audible sound. In addition, the generator power, transducer temperature and amplitude increased significantly, while the frequency decreased. If further testing was performed, the frequency would continue to decrease until it reached the internally programmed generator limit of 19,500 Hz. The amount of physical damage was directly proportional to how many times the salve transducer was vibrated after the point of failure. This can be seen by comparing transducer #6 to transducer #5. Both failed close to the same point, but transducer #5 was vibrated for significantly more cycles than #6 after the point of failure.

4.5 Tables and figures

Table 4.1 – Testing equipment specifications

Equipment name:	Manufacturer:	Part Number:	Serial Number:	Description and features
Laser Vibrometer - Sensor head	Polytec	PSV-I-400	605 2123	Laser Doppler Vibrometer - Non-contact vibration measurement, uses the Doppler principle to measure the frequency shift in the back-scattered laser light reflected by a vibrating surface. Determines instantaneous velocity and integrates for velocity, differentiates for displacement. Uses 633nm wavelength laser.
Laser Vibrometer - Vibrometer Controller	Polytec	OFV-5000	505 2271	Low pass filters with 1.5MHz bandwidth and 10 m/s
Laser Vibrometer - Junction Box	Polytec	PSV-E-400KU	505 1776 0004	Interface between sensor head, vibrometer controller and data management system. Includes output for signal generator
Laser Vibrometer - Data Management System	Polytec	PSV-W-400	n/a	Industrial PC with 17" Display, network connections and data acquisition features. Signal generator, uses Windows operating system
Oscilloscope	Gould	Classic 6000	94900004	Analog oscilloscope for measuring voltage, frequency, amperage
Electronic load	H&H	n/a	n/a	Adjustable digital load, up to 500VDC
Precision Impedance analyzer	Agilent	4294A	MY43200983	Impedance analyzer, capable of plotting impedance, phase angle and capacitance
Ultrasonic Generator	Herrmann Ultraschalltechnic	1700CV	74011/05	Digital ultrasonic generator operating at 30kHz. Controls amplitude output via current and frequency modulation

Table 4.2 – Baseline amplitude readings at 100% nominal amplitude

Trial#:	Amplitude at reflector plate (volts):	Transducer measured:	Load configuration:	Generator power (w):	Frequency (Hz):
3	1.83	Drive	Open wires	44	30,662
4	1.95	Drive	Closed wires	82	29,935
13	1.60	Slave	Open wires	43	30,660
14	1.57	Slave	Electronic load	680	30,636
23	1.55	Slave	Electronic load	739	31,048
138	1.72	Drive	n/a	42	31,299
145	1.80	Drive	Std sonotrode	171	30,428
Average:	*1.72*				

Table 4.3 – Impedance plot values before and after failure

Transducer #:	Pre/post Failure:	Series Frequency (Hz):	Parallel Frequency (Hz):	Series Impedance (ohms):	Parallel Impedance (kohms):	Capacitance (pF):
2	Pre	29,160	31,250	4.11	87.10	9.21
2	Post	28,870	31,010	4.83	70.83	9.52
2	Δ	-290	-240	0.72	-16.27	0.31
3	Pre	29,380	31,460	2.66	159.40	9.42
3	Post	29,340	31,440	3.75	111.79	9.64
3	Δ	-40	-20	1.09	-47.61	0.22
4	Pre	29,350	31,450	2.40	155.20	9.42
5	Pre	29,840	31,870	14.90	26.08	8.99
5	Post	29,660	31,590	11.09	26.41	9.66
5	Δ	-180	-280	-3.81	0.33	0.67
6	Pre	29,840	31,880	9.34	40.55	9.25
6	Post	29,820	31,830	5.19	61.10	9.26
6	Δ	-20	-50	-4.15	20.55	0.01
7	Pre	29,830	31,830	16.07	24.22	9.02
7	Post	29,540	31,570	15.11	22.40	9.10
7	Δ	-290	-260	-0.96	-1.82	0.08

Table 4.4 – Summary of failure modes

Transducer #:	Highest stable amplitude:	Amplitude at failure:	Failure Mode:			Notes:
			Shifting crystals:	Cracking crystals:	Electrical arcing:	
1	118%	220%	N	Y	Y	Failure appears to be from improper electronic load adjustment, drawing too much power causing rapid overheating (100+ Celsius) and high amplitude output - discoloration on outside of transducer, electrical arcing at inner diameter
2	147%	154%	N	Y	Y	Failure is similar to transducer above, not as much overheating however it still reached high temperatures (60+ Celsius), internal arcing at inner diameter of crystals
3	185%	193%	N	N	Y	No external indication of failure, internal arcing into pre-stress stud, caused crystals to disintegrate at inner diameter
4	172%	n/a	N	N	N	No failure, sound of vibration changed at 172% amplitude, mistakenly assumed to be broken
5	220%	223%	N	N	Y	Arcing at inner diameter causing disintegration of crystals, melting at electrode at beryllium plate
6	213%	244%	N	N	Y	Test was stopped immediately at the point of failure; damage is not as severe as other transducers because of this. Initiation point of arcing is easy to see, at inside diameter of crystal #4 into titanium body and slight arcing at the inside of crystal #3
7	169%	172%	N	N	Y	Arcing at inner diameter causing heavy damage to crystals, did not melt electrode and beryllium plate

Figure 4.1 – Drive and slave transducer set-up – (a) configuration of vibrating stack for testing, (b) configuration creating nominal stress values in slave transducer, (c) alternate configuration to create nominal stress values in slave transducer, (d) configuration creating 150% overstress in slave transducer

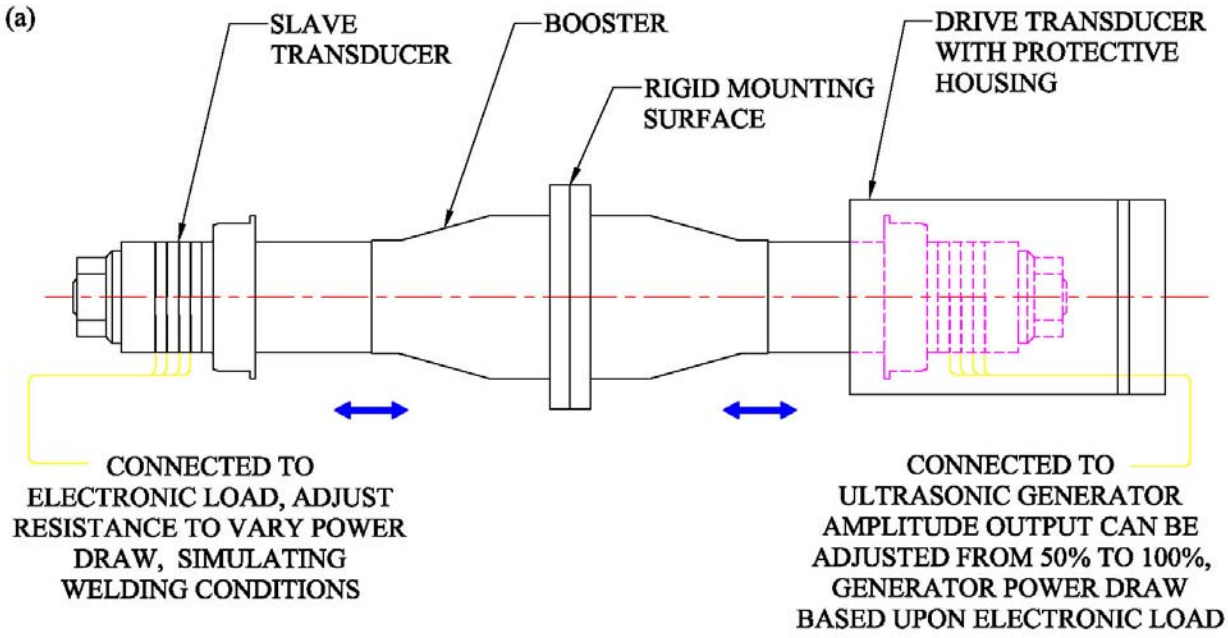

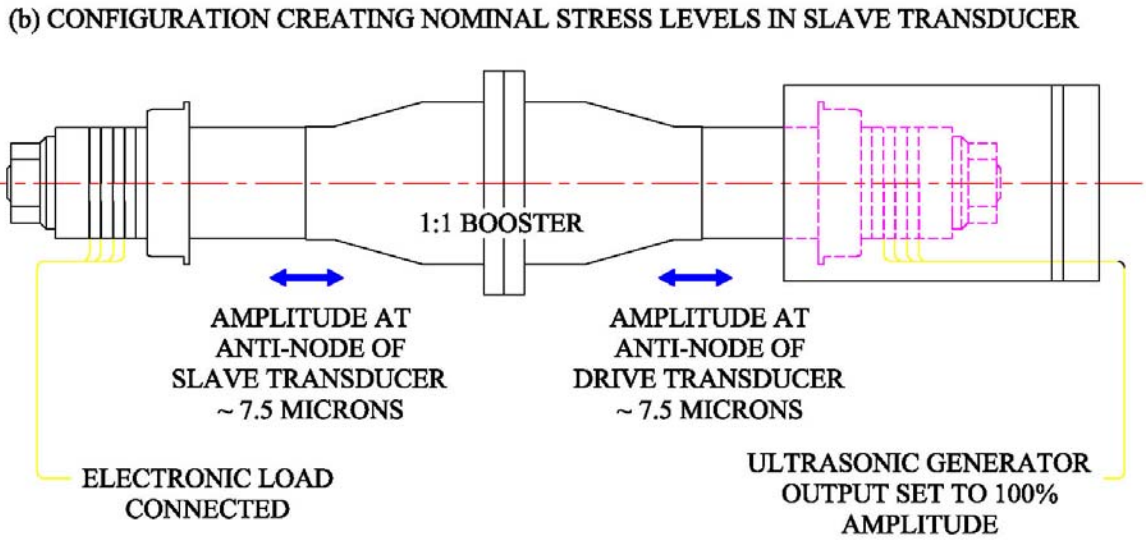

Figure 4.1 (cont'd)

(c) ALTERNATE CONFIGURATION CREATING NOMINAL STRESS LEVELS IN SLAVE TRANSDUCER

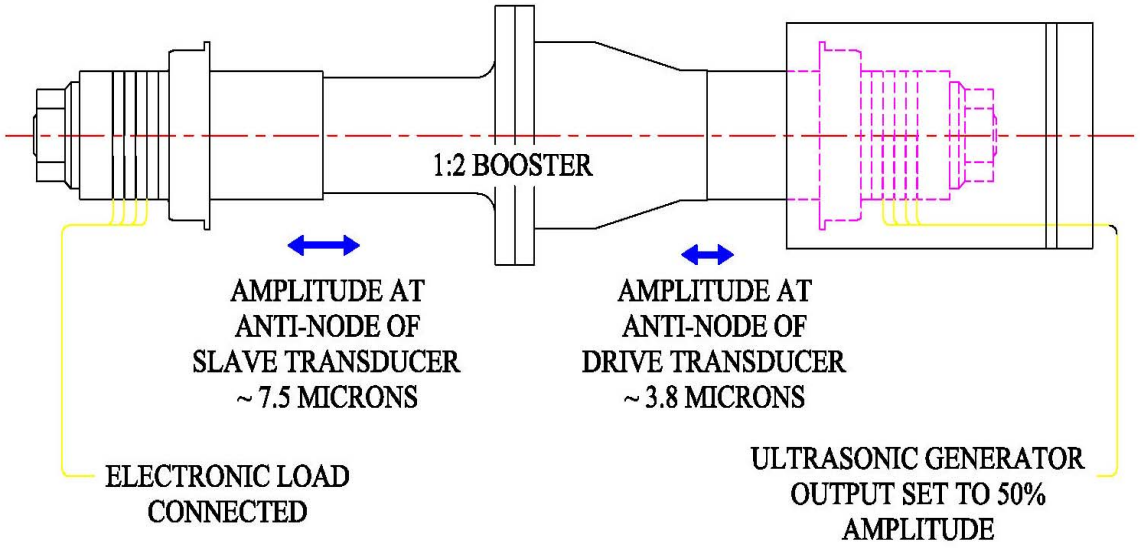

(d) CONFIGURATION CREATING 150% NOMINAL STRESS LEVELS IN SLAVE TRANSDUCER

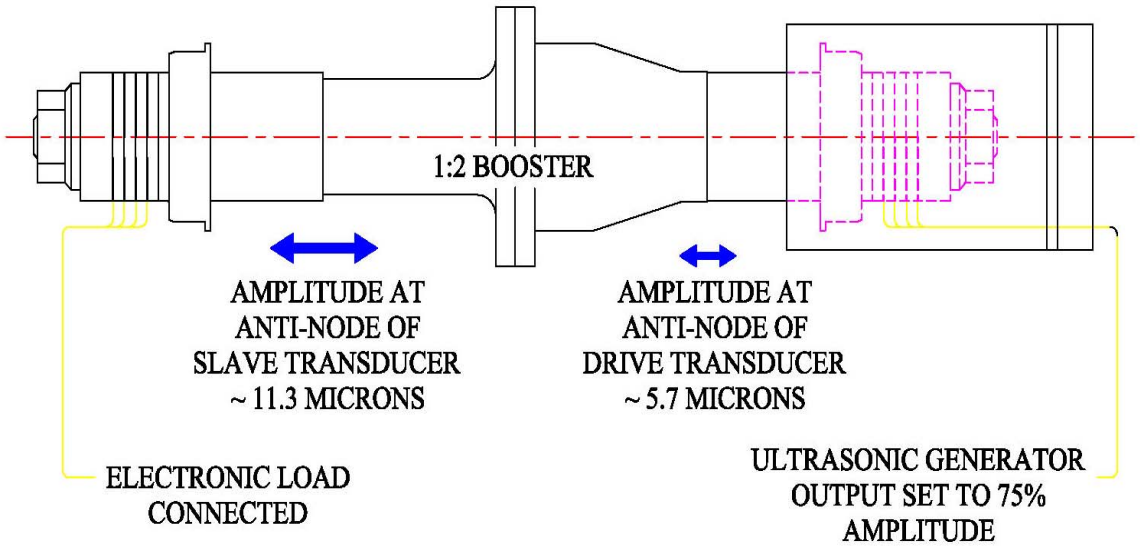

Figure 4.2 – Picture of vibrating test stack

Figure 4.3 – Schematic of overall equipment set-up

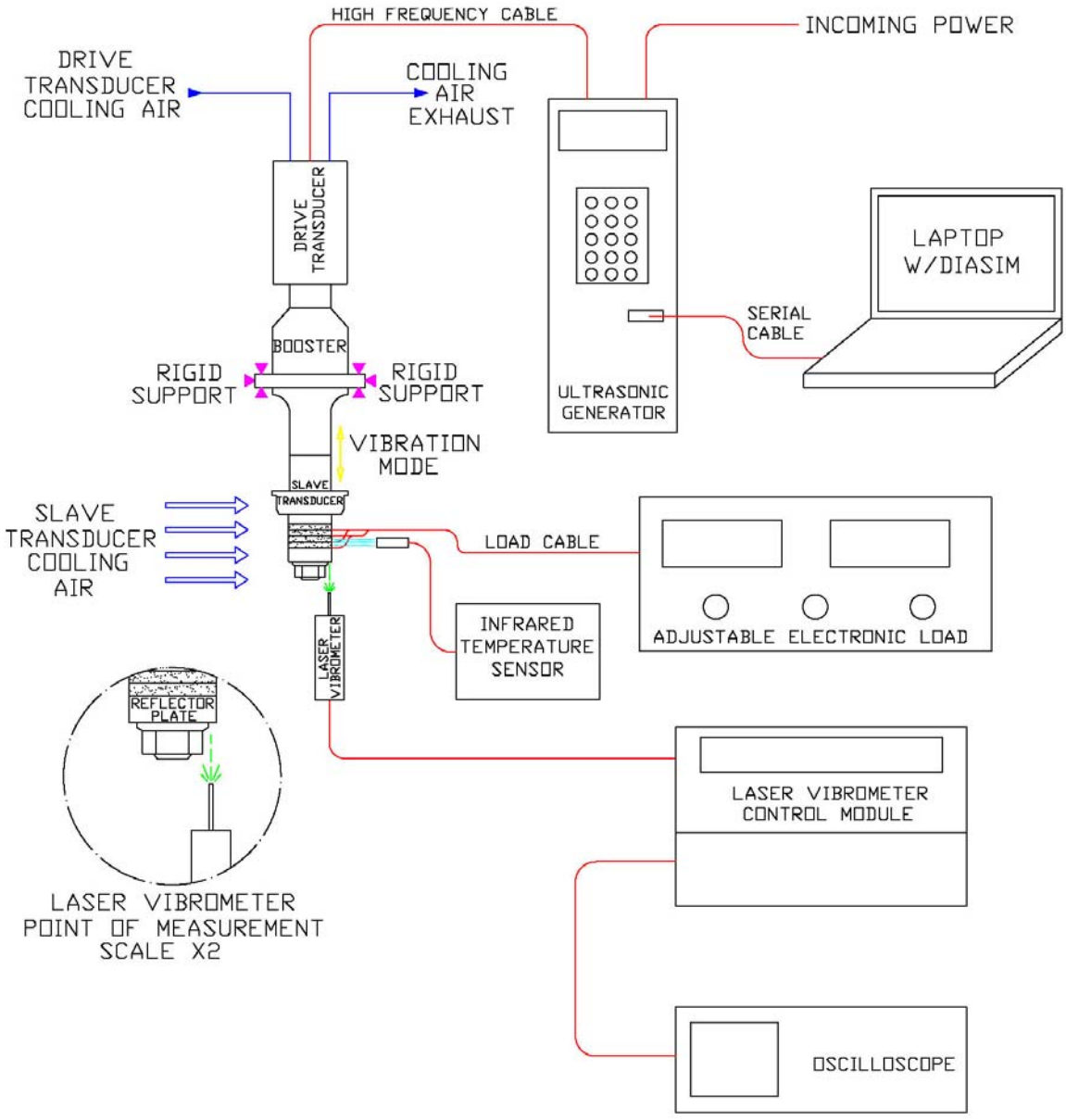

Figure 4.4 – Pictures of experimental set-up – (a) Laser vibrometer, electronic load, vibrating stack, (b) Temperature sensor, generator, computer with DIASIM, laser vibrometer control cabinet, oscilloscope, (c) Rigid booster mount, slave transducer, booster, drive transducer, (d) Close-up of vibrating test stack, (e) Cooling lines, electronic load connections, temperature probe, measuring point for laser vibrometer

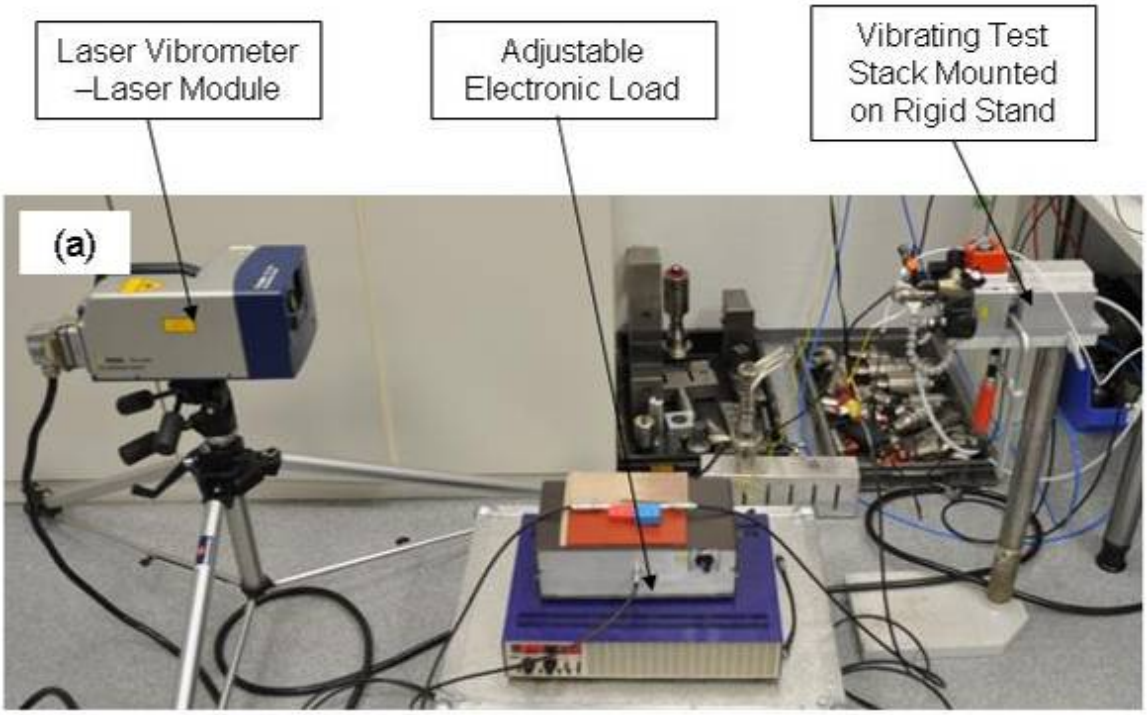

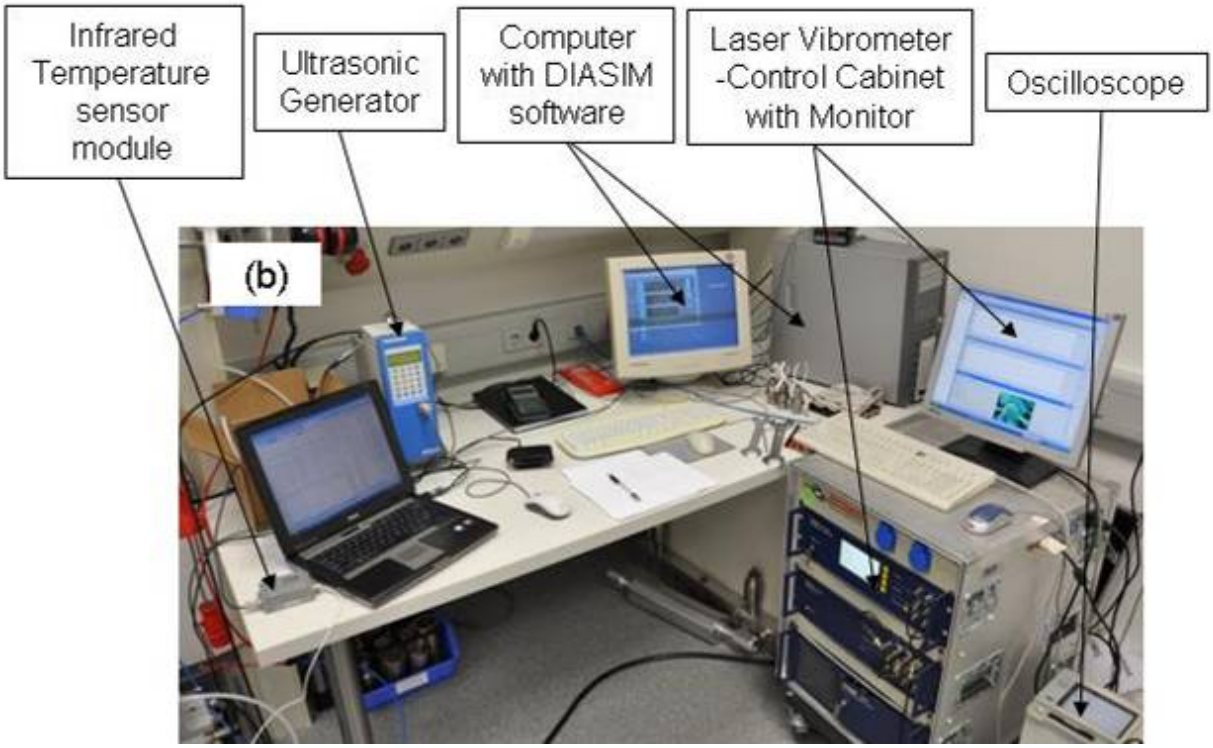

Figure 4.4 (cont'd)

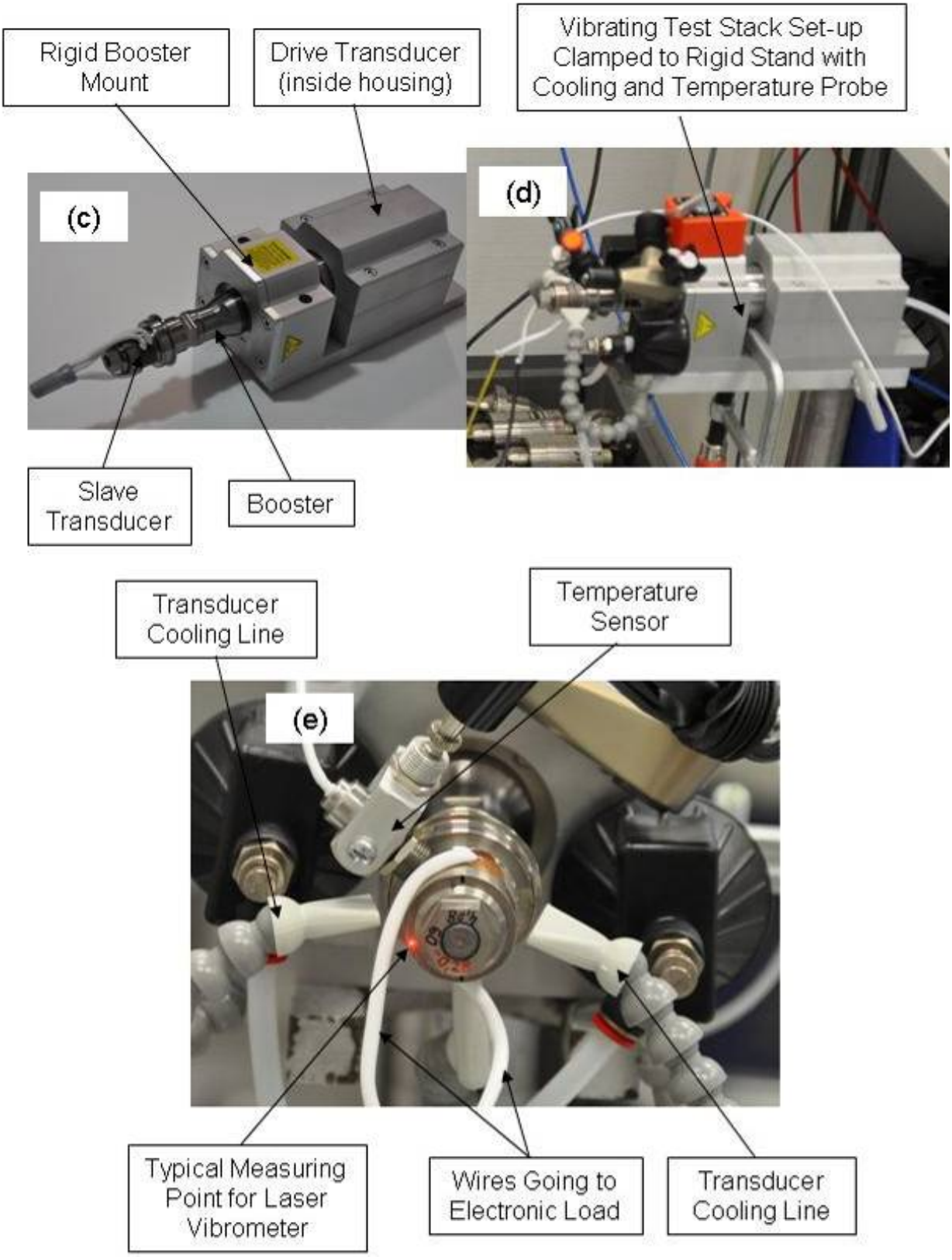

Figure 4.5 – Typical oscilloscope reading showing amplitude at reflector plate

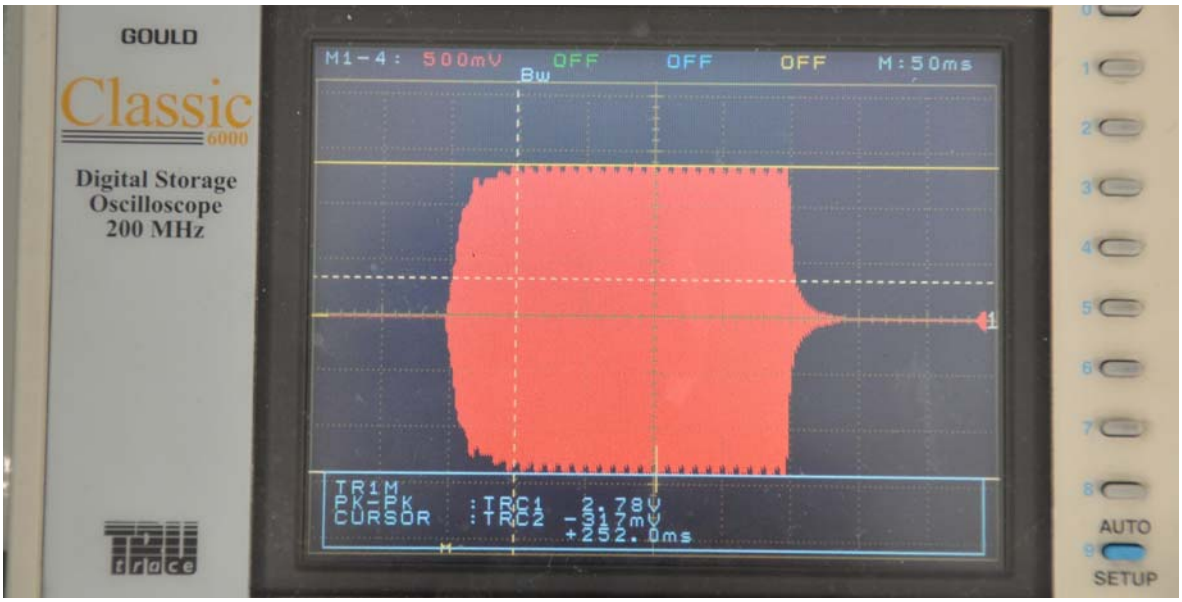

Figure 4.6 – Cycles to failure including amplitude or stress level

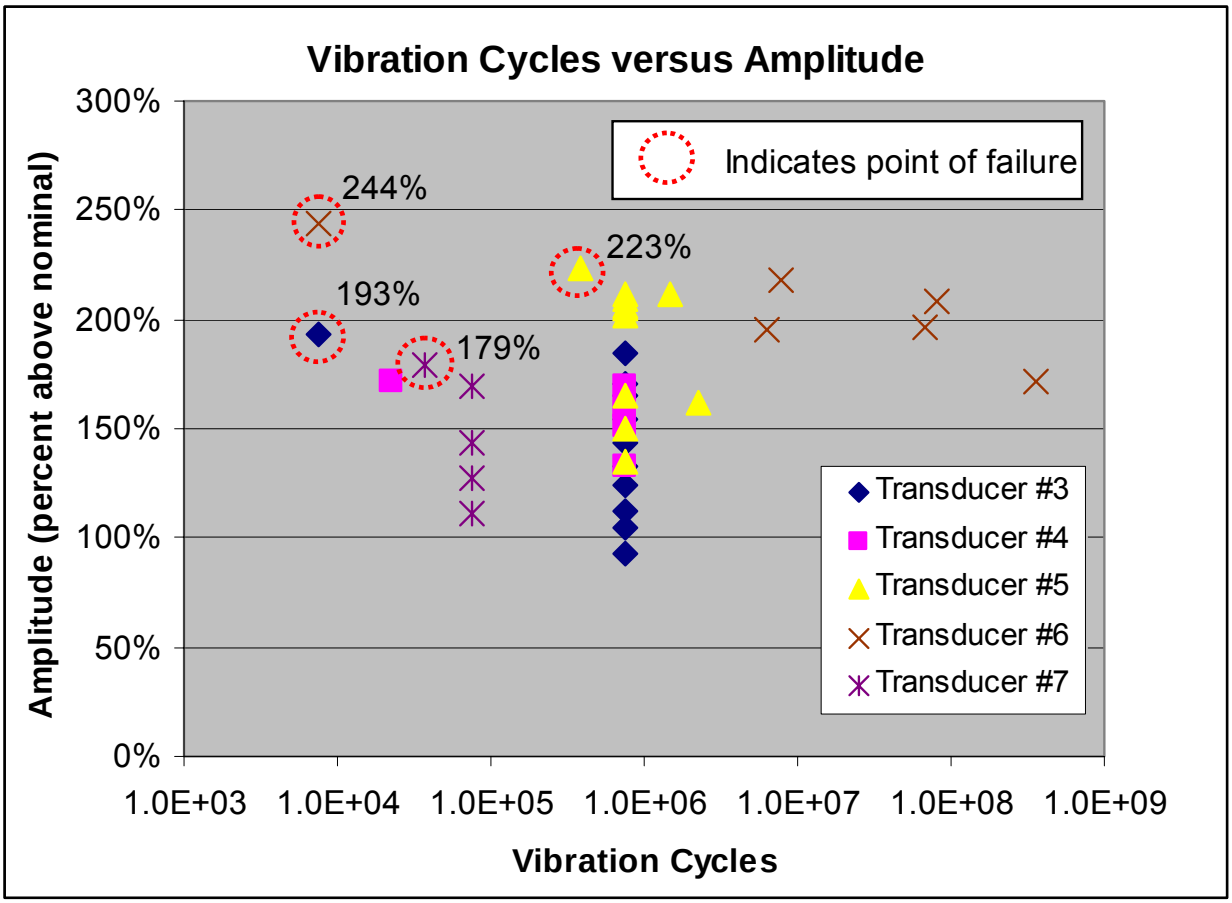

Figure 4.7 – Typical impedance plot

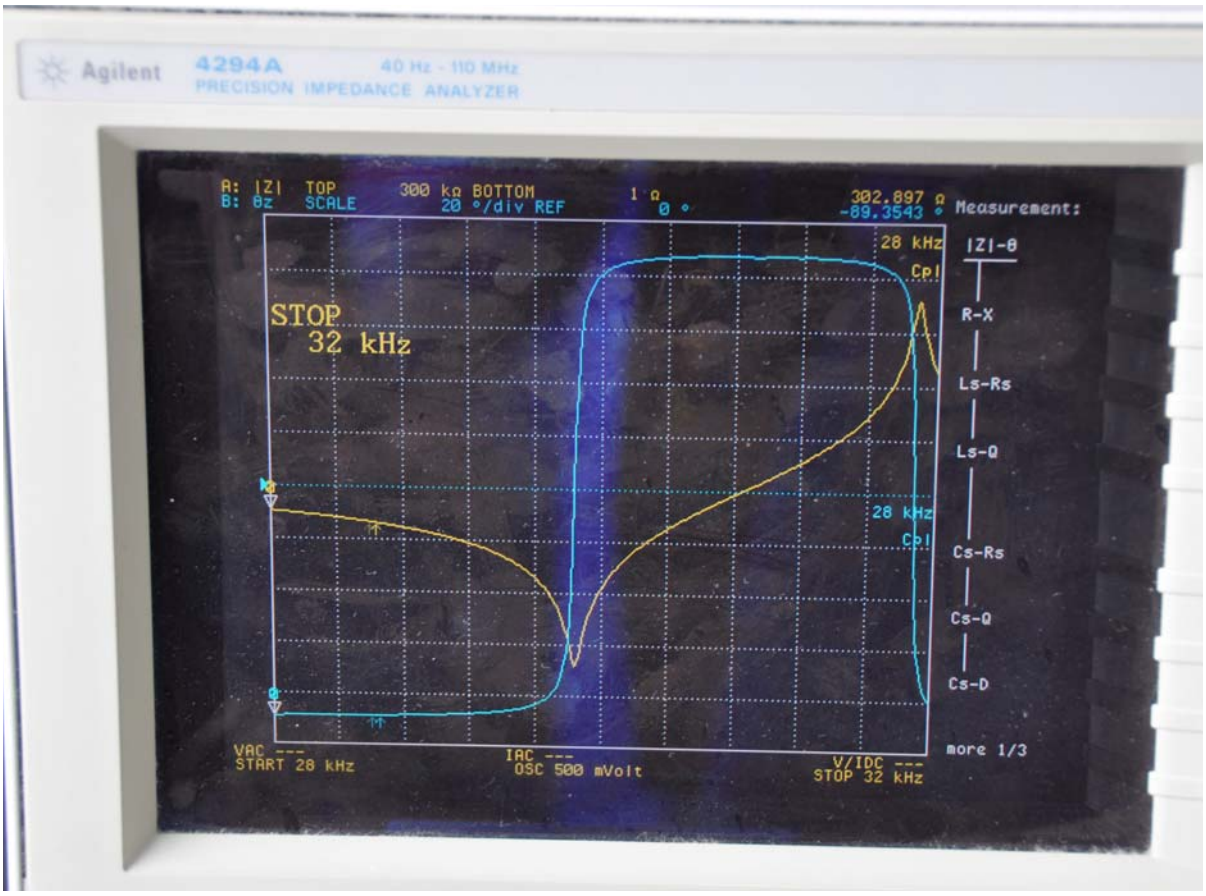

Figure 4.8 – Pictures of converter failures – (a) Transducer #1, (b) Transducer #2, (c) Transducer #5, (d) Transducer #6, (e) Transducer #7

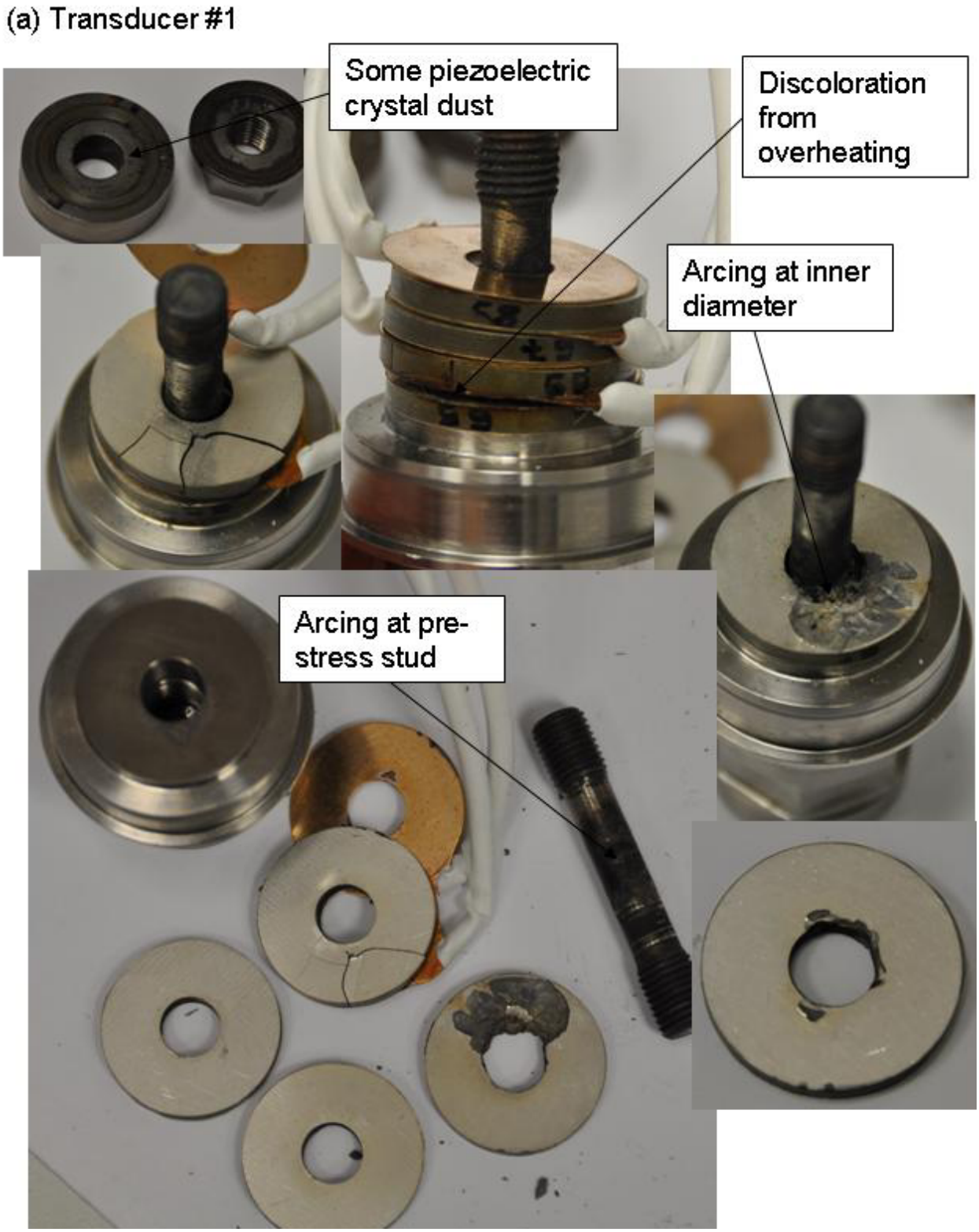

Figure 4.8 (cont'd)

(b) Transducer #2

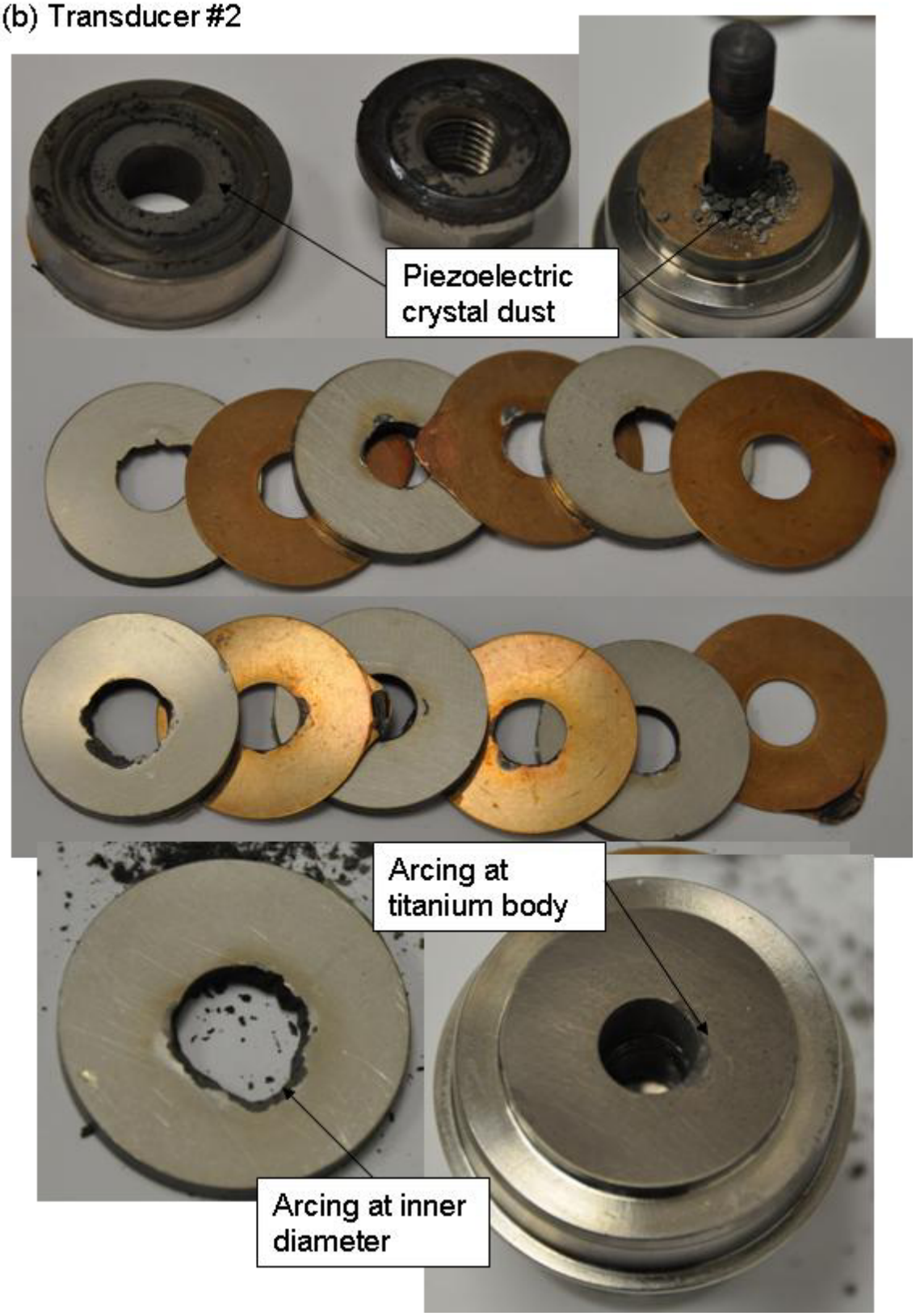

Figure 4.8 (cont'd)

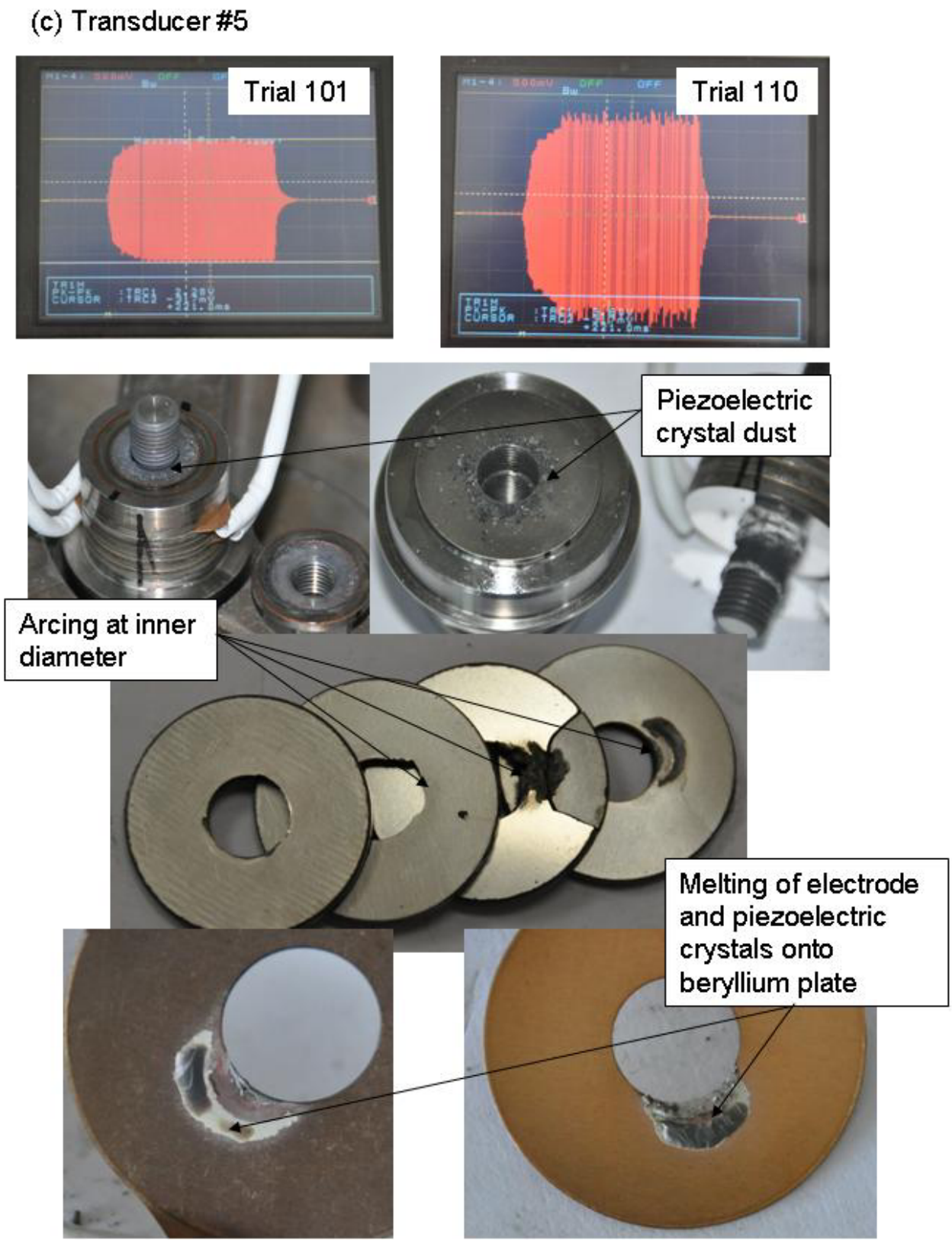

Figure 4.8 (cont'd)

Figure 4.8 (cont'd)

(d) Transducer #6 (cont'd)

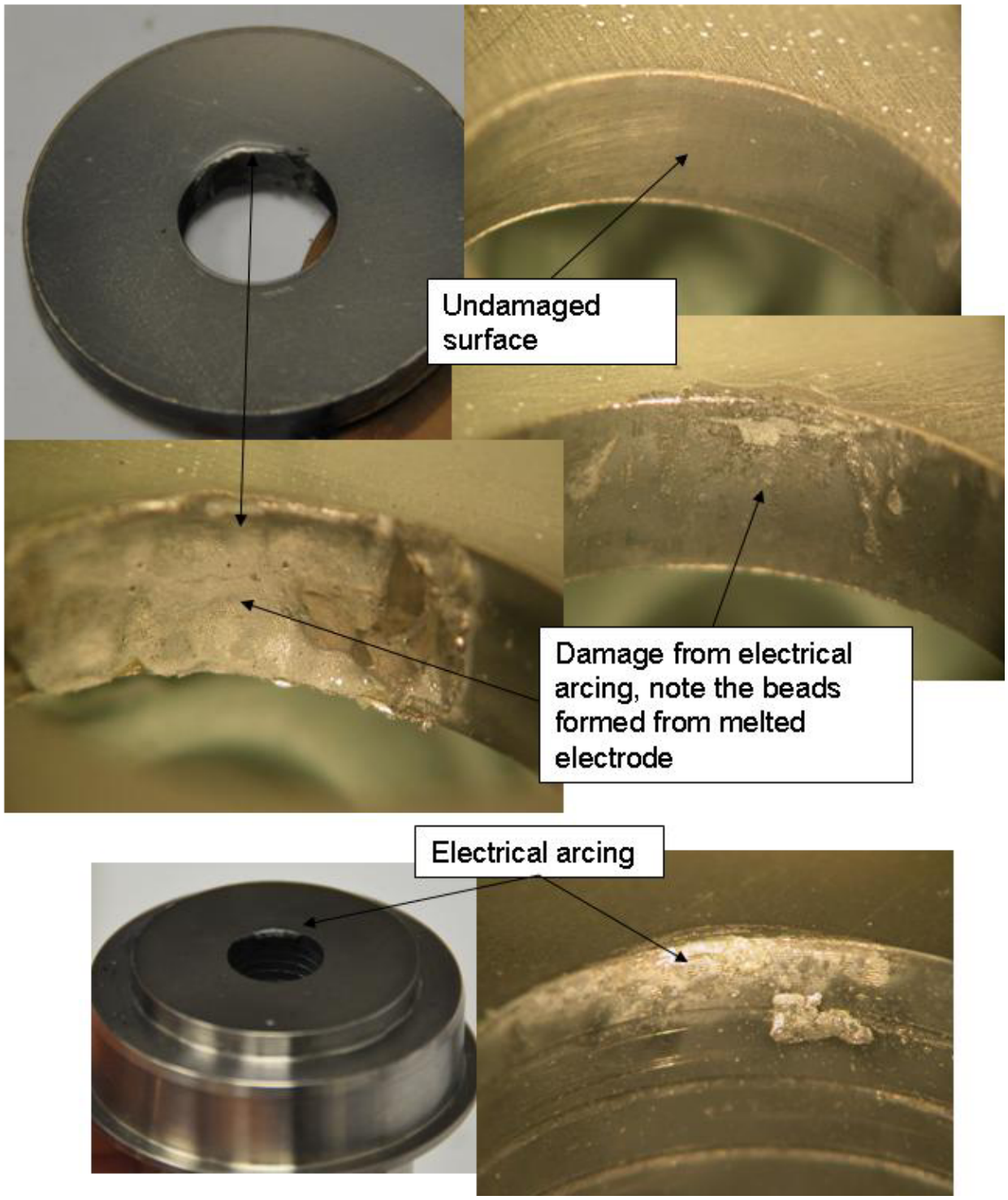

Figure 4.8 (cont'd)

(e) Transducer #7

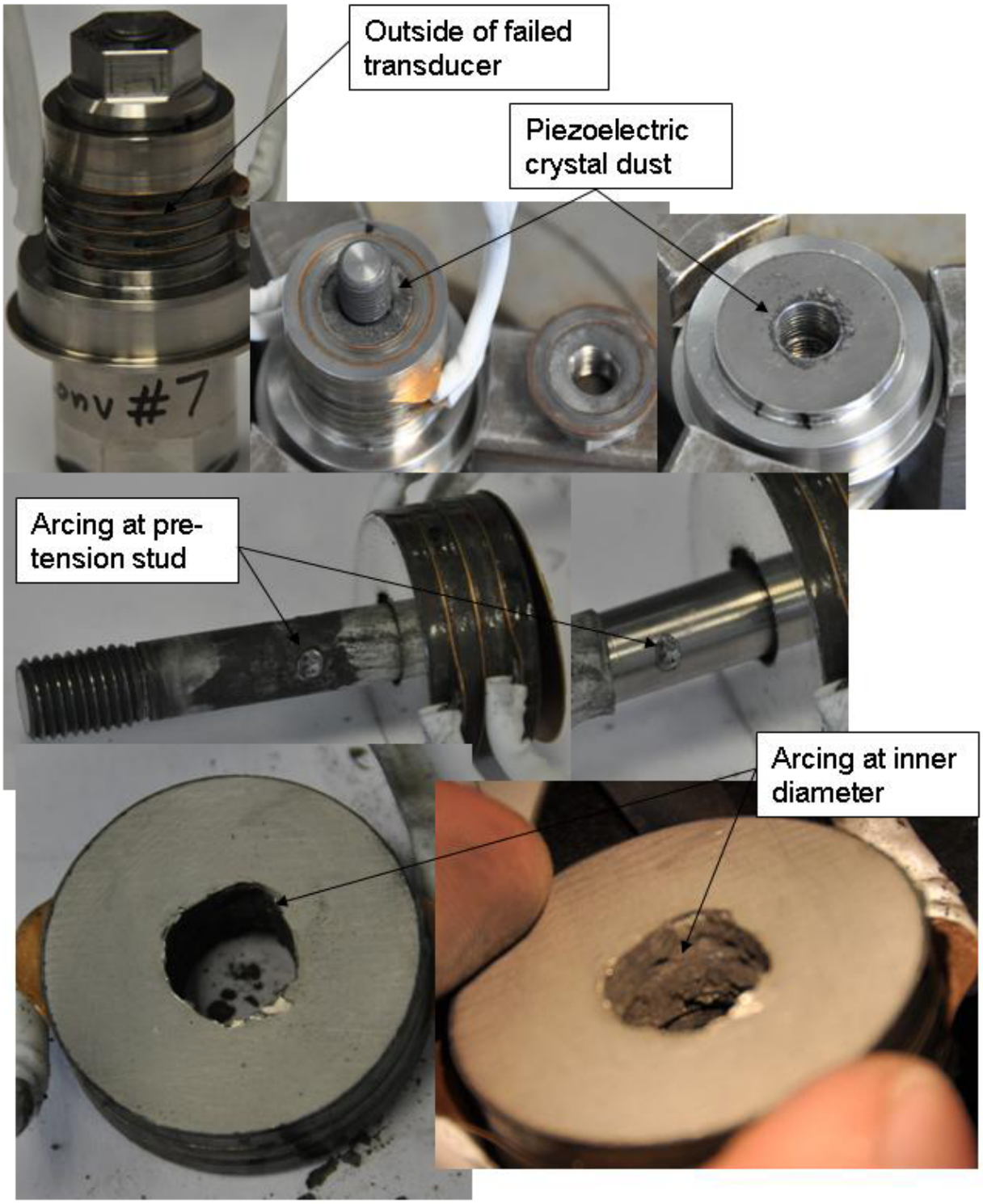

Figure 4.9 – DIASIM graphs before and after entering destabilized zone

CHAPTER 5: Conclusions

5.1 Summary of key points in FEA analysis and experiment results

The FEA analysis predicted loss of pre-stress at the outside edge of the top surface of crystal #4, starting at 208% of nominal amplitude levels (see figure3.19h). At close to 250% of nominal amplitude, there should be no pre-stress over the entire contact surface, which would allow the crystals to shift laterally. This same shifting value applies to the top and bottom surfaces on disk #3 as well as the bottom of disk #4. Examining the combined Von mises stress inside the crystals for both static and dynamic loads reveals a maximum of 114 MPa compressive stress, which is not enough to cause cracking based upon the compressive yield limit of 517 given by the manufacturer (see figure 3.3). The FEA analysis predicted the reflector plate amplitude should be approximately 5 microns zero to peak when the generator is set to 100% amplitude.

The experimental results showed significant statistical variation for the failure point of the transducers. Transducers failed between 179% and 244% of nominal stress levels, as shown in figure 4.6. All of the failures were clearly defined by a sharp drop in frequency and an increase in power. Additionally, electrical arcing and disintegration of the piezoelectric crystals on the inside diameter of the crystals occurred at disk #3 and disk #4. One key question is whether the arcing caused the disintegration of the piezoelectric crystals or if the crystals disintegrated and allowed an easy path for high voltage arcing. The failure of transducer #6 seems to show the arcing as the primary cause of failure under these conditions because the testing for this unit was stopped immediately after the first failure cycle. In this case, the only significant damage was at the inner diameter of disk #4 and the appearance is that of melting, not cracking. This would lead to the conclusion that the arcing is the root cause. None of the root causes of failures were due to cracking or shifting crystals.

5.2 Compare results between FEA and experiment

The results from the FEA analysis, the experiment and transducer failures under production conditions show no clear similarities. The experiment did not reveal any cracked crystals that were not the result of arcing or severe overheating and there was no crystal shifting even though these are the two dominant modes seen in production environments. The failures during testing

did not occur in the areas predicted by the FEA analysis either. The fact that the failures were consistent across all transducers and the fact that most production failures do not involve internal arcing (see figure 5.1 for examples of the inside of transducer failures for 30 kHz transducers under production conditions) leads to the inevitable conclusion that the testing method did not simulate production conditions. This discrepancy is most likely due to the fact that the testing load is purely electrical where the production load is purely mechanical. The production loads create a mechanical reactionary force from the thermoplastic material being welded and the rigid anvil. The magnitude of this reactionary force is based upon the applied welding force and the frequency is based upon the geometry, material properties, loading conditions and rigidity. This could lead to superposition of waves inside the transducer, creating areas of interference and reinforcement. Based upon current results, the conclusion is that the superposition of waves is causing localized stress concentrations leading to cracking and shifting.

The impedance plots matched between the FEA analysis and the experimental results. Across all 7 transducers, the average series and parallel frequencies was 29,648Hz and 31,698Hz, respectively. The model predicted values of 29,787 Hz and 31,937 Hz. The impedance values were not as close, however. These values are compared in table 5.1.

Another discrepancy was the amplitude of the reflector plate according to the FEA analysis and the testing. The laser vibrometer measured values between 4.0 to 5.1 microns with an average of 4.4 microns under 100% nominal stress levels. This was confirmed across all slave and drive transducers under various load conditions. The FEA model predicted 5.1 microns at 30,700Hz.

Even though the FEA results did not match the experimental results, it must be noted that this FEA analysis did not take electrical arcing into consideration. It only calculated the mechanical stress and strain based upon an electrical input. The arcing however did occur in the area with highest overall stress according to the FEA model (inner diameter of disk #3 and #4). This is confirmed by figure 3.12 and 3.14. Because piezoelectric materials behave according to coupled equations, there should have been a higher voltage or electrical field generated at these points, even if only for a very small amount of time until the voltage levels equalize across the surface of the conducting plates. This could have caused arcing to initiate at this point. A simple test

can be performed by considering the voltage needed to cause arcing across the conductive surfaces inside the transducer. First, assume the peak voltage at 100% nominal stress levels is 850 volts (this is the voltage applied to the FEA model and the voltage supplied by the generator at 100%), and there is a one to one linear relationship between them. This means increasing the stress or amplitude from 100% to 200% increases the peak voltage in the transducer from 850 to 1700 volts. Second, consider the voltage needed to initiate arcing, which is based upon the conductive properties of air, the configuration of the electrical conductors, surface properties and the distance between the conducting surfaces. A rule of thumb when designing ultrasonic transducers states that arcing will occur between 11-13 kilovolts/inch or 433-512 volts/mm [15]. The shortest path to ground (easiest arcing path) inside the transducer is based upon the thickness of the ceramic disks, which is 3mm. Therefore, the highest voltage level the current design can tolerate before arcing is approximately, 1300-1500 volts. Using the previous assumptions, the stress level would need to reach 216-250% of nominal levels to cause shorting. Given that the four controlled failures occurred at 244%, 223%, 193% and 179%, two of the four failures fall directly within this range. The case becomes stronger when considering that transducers #5, #6 and #7 were better insulated than transducer #3.

5.3 Inaccuracies in FEA analysis and experiment causing deviations in results

There are a variety of inaccuracies contributing to possible deviations in the FEA results and the experimental results:

- Material properties used in the FEA analysis
- Voltage boundary conditions in the FEA analysis compared to actual values in reality or in production conditions
- Laser vibrometer accuracy
- Alignment between slave transducer reflector plate and laser
- Relaxation in the pre-stress value after reaching the 44 kN preload level leading to lower actual pre-stress values
- Normal transducers are hard mounted with a housing clamped onto the nodal mounting surface, it is not able to freely vibrate

5.4 Recommendations for additional testing

Because few of the results between the FEA analyses matched the experimental values, additional testing and modifications to the model need to be performed. Below is a list of recommended next steps:

1. Test a transducer with lower pre-tension to eliminate the arcing due to high stress levels and determine if crystals crack due to loss of pre-stress or shifting based upon the FEA model.
2. Repeat the test while monitoring actual voltage and current at the slave converter electrical leads using a power monitor to determine if critical arcing voltages are reached.
3. Measure the reflector plate of the drive converter under production welding conditions, i.e. with a sonotrode in place of the slave converter and an anvil with thermoplastic material in between. Increase welding pressure until amplitude levels are high enough to cause failure.
4. Perform a Fourier analysis on a transducer in production to examine the additional frequencies created from the anvil reaction during welding.
5. Perform an FEA analysis with a damped load to simulate true welding conditions and compare to experimental results.

5.5 Tables and figures

Table 5.1 – Comparison of impedance between FEA and experimental results

	Series Frequency (Hz):	Parallel Frequency (Hz):	Series Impedance (ohms):	Parallel Impedance (kohms):
FEA calculations	29,787	31,937	28.90	12.07
Experimental results (averaged):	29,648	31,698	9.07	81.09
Δ	139	239	19.83	-69.02
Percent difference:	0.47%	0.75%	218.49%	-85.12%

Figure 5.1 – Pictures of typical production transducer failures

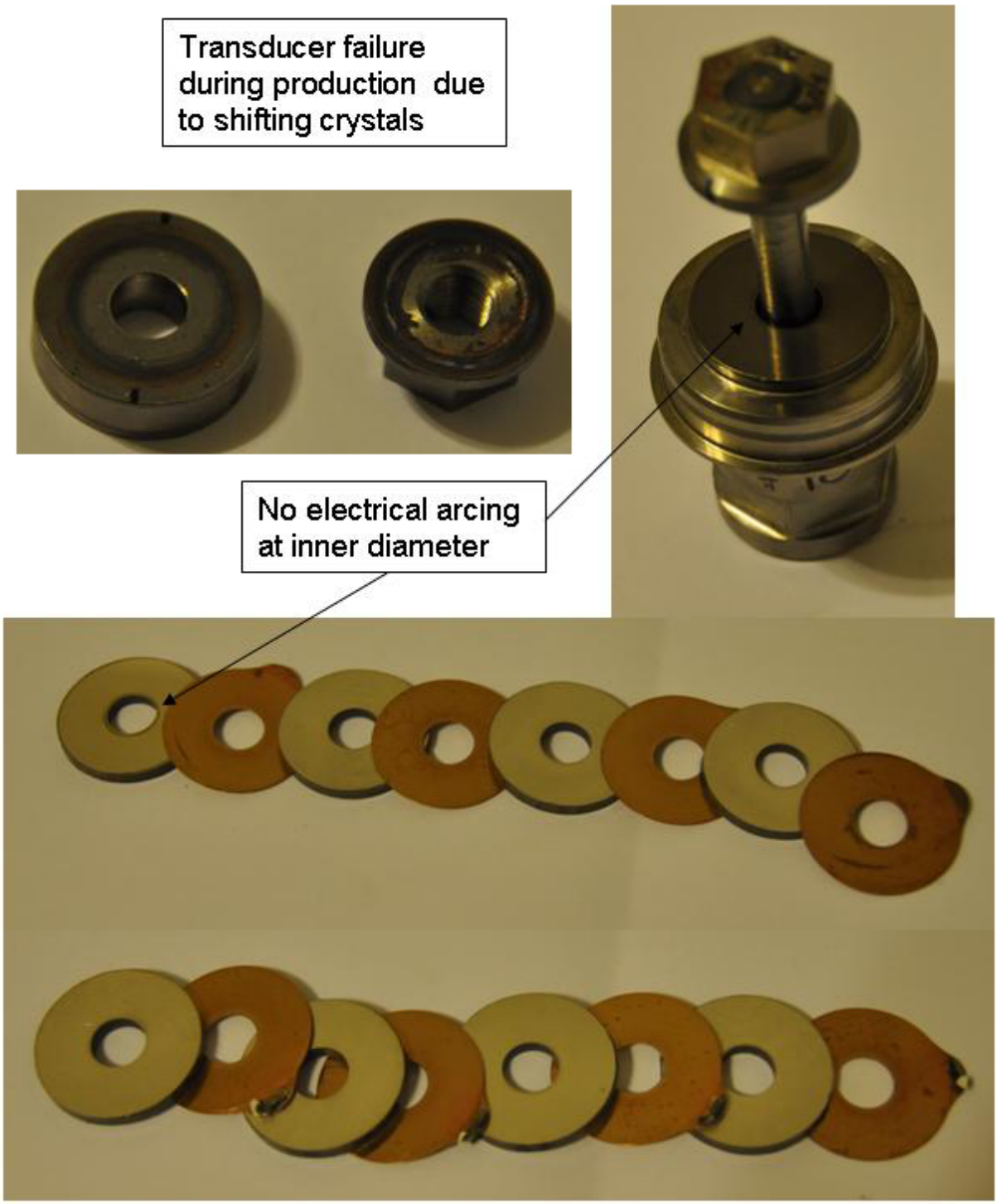

Figure 5.1 (cont'd)

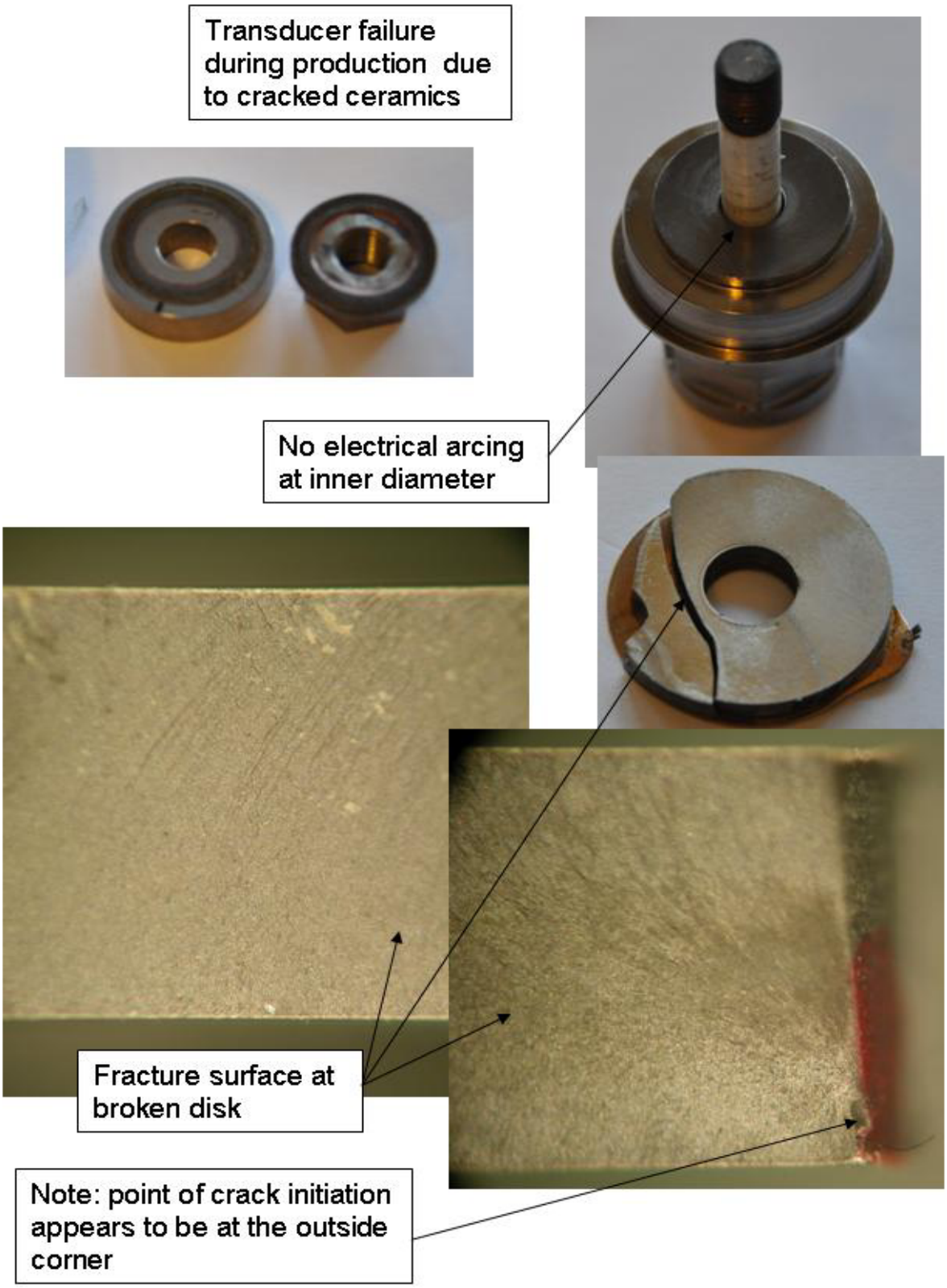

Figure 5.1 (cont'd)

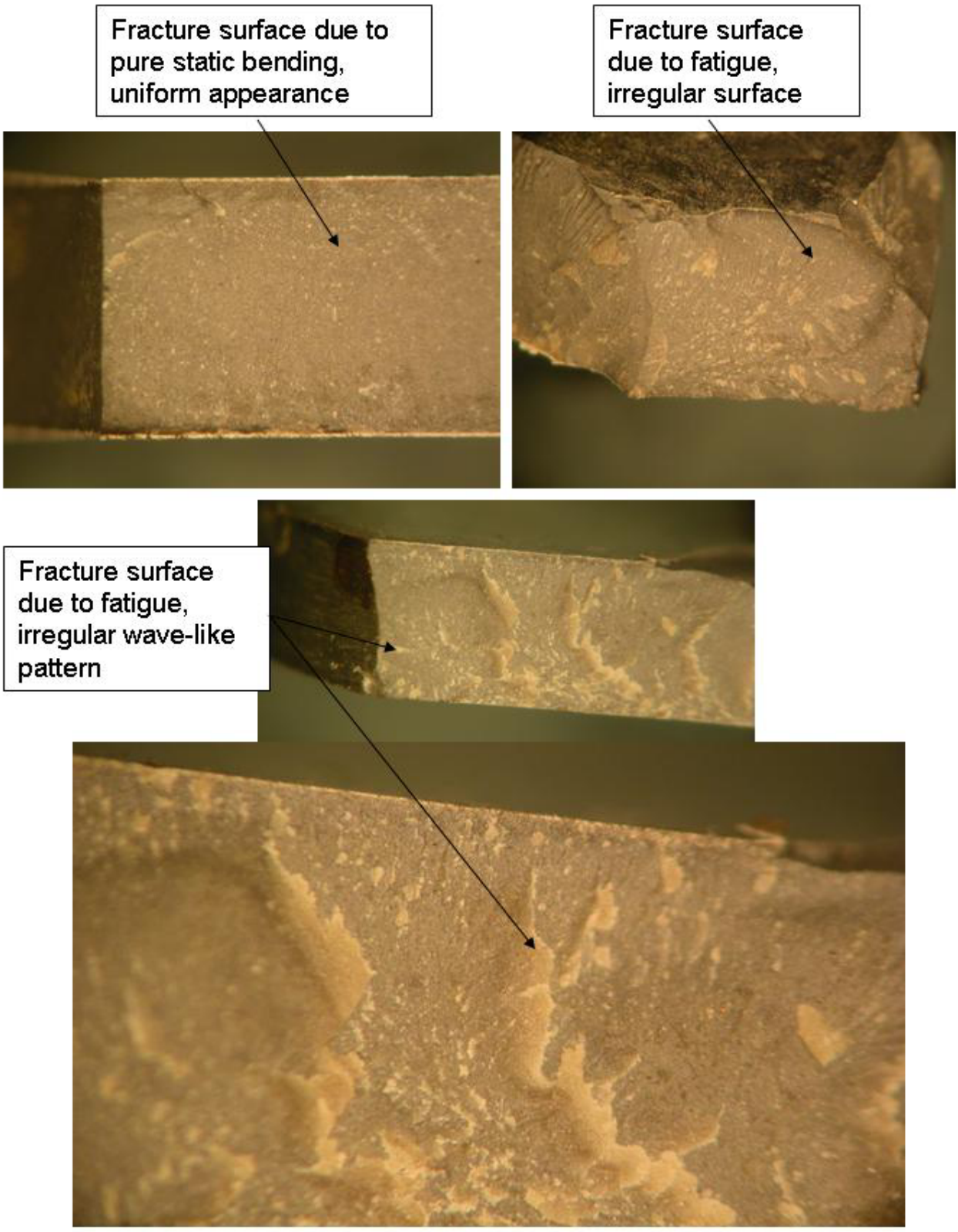

References

1 W.C. Ng, Dissertation, The Ohio State University, 1996

2 G. Bromfield, "Transducer Control Algorithms", *Ultrasonics International Symposium,* London, March 21, 2007

3 D. A. DeAngelis and G. W. Schulze, "Optimizing Piezoelectric Crystal Preload in Ultrasonic Transducers", *IEEE Ultrasonics, Ferroelectrics and Frequency Control*, 2008

4 M. Okayasu, G. Ozeki and M. Mizuno, "Fatigue failure characteristics of lead zirconate titanate piezoelectric ceramics*, Journal of European Ceramic Society*, 30, 713-725, 2010

5 U. Vogler, "Entwicklung Konverterqualitat", Herrmann Ultraschalltechnic Karlsbad Germany, 2010, *Unpublished work*

6 A.J. Masys, Thesis, Royal Military College of Canada, 2001

7 "Fundamentals of Piezoelectricity" , Physiks Instrumente GmbH & Co., 1996-2010, Web October 18 2010, http://www.physikinstrumente.com/en/products/prdetail.php?sortnr=400600.00

8 T. Zhang, T. Wang and M. Zhao, "Failure Behavior and failure criterion of conductive cracks (deep notches) in thermally depoled PZT-4 ceramics", *Acta Materialia*, 51, 4881-4895, 2003

9 H. Allik and T. J. R. Huges, "Finite Element Method for Piezoelectric Vibration", *International Journal for Numerical Methods in Engineering*, 2, 151-157, 1970

10 M. Guney and E. Eskinat, "Modeling of multilayered piezoelectric transducers with ultrasonic welding application", *Smart Material Structures*, 16, 541-554, 2007

11 D.A. Hall, "Review Non-linearity in piezoelectric ceramics", *Journal of Materials Science*, 36, 4575-4601, 2001

12 "Micropositioning or Nanopositioning" , Physiks Instrumente GmbH & Co., 1996-2010, Web October 20 2010, http://www.physikinstrumente.com/en/products/prdetail.php?sortnr=700400

13 A. Arnau and D. Soares, *Piezoelectric Transducers and Applications*, (Springer-Verlag Berlin Heidelberg 2008)

14 APC International Ltd., *Piezoelectric Ceramics: Principles and Applications*, (APC International Ltd., 2002)

15 J. Sheehan, *Converter Basics, Converter Materials, Converter Design Process Presentation*, Iowa State University, (March 2010), *Unpublished work*

16 W.P. Mason, *Physical Acoustics: Principles and Methods*, (New York: Academic 1964)

17 M. Prokic, Piezoelectric *Transducers Modeling and Characterization*, (M.P. Interconsulting 2004, e-book)

18 R. Lerch, "Simulation of Piezoelectric Devices by Two and Three Dimensional Finite Elements*, IEEE Transactions on Ultrasocnics, Ferroelectrics and Frequency Control*, vol 37, no. 2, 233-247, 1990

19 A. Iula, F. Vazquez, M. Pappalardo, J. A. Gallego, "Finite element three-dimensional analysis of the vibrational behavior of the Langevin-type transducer", *Ultrasonics*, 40, 513-517, 2002

20 K. Adachi, M. Tsuji and H. Kato, "Elastic contact problem of the piezoelectric material in the structure of a bolt-clamped langevin-type transducer", *J. Acoustic Society of America*, 105(3), 1651-1656, 1999

21 A. Abdullah, M. Sahini and A. Pak, "An approach to design a high power piezoelectric ultrasonic transducer", *Journal of Electroceram*, 22, 369-382, 2009

22 K. Adachi and S. Ueha, "Modal vibration control of large ultrasonic tools with the use of wave-trapped horns", *Journal Acoustical Society of America*, 87, 208-214, 1990

23 D.J. Ewins, "Basic and state-of-the-art of modal testing", *Sadhana*, vol. 25 part 3, 207-220, 2000

24 D. Culp, "Ultrasonic Resonator Design Using Finite Element Analysis (FEA)", Krell Engineering 1991-2002, September 16 2010, http://www.krell-engineering.com/fea/fea_info/fea_resonator_design.htm

25 J. Sheehan, *Transducer Design Consultation*, Boston MA, September 2010, *unpublished work*

Appendix A – Modifying piezoelectric material data to enter into ANSYS

The material property data found in the manufacturer's specifications is usually based upon using the X (11) or Z (33) direction as the axis of polarization along with any anisotropic properties. In ANSYS, the direction of polarization is in the Y (22) direction and this is the axis of rotation as well. This requires adjustments to the configuration of the material properties before entering into ANSYS. Table A.1 shows the material properties from the manufacturer's specification sheet in figure 3.3 with notes indicating changes to the values to account for pre-load conditions. Table A.2 shows how these values are adjusted to fit into ANSYS. For example, in the manufacturer's data sheet the direction of polarization is s33, but for ANSYS it is s22 therefore these values are exchanged. Table A.3 shows how the compliance matrix is created from the adjusted values in table A.2 and then transposed to create the stiffness matrix (table A.3a). After this, the shear terms are shifted to account for the coordinate changes (table A.3c). Table A.1c is the same as table 3.1b. These values are entered into ANSYS for the stiffness matrix. Table A.4 shows how the piezoelectric constants are manipulated. Table A.4a shows the data directly from the manufacturer as a 3x6 matrix. In order to enter these values into ANSYS, transpose the matrix (table A.4b), multiply by the stiffness matrix (table A.4c) and adjust the shear terms (table A.4d). Table A.4d is therefore the same as table 3.1c. The permittivity or capacitance from the manufacturer is shown in table A.5, where the directions have already been adjusted to account for the different axis configuration. Table A.5 is therefore the same as table 3.1d. [25]

Table A.1 – Material properties from manufacturer's data sheet adjusted for preload

Value	Units	ANSYS Input	Rational (9/17/2010)
Piezo Charge Constants			
d33	E-12 C/N	260	802 Value (250) +4.43% for 7500 psi preload (New Vernitron Method)
d31	E-12 C/N	-97	802 Value
d15	E-12 C/N	300	802 Value
d32	E-12 C/N	-97	Old Vernitron Method d32=d31
d24	E-12 C/N	300	Old Vernitron Method d24=d15
E Constants, Closed Circuit			
s11E	E-12 m^2/N	11.5	802 Value
s33E	E-12 m^2/N	13.5	802 Value
s44E	E-12 m^2/N	31.9	Old Vernitron
s12E	E-12 m^2/N	-3.7	Old Vernitron
s13E	E-12 m^2/N	-4.8	Old Vernitron
s23E	E-12 m^2/N	-4.8	Old Vernitron Method, s23E=s13E
s55E	E-12 m^2/N	31.9	Old Vernitron Method, s55E=s44E
s66E	E-12 m^2/N	32.6	Old Vernitron Method, s66E=2(s11E-s13E)
Capacitance, Constant Strain			
e33S	F/m	703.8	802 Value +13.3% for 7500 psi preload (New Vernitron Method)
e11S	F/m	789.5	802 Value

Table A.2 – Material properties adjusted to account for axis configuration in ANSYS

Catalog Label	ANSYS	Adjusted Label
Piezo Charge Constants		
d33	260	d22
d31	-97	d23
d15	300	d34
d32	-97	d21
d24	300	d16
E Constants, Closed Circuit		
s11E	11.5	s33E
s33E	13.5	s22E
s44E	31.9	s66E
s12E	-3.7	s31E, s13E
s13E	-4.8	s32E, s23E
s23E	-4.8	s12E, s21E
s55E	31.9	s44E
s66E	32.6	s55E
Capacitance		
e33s	703.8	e22s
e11s	789.5	e33s
e22s	789.5	e11s

Table A.3 – Compliance matrix – (a) Compliance matrix inputs, (b) Stiffness matrix, (c) Stiffness matrix adjusted for shear terms

(a) - [s] Compliance Matrix (m^2/N) - Closed Circuit

1.15E-11	-4.80E-12	-3.70E-12	0	0	0
-4.80E-12	1.35E-11	-4.80E-12	0	0	0
-3.70E-12	-4.80E-12	1.15E-11	0	0	0
0	0	0	3.19E-11	0	0
0	0	0	0	3.26E-11	0
0	0	0	0	0	3.19E-11

(b) - [c] Stiffness Matrix (N/m^2) - Closed Circuit

1.47E+11	8.11E+10	8.11E+10	0	0	0
8.11E+10	1.32E+11	8.11E+10	0	0	0
8.11E+10	8.11E+10	1.47E+11	0	0	0
0	0	0	3.13E+10	0	0
0	0	0	0	3.07E+10	0
0	0	0	0	0	3.13E+10

(c) - [c] Stiffness Matrix (N/m^2) - Closed Circuit

1.47E+11	8.11E+10	8.11E+10	0	0	0
8.11E+10	1.32E+11	8.11E+10	0	0	0
8.11E+10	8.11E+10	1.47E+11	0	0	0
0	0	0	3.13E+10	0	0
0	0	0	0	3.13E+10	0
0	0	0	0	0	3.07E+10

Table A.4 – Piezoelectric matrix – (a) Piezoelectric values from manufacturer, (b) Transposed piezoelectric values, (c) Piezoelectric matrix multiplied by the stiffness matrix, (d) Final piezoelectric matrix adjusted for shear terms

(a) - [d] Piezoelectric Matrix (C/N)

0	0	0	0	0	3.00E-10
-9.70E-11	2.60E-10	-9.70E-11	0	0	0
0	0	0	3.00E-10	0	0

(b) - [d] Piezoelectric Matrix Transposed (C/N)

0	-9.7E-11	0
0	2.6E-10	0
0	-9.7E-11	0
0	0	3E-10
0	0	0
3E-10	0	0

(c) - [d] * [c] = Piezoelectric Matrix (C/m^2)

0	-1.04	0
0	18.52	0
0	-1.04	0
0	0	9.40
0	0	0
9.40	0	0

(d) - [d] * [c] = Piezoelectric Matrix (C/m^2)

0	-1.04	0
0	18.52	0
0	-1.04	0
9.40	0	0
0	0	9.40
0	0	0

Table A.5 – Permittivity matrix – (a) Permittivity values from manufacturer, (b) Permittivity values for input to ANSYS

(a) - Permittivity Matrix - Constant Strain (F/m)

790	0	0
0	704	0
0	0	790

(b) - Permittivity Matrix - Constant Strain (F/m)

790	0	0
0	704	0
0	0	790

Appendix B – Alternate modes of vibration for series and parallel resonance

Figure B.1 – Alternate modes of vibration during parallel and series vibration – (a) Series mode at 54,424Hz, (b) Series mode at 57,659Hz, (c) parallel mode at 55,321Hz

(a)

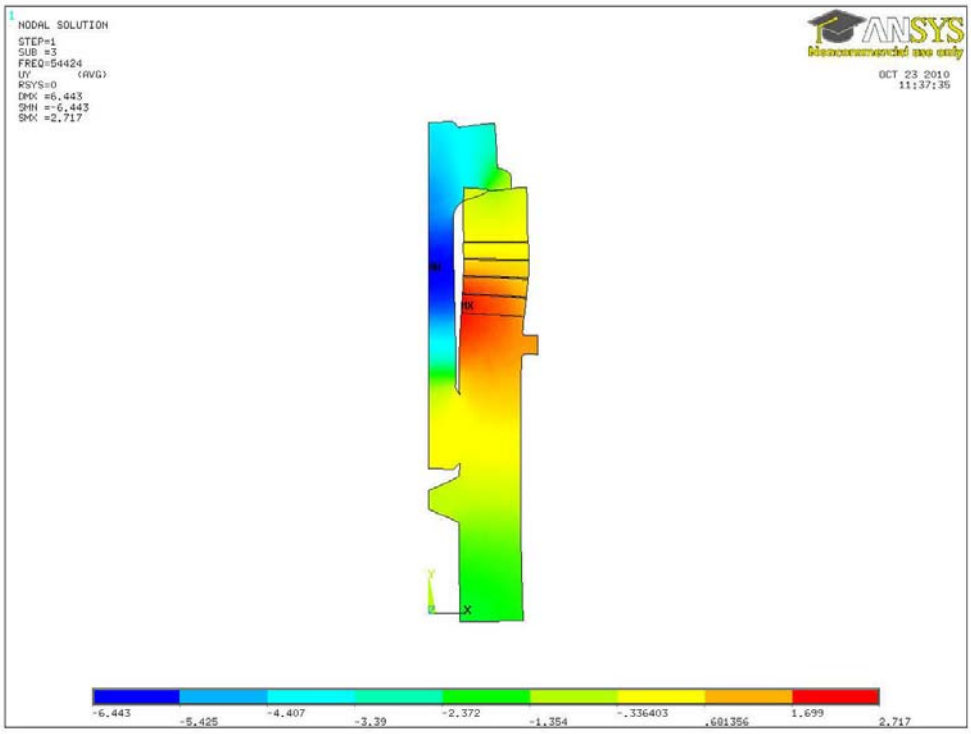

(b)

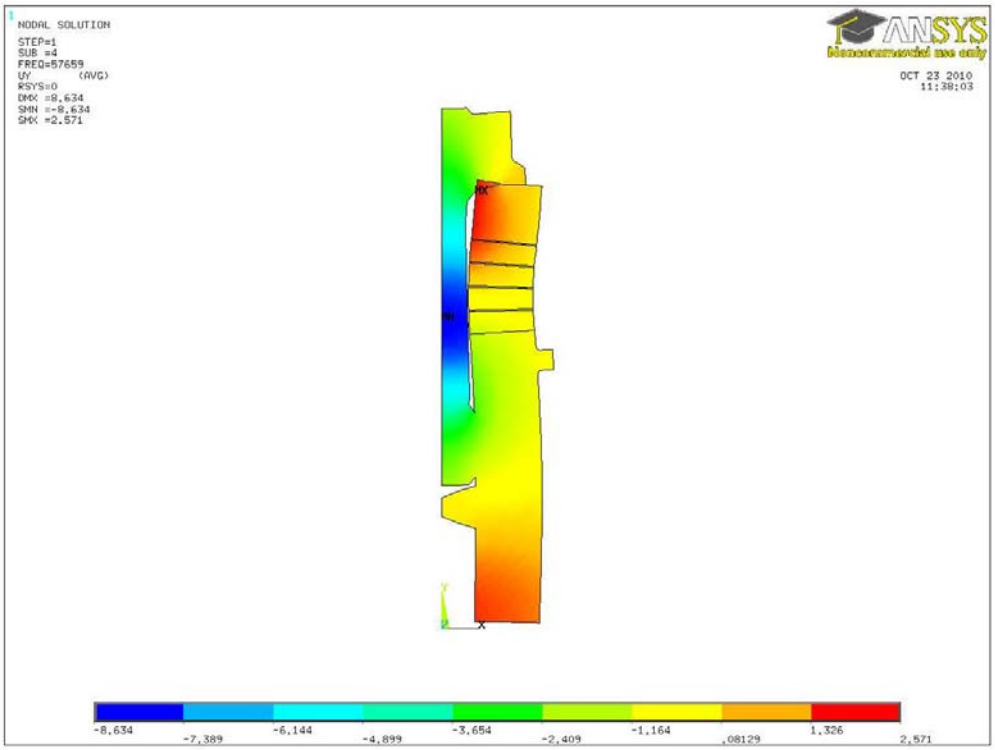

Figure B.1 (cont'd)

(c)

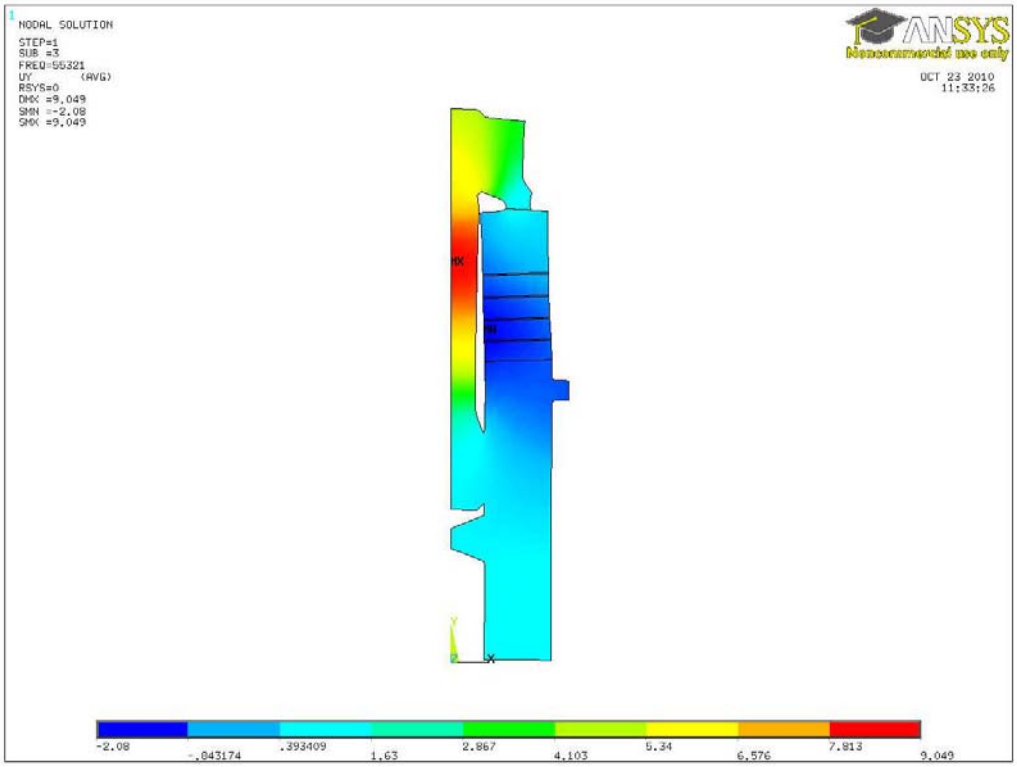

Appendix C – Nodal stress calculations for static and dynamic analyses

Table C.1 – numerical calculations from FEA analysis – (a) Top of disk #1, (b) Bottom of disk #1, (c) Top of disk #2, (d) Bottom of disk #2, (e) Top of disk #3, (f) Bottom of disk #3, (g) Top of disk #4, (h) Bottom of disk #4

(a) Disk #1 Top

Dyn Node:	Distance from center axis (mm)	Dyn MPa	Static MPa	Delta	% safety factor
1623	5.0	18.83	66.44	47.62	353%
1629	5.7	19.90	67.98	48.08	342%
1630	6.3	19.96	68.75	48.79	344%
1631	7.0	20.11	69.61	49.50	346%
1632	7.7	20.18	70.29	50.11	348%
1633	8.4	20.25	70.77	50.53	350%
1634	9.0	20.30	71.03	50.72	350%
1635	9.7	20.36	71.04	50.68	349%
1636	10.4	20.43	70.82	50.40	347%
1637	11.1	20.51	70.46	49.95	344%
1638	11.7	20.63	70.01	49.38	339%
1639	12.4	20.81	69.68	48.87	335%
1640	13.1	21.10	69.53	48.42	329%
1641	13.8	21.43	69.67	48.24	325%
1642	14.4	22.28	71.11	48.83	319%
1628	15.0	22.19	69.04	46.84	311%

(b) Disk #1 Bottom

Dyn Node:	Distance from center axis (mm)	Dyn MPa	Static MPa	Delta	% safety factor
1607	5.0	24.65	71.20	46.55	289%
1609	5.7	24.08	71.64	47.56	297%
1610	6.3	24.32	71.87	47.55	296%
1611	7.0	24.43	72.20	47.77	296%
1612	7.7	24.48	72.40	47.92	296%
1613	8.4	24.46	72.43	47.97	296%
1614	9.0	24.42	72.33	47.92	296%
1615	9.7	24.36	72.09	47.73	296%
1616	10.4	24.28	71.71	47.43	295%
1617	11.1	24.20	71.20	47.01	294%
1618	11.7	24.09	70.57	46.48	293%
1619	12.4	23.93	69.76	45.83	292%
1620	13.1	23.66	68.73	45.07	290%
1621	13.8	23.25	67.30	44.05	289%
1622	14.4	22.60	65.73	43.13	291%
1608	15.0	22.56	65.30	42.74	289%

Table C.1 (cont'd)

(c) Disk #2 Top

Dyn Node:	Distance from center axis (mm)	Dyn MPa	Static MPa	Delta	% safety factor
1527	5.0	25.88	74.33	48.45	287%
1533	5.7	25.80	72.47	46.67	281%
1534	6.3	25.76	72.50	46.75	281%
1535	7.0	25.78	72.71	46.94	282%
1536	7.7	25.75	72.77	47.02	283%
1537	8.4	25.69	72.72	47.02	283%
1538	9.0	25.61	72.52	46.90	283%
1539	9.7	25.51	72.19	46.68	283%
1540	10.4	25.38	71.73	46.35	283%
1541	11.1	25.21	71.14	45.92	282%
1542	11.7	25.01	70.40	45.39	282%
1543	12.4	24.73	69.49	44.76	281%
1544	13.1	24.37	68.35	43.98	280%
1545	13.8	23.87	66.91	43.04	280%
1546	14.4	23.32	65.56	42.24	281%
1532	15.0	22.59	63.95	41.36	283%

(d) Disk #2 Bottom

Dyn Node:	Distance from center axis (mm)	Dyn MPa	Static MPa	Delta	% safety factor
1511	5.0	30.68	76.37	45.69	249%
1513	5.7	29.53	75.54	46.01	256%
1514	6.3	29.32	74.90	45.58	255%
1515	7.0	29.14	74.51	45.37	256%
1516	7.7	28.97	74.08	45.11	256%
1517	8.4	28.79	73.59	44.80	256%
1518	9.0	28.59	73.01	44.42	255%
1519	9.7	28.36	72.33	43.97	255%
1520	10.4	28.07	71.54	43.46	255%
1521	11.1	27.74	70.63	42.89	255%
1522	11.7	27.34	69.60	42.26	255%
1523	12.4	26.86	68.44	41.58	255%
1524	13.1	26.29	67.16	40.87	255%
1525	13.8	25.63	65.71	40.09	256%
1526	14.4	24.88	64.49	39.61	259%
1512	15.0	24.81	64.42	39.61	260%

Table C.1 (cont'd)

(e) Disk #3 Top

Dyn Node:	Distance from center axis (mm)	Dyn MPa	Static MPa	Delta	% safety factor
1431	5.0	31.33	77.96	46.63	249%
1437	5.7	30.63	75.94	45.31	248%
1438	6.3	30.30	75.33	45.03	249%
1439	7.0	30.09	74.92	44.83	249%
1440	7.7	29.88	74.41	44.53	249%
1441	8.4	29.67	73.84	44.17	249%
1442	9.0	29.44	73.17	43.73	249%
1443	9.7	29.17	72.40	43.22	248%
1444	10.4	28.86	71.52	42.66	248%
1445	11.1	28.50	70.54	42.04	248%
1446	11.7	28.06	69.45	41.38	247%
1447	12.4	27.55	68.24	40.69	248%
1448	13.1	26.96	66.93	39.97	248%
1449	13.8	26.28	65.51	39.23	249%
1450	14.4	25.58	64.39	38.82	252%
1436	15.0	24.97	63.53	38.56	254%

(f) Disk #3 Bottom

Dyn Node:	Distance from center axis (mm)	Dyn MPa	Static MPa	Delta	% safety factor
1415	5.0	33.46	78.29	44.82	234%
1417	5.7	32.44	77.64	45.20	239%
1418	6.3	32.25	77.01	44.76	239%
1419	7.0	32.08	76.48	44.40	238%
1420	7.7	31.89	75.75	43.86	238%
1421	8.4	31.66	74.87	43.21	236%
1422	9.0	31.41	73.87	42.47	235%
1423	9.7	31.12	72.77	41.66	234%
1424	10.4	30.79	71.60	40.81	233%
1425	11.1	30.42	70.37	39.95	231%
1426	11.7	29.99	69.07	39.08	230%
1427	12.4	29.47	67.67	38.20	230%
1428	13.1	28.82	66.18	37.36	230%
1429	13.8	28.04	64.51	36.48	230%
1430	14.4	27.12	63.05	35.93	232%
1416	15.0	26.76	62.76	36.00	235%

Table C.1 (cont'd)

(g) Disk #4 Top

Dyn Node:	Distance from center axis (mm)	Dyn MPa	Static MPa	Delta	% safety factor
1335	5.0	33.45	79.61	46.15	238%
1341	5.7	32.81	77.95	45.14	238%
1342	6.3	32.68	77.48	44.80	237%
1343	7.0	32.56	76.97	44.41	236%
1344	7.7	32.37	76.16	43.79	235%
1345	8.4	32.13	75.18	43.05	234%
1346	9.0	31.86	74.06	42.20	232%
1347	9.7	31.57	72.86	41.29	231%
1348	10.4	31.26	71.60	40.34	229%
1349	11.1	30.92	70.30	39.39	227%
1350	11.7	30.53	68.96	38.43	226%
1351	12.4	30.07	67.56	37.49	225%
1352	13.1	29.48	66.05	36.57	224%
1353	13.8	28.70	64.36	35.66	224%
1354	14.4	27.78	62.84	35.06	226%
1340	15.0	27.05	61.43	34.38	227%

(h) Disk #4 Bottom

Dyn Node:	Distance from center axis (mm)	Dyn MPa	Static MPa	Delta	% safety factor
61	5.0	33.09	80.98	47.89	245%
97	5.7	33.62	81.54	47.92	243%
98	6.3	33.44	80.58	47.15	241%
99	7.0	33.23	79.33	46.10	239%
100	7.7	32.97	77.76	44.80	236%
101	8.4	32.68	76.09	43.41	233%
102	9.0	32.39	74.35	41.96	230%
103	9.7	32.09	72.59	40.50	226%
104	10.4	31.79	70.85	39.06	223%
105	11.1	31.50	69.18	37.67	220%
106	11.7	31.26	67.63	36.38	216%
107	12.4	31.06	66.26	35.20	213%
108	13.1	30.95	65.10	34.15	210%
109	13.8	30.82	63.94	33.13	207%
110	14.4	30.62	62.77	32.15	205%
96	15.0	29.51	60.24	30.73	204%

Appendix D – Raw test data from experiment

Table D.1 – raw data from testing (contained in the next 8 pages, created using larger 11”x17” paper size to accommodate the amount of information and to improve readability)

Curriculum Vitae

Chris Hampton graduated with honors from the Illinois Institute of Technology in 2002 with a Bachelors of Science in Mechanical Engineering. Before and after receiving his B.S., he worked across a broad range of industries in various technically challenging hands-on engineering and management positions. From 1997-2002, he worked as a mechanical designer and project manager for Industrial Fluid Systems Incorporated where he designed and manufactured customized industrial fluid recycling equipment. From 2002-2004, he worked at The Parkson Corporation in the quality control department where he inspected wastewater treatment equipment after fabrication. From 2004-2006, he returned to Industrial Fluid Systems Incorporated and was responsible for opening a satellite manufacturing facility in Illinois. Since 2006, he has worked at Herrmann Ultrasonics Incorporated where he manages a team of ultrasonic engineers responsible for installing, maintaining and troubleshooting ultrasonic welding equipment. He received his Masters of Mechanical Engineering degree in December of 2010 from the University of Illinois Urbana-Champaign.